

Kyushu Institute of Technology

**Quasi-Casimir coupling induced phonon  
heat transfer across a nanogap**

Submitted to Department of Mechanical Engineering

In Partial Fulfillment of the Requirements  
for the Degree of Doctor of Philosophy Engineering

by

Wentao CHEN

February 2022



# Contents

<b>Contents</b> .....	<b>I</b>
<b>Abbreviations and Symbols</b> .....	<b>I</b>
<b>1 Introduction</b> .....	<b>1</b>
1.1 Current research in nanoscale heat transfer .....	1
1.1.1 Near-field heat transfer.....	2
1.1.2 Thermal transport at solid–liquid interface .....	5
1.2 Objectives .....	11
1.3 Outline.....	12
<b>2 Molecular dynamics simulation</b> .....	<b>15</b>
2.1 Introduction.....	15
2.2 Overview of molecular dynamics simulation system .....	18
2.3 Molecular dynamics simulation method .....	19
2.3.1 Intermolecular potentials.....	19
2.3.2 Intermolecular force .....	20
2.3.3 Integration methods.....	22
2.3.4 Thermodynamic ensembles.....	24
2.3.5 Periodic boundary condition .....	25
2.3.6 Thermostating .....	27
2.4 Computational details .....	28
2.4.1 Density profiles .....	28
2.4.2 Temperature profiles .....	28

2.4.3	Atomic vibrational characteristics.....	29
2.4.4	Vibrational density of states .....	30
2.4.5	Net heat flux and local heat flux by Irving–Kirkwood method .....	30
<b>3</b>	<b>Quasi-Casimir heat transfer across a vacuum gap.....</b>	<b>33</b>
3.1	Introduction.....	33
3.2	Simulation method .....	34
3.3	Results and discussion .....	38
3.3.1	Transient thermal behavior in non-steady state.....	38
3.3.2	Temperature profiles in steady state.....	40
3.3.3	Net heat flux and thermal gap conductance .....	42
3.3.4	Thermal resonance induced by quasi-Casimir coupling .....	44
3.3.5	Local heat flux by Irving–Kirkwood method.....	46
3.4	Summary .....	50
<b>4</b>	<b>Quasi-Casimir coupling at the solid–liquid interface.....</b>	<b>53</b>
4.1	Introduction.....	53
4.2	Simulation method .....	54
4.3	Results and discussion .....	58
4.3.1	Quasi-Casimir coupling via a liquid monolayer .....	58
4.3.2	Thermal resonance between two liquid layers .....	64
4.3.3	Thermal energy transport across a nanogap .....	67
4.4	Summary .....	73
<b>5</b>	<b>Weak solid–liquid interaction enhances phonon heat transfer .....</b>	<b>75</b>
5.1	Introduction.....	75
5.2	Simulation method.....	76

5.3	Results and discussion .....	80
5.3.1	Density profiles .....	80
5.3.2	Potential and kinetic energy .....	81
5.3.3	Net heat flux and thermal gap conductance .....	83
5.3.4	Atomic vibrational displacement of liquid atoms .....	84
5.3.5	VDOS of interfacial solid layers .....	86
5.3.6	Knudsen number effects .....	86
5.4	Summary .....	89
<b>6</b>	<b>Conclusions and outlook .....</b>	<b>91</b>
6.1	Conclusions .....	91
6.2	Outlook .....	92
	<b>Reference .....</b>	<b>93</b>
	<b>Acknowledgments .....</b>	<b>107</b>
	<b>Appendix .....</b>	<b>109</b>



## Abbreviations and Symbols

$a$	lattice constant of platinum, m
$A$	cross-sectional area of the $x$ - $y$ plane, $\text{m}^2$
$d$	gap distance between interfacial solid–liquid or liquid–liquid layers, m
$D$	vacuum gap distance, m
$\Delta E$	difference between cumulative input and output energy, J
$E_C$	cumulative output energy, J
$E_H$	cumulative input energy, J
$E_i^k$	kinetic energy of molecule $i$ , J
$f$	frequency, Hz
$F_{ij}$	intermolecular force between pair molecules $i$ and $j$ , N
$G$	thermal conductance, $\text{W m}^{-2} \text{K}^{-1}$
$J_{is}$	local heat flux corresponding to self-wall molecular interaction, $\text{W m}^{-2}$
$J_{io}$	local heat flux corresponding to other wall molecular interaction, $\text{W m}^{-2}$
$J_k$	local heat flux corresponding to molecular kinetic energy, $\text{W m}^{-2}$
$J_p$	local heat flux corresponding to molecular potential energy, $\text{W m}^{-2}$
$J_q$	local heat flux by Irving–Kirkwood method, $\text{W m}^{-2}$
$k_B$	Boltzmann constant, $\text{m}^2 \text{kg s}^{-2} \text{K}^{-1}$
$L_x$	length of simulation cell in $x$ -direction, m
$L_y$	length of simulation cell in $y$ -direction, m
$L_z$	length of simulation cell in $z$ -direction, m
$m$	mass of an atom, kg

$N$	number of atoms
$q$	heat flux, $\text{W m}^{-2}$
$r_{ij}$	distance between pair molecules $i$ and $j$ , m
$t_f$	long finite time, s
$t_0$	initial time, s
$\Delta T$	temperature difference between two thermostats, K
$T$	local temperature of each bin, K
$T_{\text{Ci}}$	temperature of interfacial layer at cooling wall, K
$T_{\text{Cil}}$	temperature of cooling interfacial liquid layer, K
$T_{\text{Cis}}$	temperature of cooling interfacial solid layer, K
$T_{\text{Hi}}$	temperature of interfacial layer at heating wall, K
$T_{\text{Hil}}$	temperature of heating interfacial liquid layer, K
$T_{\text{His}}$	temperature of heating interfacial solid layer, K
$\bar{v}_i$	mean velocity component $i$ ( $=x, y, z$ ), $\text{m s}^{-1}$
$v_j$	velocity of molecule $j$ , $\text{m s}^{-1}$
$v_{n,i}$	velocity component $i$ ( $=x, y, z$ ) of atom $n$ , $\text{m s}^{-1}$
$v_{z,i}$	velocity component of molecule $i$ in $z$ -direction, $\text{m s}^{-1}$
$\Delta z_{i,t}$	vibrational displacement of atom $i$ at time $t$ , m
$\bar{z}$	equilibrium position of an atom in $z$ -direction, m
$z_{i,t}$	$z$ position of atom $i$ at time $t$ , m

*Greek symbols*

$\varepsilon$	energy parameter of potential function, J
---------------	---

$\phi$	pair potential, J
$\sigma$	length parameter of potential function, m
$\omega$	angular frequency, rad/s

*Subscripts*

C	cooling wall
H	heating wall
i	interface
l	liquid
s	solid
$x$	$x$ -direction
$y$	$y$ -direction
$z$	$z$ -direction



## Chapter 1

# 1 Introduction

## 1.1 Current research in nanoscale heat transfer

Nanoscale heat transfer has been a challenging research topic for the last decade. Phonon transmission dominates the heat transfer mechanism between two objects in the transition from heat conduction to near-field heat transfer (NFHT). Therefore, the scale of the gap distance  $D$  dominates the heat transfer between two objects at different temperatures in a vacuum, from the conventional heat conduction ( $D = 0$ ) to thermal radiation ( $D > \lambda_T$ , Wien's wavelength  $\lambda_T \approx 10^{-5}$  m at room temperature) [1,2]. As shown in Fig. 1.1, when the two objects are separated by a gap of  $D < \lambda_T$ , known as the regime of the near-field radiative heat transfer (NFRHT), the amount of heat transfer can be several orders of magnitude greater than Planck's blackbody limit [3–8]. Therefore, the

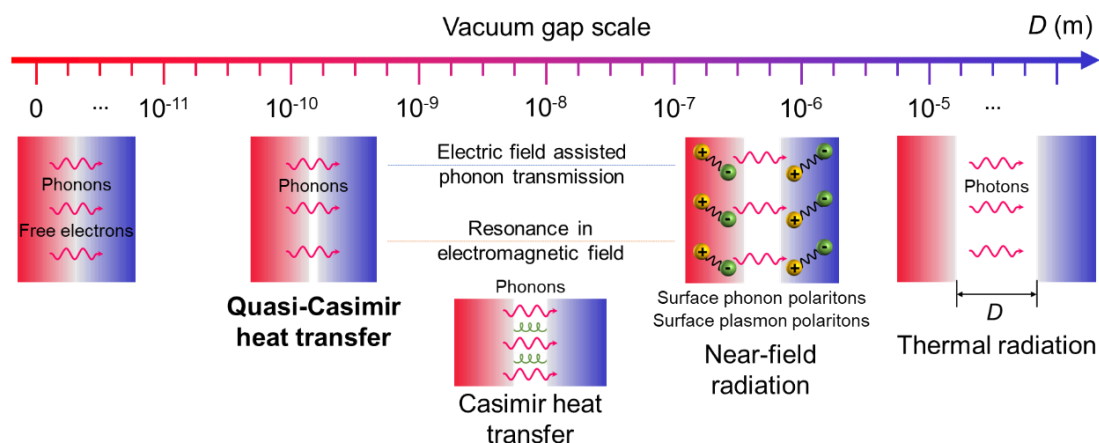


**Fig. 1.1** Scale of a vacuum gap dominates the heat transfer mechanism between two objects.

NFRHT has attracted considerable interest in advanced applications of thermal management [9,10], radiative cooling [11,12], nanogap near-field thermophotovoltaics [13], and heat-assisted magnetic recording [14,15]. Meanwhile, the presence of liquid in the nanogap is significant to understand better the nanoscale heat transfer at the solid–liquid interface.

### **1.1.1 Near-field heat transfer**

The thermal energy transported by the coupling between the electromagnetic waves of the heating object and the phonons or plasmons of the cooling object in the regime of NFRHT, has been explored using the fluctuating electrodynamics theory [16] and experiments [17–19]. Shen et al. have found that the surface phonon polaritons can exist near the solid interface and improve the heat exchange between two closed solid surfaces [18]. Surface phonon polaritons are electromagnetic waves that propagate along with the interfaces of polar dielectrics, which can be generated by resonant coupling between the electromagnetic field and optical phonons in polar dielectrics. A glass (silica) microsphere 50 or 100  $\mu\text{m}$  in diameter is attached to the tip of a biomaterial ( $\text{Si}_3\text{N}_4/\text{Au}$ ) AFM cantilever with UV adhesive. Solid substrates are made by  $\text{SiO}_2$ , Si, or Au. The radiative heat transfer can be enhanced significantly compared to blackbody radiation at extremely small gaps, while the heat transfer coefficient becomes smaller in the case of  $\text{SiO}_2$ –Si and  $\text{SiO}_2$ –Au due to the weaker resonance effects.

In the regime of  $D < 10^{-7}$  m, the atomic Coulomb interaction between two polar nanoparticles dominates the NFRHT in the gap distance of 8–100 nm [20], while the phonons serve as effective thermal carriers between two objects separated by nanometer

vacuum gap [21–29]. In particular, phonon coupling in electric fields becomes significant in the transition regime from NFRHT to heat conduction. However, the boundary between heat conduction and thermal radiation is still unclear when the gap distance between two objects is at the nanoscale.

The transition regime from near-field thermal radiation to phonon heat conduction has been investigated based on lattice dynamics simulation [30]. Two kinds of forces exerted on the solid surfaces in the simulation model, the short-range repulsive forces due to atomic bonding force and the long-range Coulomb forces, are computed using the electric fields generated by oscillating ions. To investigate the heat exchange between two solid surfaces, the thermal conductance at a few nanometer gaps was calculated by Green's function and Rytov's formulation. As gaps are larger than 1 nm, the thermal conductance computed using the atomistic approach agrees well with Rytov's formulation. When the gap distance is smaller than 1 nm, the atomistic approach predicts conductance significantly higher than the continuum approach due to the atomic bonding force between interfacial layers. This bonding forces can provide another channel for improving thermal energy transportation.

Furthermore, the acoustic phonons theoretically dominate the heat transfer across a gap of 1–5 nm between two Au surfaces applied to a bias voltage of 0.6 V [31]. Jarzembki et al. have investigated force-induced acoustic phonon transport across vacuum gaps between silicon and platinum surfaces under a bias voltage of 0.8 V [32]. They utilized a custom-built high-vacuum shear force microscope (HV-SFM) to measure heat transfer between a silicon tip and a feedback-controlled platinum nanoheater. The silicon tip temperature is 295 K, and the initial temperature of the platinum nanoheater is 467.13 K. When the silicon tip is approached the platinum

nanoheater, the temperature of platinum nanoheater will decrease and drop sharply in the bulk-contact regime. To confirm the accuracy of the experimental data, a one-dimensional atomic chain system separated by a vacuum gap was established. In this system, short-range van der Waals force is modeled by Lennard–Jones potential, long-range electrostatic surface charge interaction is modeled by Coulomb force. Lennard–Jones force just can drive heat transfer for  $\delta < 1.1$  nm, and Coulomb force becomes dominant in heat transfer for  $1.1 \text{ nm} < \delta < 10$  nm. The experimental results agree well with theoretical results and the thermal conductance is enhanced rapidly when the gap is close to the bulk contact regime. However, clarifying the mechanism of the electric field-assisted phonon transmission across a vacuum gap in this transition regime is still challenging work.

On the other hand, Casimir heat transfer induced by resonance in electromagnetic fields was proposed in the transition regime from NFRHT to heat conduction [33]. Consider an object at a high-temperature  $T_1$ , the thermal agitation of the object's atoms gives rise to phonons that propagate as acoustic waves and cause the surface to exhibit time-varying undulations. A second object, at a low-temperature  $T_2 < T_1$ , is close to the first object, with a vacuum gap between the objects. The undulations of the first object's surface exert a time-varying Casimir force on the second object's surface, producing phonons in the second object. Since the phonons are heat carriers, thermal energy can be transferred from the first object to the second object.

The Casimir force was first introduced in 1948 as an attractive force acting between neutral objects based on quantum fluctuations of electromagnetic fields [34]. A local model of the dielectric function was applied to explain the phonon coupling mechanism induced by the Casimir force across a vacuum gap of  $D < 10$  nm between two dielectric

solids [35]. Fong et al. reported experiment evidence that phonons can travel across a vacuum gap due to quantum fluctuations [36]. They considered the interaction between two phonon modes based on a spring-mass model. Two objects attached to springs are linked to thermal baths at different temperatures. The vibration of two objects disturbs the zero-point energy of the electromagnetic vacuum and generates the Casimir force. Therefore, the Casimir interaction acts as a coupling spring to contact two objects. In their experiment, two  $\text{Si}_3\text{N}_4$  membranes were aligned in parallel and connected to heat baths. By adjusting the sample temperature to tune the film stress, the frequencies of the two membranes are matched at 191.6 kHz when mode temperature  $T_1 = 287$  K and  $T_2 = 312.5$  K. The Casimir heat transfer between the membranes strongly depends on the gap distance. The mode temperature is the same as the heat bath temperature in the far-field region. When two membranes move close, the temperature changes and becomes identical as the gap distance is less than 350 nm. The temperature difference between the heat bath and membrane can induce a net heat flux across this system. However, the phonon heat transfer across a nanogap caused by the intermolecular interaction between two solid interfacial layers has never been verified without an electromagnetic field. To this end, in the present study, a quasi-Casimir coupling model is proposed for phonon heat transfer between two parallel solid walls separated by a sub-nanometer vacuum gap in the absence of an electromagnetic field.

### 1.1.2 Thermal transport at solid–liquid interface

NFHT across a vacuum nanogap between two objects has already attracted considerable interest in the field of nanoscale heat transfer. Meanwhile, the presence of liquid in the nanogap is also essential to better understand the nanoscale heat transfer at

the solid–liquid interface. Thermal transport at the solid–liquid interface is becoming ever more critical with the development of next-generation high-efficiency thermoelectric devices. It is well known that the temperature changes abruptly at the interface due to the significantly different thermal properties between solid and liquid when thermal energy is transported across the solid–liquid interface. Thus, the interfacial thermal resistance characterized by Kapitza length  $L_k$  is an obstacle to thermal transport at the solid–liquid interface.

Kapitza length has considerable effects on interfacial thermal energy transportation in micro/nanochannel. In recent years, the chemical and physical properties of the interface have been modified to control the interfacial thermal resistance based on experiments [37,38] and simulations [39–46]. However, the direct experimental measurements of thermal transport in nanoscale systems are still challenging. Molecular dynamics (MD) simulation is a powerful tool for investigating solid–liquid interfacial characteristics. It is well known that interfacial thermal resistance is impacted by the surface wettability [47–50], nanostructure [51–54], surfactant adsorption [55–57], self-assembled monolayer [58–60], temperature [61–63], and liquid pressure [64,65] and so on. The solid surface can be improved to regulate the solid–liquid interfacial thermal resistance.

With the rapid development of fabricating and manufacturing micro/nanoscale devices, heat transfer characteristics are significantly different in varying scale systems. In our previous experimental research, the scale effect of the boundary condition was studied at the solid–liquid interface on the single-phase convective heat transfer characteristics in a microchannel flow [66]. It has been observed that the solid–liquid interfacial resistance cannot be disregarded when the slip length and the thermal slip

length are comparable with the hydraulic diameter, as shown in Fig. 1.2. Rabani et al. [67] have investigated the effect of the wall force field on the thermal transport properties in a nanochannel with the different channel height and the gas density in various Knudsen numbers. The local thermal conductivity in the wall force field region keeps approximately constant if the Knudsen number is regulated by varying the channel height. Taking a different approach, Yenigun and Barisik [68] revealed that the solid thermal conductivity decreases with reducing the solid nano-film thickness. The enhanced ballistic phonon transport suppresses the interfacial thermal energy transport since the phonon passage is changed through the interface.

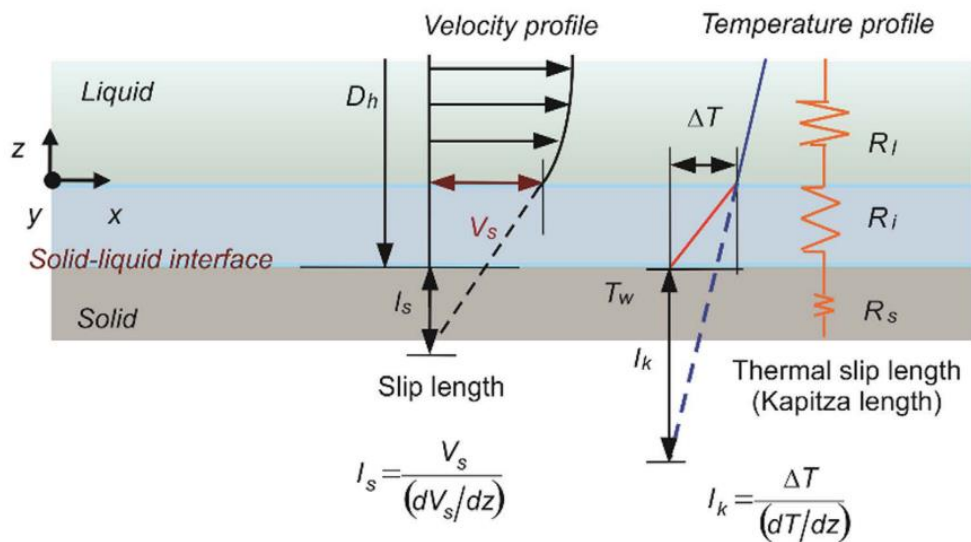


**Fig. 1.2** Slip boundary condition at the solid–liquid interface: slip length and thermal slip length [66].

Additionally, early research has already investigated the effects of surface wettability on interfacial heat transfer using MD simulations;  $L_k$  sharply decreases as the solid–liquid interaction increases. Barisik and Beskok [61] clarified that interfacial thermal resistance strongly depends on the near surface water density structure, which is a

function of the molecular interaction parameter  $\varepsilon$  value. To identify the proper parameter for water–silicon interactions, they have simulated a nano water droplet on the silicon surface with different wetting behavior. Results show that the interfacial thermal resistance between a liquid and solid is dominated by the liquid structure formed on the solid surface under high wetting conditions. Nagayama et al. [51] have made the surface nanostructures in the interfacial region to calibrate the solid–liquid interaction potentials using MD simulation, as shown in Fig. 1.3. They found that the thermal resistance at the solid–liquid interface can be reduced by the nanostructures and the interfacial heat flux increases almost linearly proportional to the surface area. The effect of surface nanostructures is significant in determining the evaporation rate of the ultra-thin liquid film. The evaporation rate at the hydrophilic nanostructured surface has a more significant value than that of the flat surface when the film thickness is larger than that of the adsorbed layer. In addition, Chen and Zhang [69] demonstrated that surface roughness weakens the mobility of liquid atoms close to the solid surface, resulting in liquid atoms in contact with the solid surface for a longer time. Shibahara et al. [70] found that the gap between fins can reduce the thermal resistance of solid–liquid interface, which was attributed to the longer residence time of liquid molecules at the interfacial zone.

As a result, studies over the past decade have provided important information on the solid-like liquid layers above the solid surface in nanoscale systems. Xue et al. [71] found that the liquid layers at the solid–liquid interface have no effects on thermal transport properties. However, Frank and Drikakis [72] pointed out that the thermal conductivity in the direction parallel to the solid surfaces is enhanced three times in a nanochannel compared to the unrestricted liquid and the long-range phonons exist in the

nanochannel due to the structural order of liquid. Moreover, Liang and Tsai [73] also have discovered that the effective thermal conductivity of nanofluids enhances with increasing the interaction between solid and liquid molecules. It is widely understood that the thermal conductivity of ordered crystalline materials is much larger than that of disordered amorphous materials on account of the efficient thermal transport in solids by virtue of the lattice vibration (phonons).

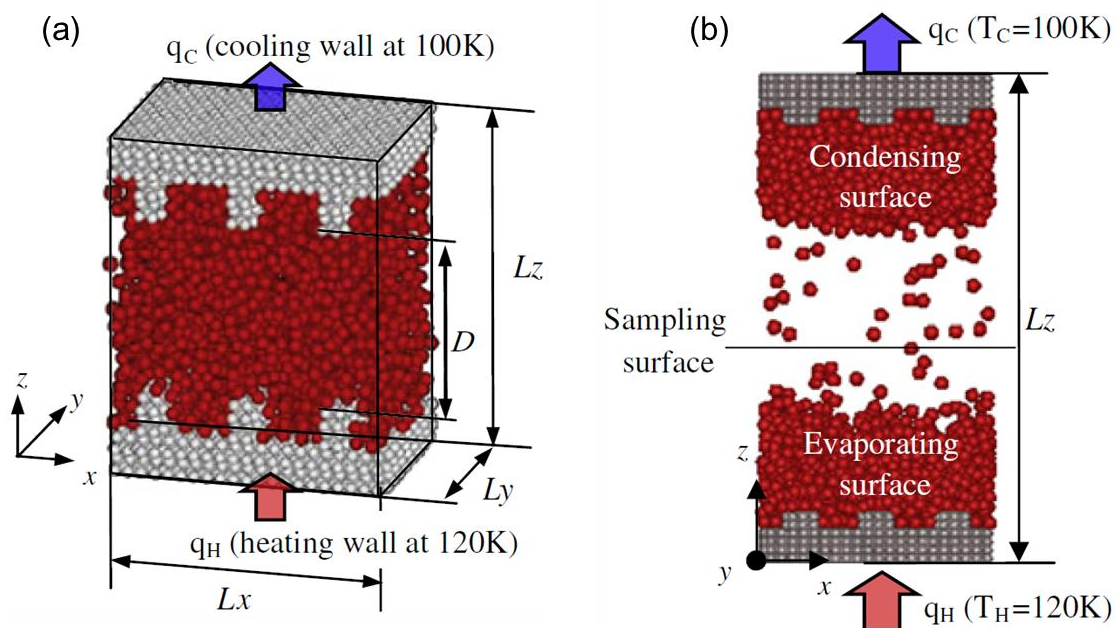


**Fig. 1.3** Molecular dynamics simulation systems: (a) simulation cell for liquid film; (b) simulation cell for evaporating and condensing liquid film [51].

Nevertheless, the amorphous liquid cannot produce this powerful thermal transport mechanism owing to the lack of ordered structures. The thermal energy will be transported passing through the ordered liquid layer via the phonon ballistic mechanism if multiple ordered liquid layers formed in the solid–liquid interfacial region. It is also found that the thickness of the interfacial liquid layer is equal approximately to the distance of 2-fold of liquid argon atoms, which is barely influenced by the interaction

between solid and liquid atoms [74]. The heat transfer in the base liquids is the diffusive mechanism and the thermal transport at the interfacial layer should be regarded as the ballistic mechanism.

As discussed above, the ordered liquid layer adjacent to the solid surface can increase the thermal conductivity of interfacial liquid layers. In the case of a liquid monolayer firmly sandwiched by two solid walls, the thermal resistance becomes extremely low at the solid–liquid interface compared with the cases of multiple layers [42,46,75]. Liu et al. [42] have utilized the non-equilibrium molecular dynamics (NEMD) simulations to investigate the thermal resistance between the two solid surfaces for varying thickness of liquid film and alignment of the two solid surfaces. When the liquid film thickness is equal to, or less than four molecular dimensions, the film thickness and the surface alignment significantly influence the thermal resistance. Furthermore, the thermal resistance of liquid confined in parallel-aligned walls is lower than that in the cross-aligned wall.

Similarly, Liang and Tsai [75] have studied thermal conduction across the Ag particle-Ar thin film interface. It was found that the solid–liquid film interfacial thermal resistance is around one order of magnitude smaller than the solid-bulk liquid interfacial thermal resistance when the liquid film contains one molecule layer. By analyzing the vibrational density of states of Ag atoms and Ar atoms, they demonstrated that the low thermal resistance in the monolayer film case is caused by the resonant thermal transport between Ag atoms and Ar atoms. Consequently, the interfacial liquid layers are dominant in controlling the thermal transport at the solid–liquid interface. The gap distance can be the critical factor in determining the heat transfer across a nanogap between two objects in contact with liquid.

## 1.2 Objectives

In this thesis, MD simulations were carried out to provide fundamental insights into nanoscale heat transfer between the regimes of NFRHT and heat conduction. A new heat transfer mode, named quasi-Casimir heat transfer will be investigated in the following chapters. The differences between Casimir heat transfer and quasi-Casimir heat transfer are shown in Table 1-1. The main objectives of this thesis are described as follows.

**Table 1-1** Casimir heat transfer and quasi-Casimir heat transfer in a nanogap between two objects.

	Casimir heat transfer	Quasi-Casimir heat transfer
Gap distance	$10^{-9} \sim 10^{-6}$ m	$0 \sim 10^{-9}$ m
Heat transfer mechanism	Quantum fluctuations of electromagnetic field	Quantum fluctuations of electron density
Interactive force	Casimir force <sup>[34]</sup> $F = -\frac{\pi^2 \hbar c}{240D^4}$ <sup>a</sup>	Intermolecular force $F = 4\epsilon\pi n^2 \sigma^3 \left[ \frac{1}{45} \left( \frac{\sigma}{D} \right)^9 - \frac{1}{6} \left( \frac{\sigma}{D} \right)^3 \right]$ <sup>b</sup>

<sup>a</sup> For two metals. <sup>b</sup> Surface–surface interactions based on LJ potential.

- (1) To verify phonon heat transfer due to the thermal resonance induced by quasi-Casimir coupling across a vacuum nanogap without electromagnetic fields.
- (2) To clarify the phonon transmission across a nanogap via liquid layers induced by quasi-Casimir coupling.
- (3) To investigate the effects of weak molecular interaction on the quasi-Casimir

phonon heat transfer across a nanogap.

Upon completing these objectives, we look forward to understanding the physical mechanism of quasi-Casimir heat transfer across a nanogap. These findings can pave the way for the exploitation of near-field heat transfer.

### **1.3 Outline**

In vacuum, the scale of the gap distance dominates the heat transfer between two objects separated at different temperatures. When the two objects are separated by a nanogap, the near-field radiative heat transfer can be several orders of magnitude greater than the Planck's blackbody limit. Experiments have demonstrated that the Casimir coupling due to quantum fluctuation can resonantly enhance the phonon heat transfer across a nanogap in the electromagnetic field. However, it is unknown if the phonon heat transfer can be enhanced without the electromagnetic field.

In this thesis, we proposed a new heat transfer mode to describe phonon heat transfer induced by quasi-Casimir coupling across a sub-nanometer gap without the electromagnetic field. This mode differs from conventional heat conduction, convection, and radiation and is independent of electrostatic interaction, electron cloud overlap, surface phonon polaritons, and surface plasmon polaritons. This thesis consists of 6 Chapters.

Chapter 1 provides the literature review, problem description and purpose of this study. The current research progress and applications about near-field heat transfer and thermal transport at solid-liquid interface were introduced and the unsolved problems were described. Subsequently, the concept of a new heat transfer mode named quasi-

Casimir coupling was proposed. This study aims to verify this mode and its contribution to heat transfer.

Chapter 2 introduces the methodology, technique, and implementation of molecular dynamics (MD) simulation applied in this study. The simulation system consists of two solid walls separated by a nanogap in vacuum, with and without liquid atoms. Lennard–Jones (LJ) potential was applied to the molecular interaction between solid–solid atoms and liquid–liquid atoms, and the modified LJ potential was applied to solid–liquid interactions as a function of surface wettability. The analysis methods of the density, temperature profiles, atomic vibrational characteristics, and local heat flux by Irving–Kirkwood (I–K) method etc. were described.

Chapter 3 demonstrates the MD simulation results for two planar solid walls separated by a vacuum gap under equilibrium and non-equilibrium states. The heat exchange between two solid walls exists even in vacuum and enhances exponentially by narrowing the gap distance. This is owing to the thermal resonance induced by the quasi-Casimir coupling at the interfacial layers of solid walls, which is confirmed by the wave analysis. Moreover, the apparent local heat flux by I–K method at the interfacial layers is larger than that at the inner layers singularly, showing the dependence of the strong thermal resonance at the two interfacial layers induced by quasi-Casimir coupling. The quasi-Casimir heat transfer achieves high heat flux up to a magnitude of 10 GW/m<sup>2</sup> level, attracting considerable interest in promising advanced applications.

Chapter 4 demonstrates the quasi–Casimir coupling at the solid–liquid interface between interfacial solid–liquid and liquid–liquid layers for simulation systems with adsorbed solid-like liquid layers in the nanogap. The thermal resonance between the two liquid layers exists due to the quasi-Casimir coupling, which agitates the co-occurrence

of the thermal resonance between the interfacial solid layers. As a result, the heat flux and thermal conductance exponentially increase with narrowing the gap distance  $D$  between two interfacial solid layers, one to three orders of magnitude greater than those in the vacuum nanogap.

Chapter 5 demonstrates the evidence of quasi-Casimir coupling between the interfacial solid layers for simulation systems with non-adsorbed liquid atoms in the nanogap under weak solid–liquid interaction. Unlike the adsorbed solid-like liquid layers in Chapter 4, the liquid atoms move randomly and frequently collide with other liquid and interfacial solid atoms. Therefore, the mechanism of thermal energy transport includes both the contribution of solid atomic vibrations and liquid atomic collisions. With the aid of liquid atomic collisions, the phonon mismatch between the interfacial solid layers decreases, thus resulting in the maximum heat flux and thermal conductance in spite of the gap distance.

Chapter 6 summarizes the above results and discusses future works. Our findings in this thesis provided evidence of the new heat transfer mode of quasi-Casimir coupling, which can bring fundamental scientific insights into nanoscale heat transfer. The investigation of this new heat transfer mode will promote the development of heat transfer technologies at the nanoscale to achieve extremely high thermal energy transportation, attracting considerable interest in advanced applications.

## **Chapter 2**

# **2 Molecular dynamics simulation**

## **2.1 Introduction**

Molecular dynamics simulation is a computer simulation method of the physical movements of molecules. It is also a classical and deterministic process of simulation that uses potential energy functions to model the essential interaction of molecules. Due to the small time scale, the experiments are challenging and complex to achieve in micro and nanoscale systems. In this case, molecular dynamics simulation becomes a powerful and potential tool to study and provide solutions to phenomena and challenges at the nanoscale. MD is an experimental, numerical method with the atomic time scale of femtoseconds; this time region covers dynamics in the nano-region and makes the time to process the dynamics extremely small. Because of the increasing computational resources for modern computing, simulation time is still insufficient to observe molecules' dynamics in a suitable and desired time frame. The trajectories of molecules are determined by numerically solving Newton's equation of motion for a system of interacting particles, where forces between the particles and their potential energies are calculated using interatomic potentials or molecular mechanics force fields. A flow chart of the main steps of MD simulations is shown in Fig. 2.1. These steps will be explicitly explained in the following sections.

The origins of molecular dynamics are rooted in the atomism of antiquity. The significance of the solution to the many-body problem was noticed by Laplace [76].

MD simulation is a technique whose emergence was a predictable eventuality. Only a few years after the first digital computers emerged, the first MD steps were taken [77–79]. The  $N$ -body problem originated in the dynamics of the solar system, and the general problem turns out to be insoluble for three or more bodies. Quantum mechanics took over the microscopic world after the atomic nature of matter was confirmed. The situation got much more confusing because even the constituent particles seemed to have an undefined existence. However, a great deal of the behavior of matter in its many states can still be explained in classical terms, and the classical  $N$ -body problem is vital for understanding matter at the microscopic level. MD takes up the responsibility of numerically solving this problem. A considerable measure of success was achieved from statistical mechanics for systems in thermal equilibrium, especially from a conceptual standpoint. Statistical mechanics provides a theoretical description based on the partition function of a system in equilibrium. There are no quantitative solutions unless severe approximations are introduced, and even then, it is necessary to assume an extensive system. In many kinds of simulations, MD aid in filling in the gaps on the equilibrium side.

The topic of how simulation relates to physical theory emerges. The theoretical manipulation pervades throughout university education, which serves as a repository for highly idealized issues suitable to a closed-form solution. As we know, the theory relies extensively on analytical and numerical approximation, but this is often unregulated, making it challenging to prove trustworthiness. Therefore, simulation is based on fundamental theoretical foundations, but it seeks to eliminate much of the approximation generally associated with theory instead of relying on a more complex calculational effort.

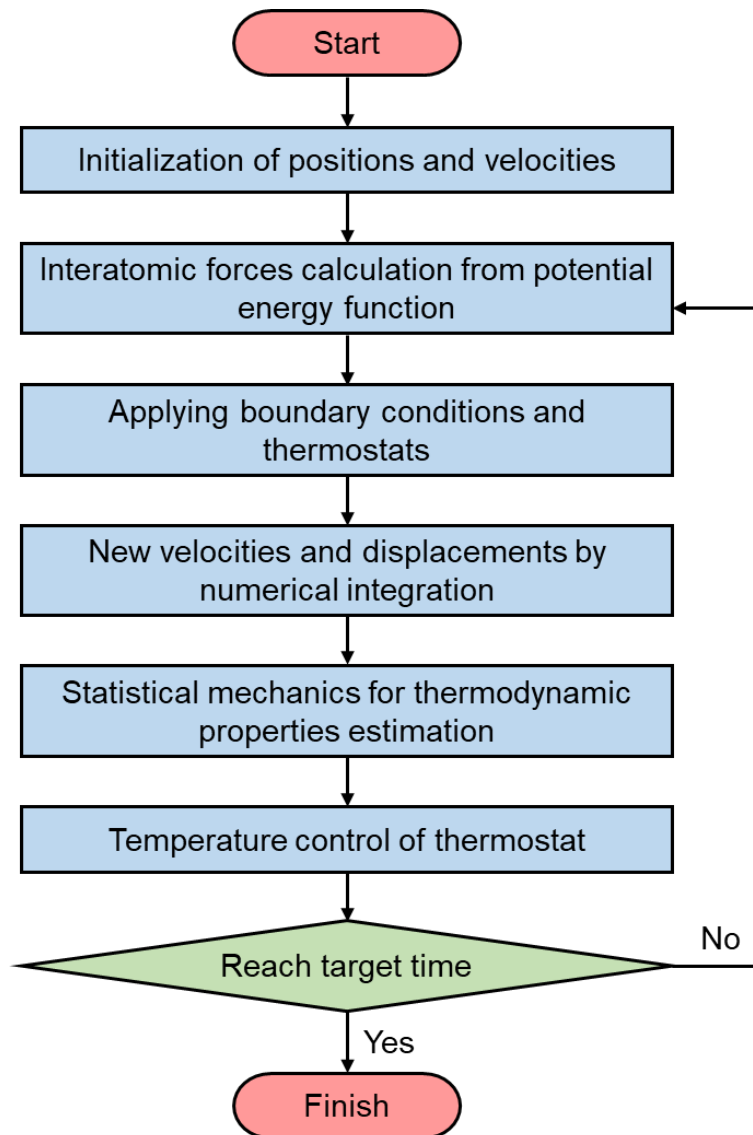


**Fig. 2.1** Flow chart for MD simulation algorithm.

In addition to MD, classical Monte Carlo [80,81], quantum-based techniques involving path-integral [82,83], MD combined with electron density-function theory [84,85], and discrete approaches such as cellular automata and the lattice-Boltzmann method [86] have all been developed over the years and are relevant for work at the molecular level. When a plausible model can recreate and anticipate experimental observation, understanding is accomplished in the simulation context. In order to

explain experiments, further research may lead to improvements in the model or its replacement, but this is not different from how science is practiced in the broader context. Simulation is very significant in education, and it is easy to understand how interactive computer simulations of the natural phenomenon may enhance any scientific presentation. Simulation is unrivaled as a complement to experimentation, a technique of strengthening theoretical discussion, or a tool for establishing hypothetical worlds. Simulation can be used to help overcome some of the more paradoxical concepts encountered even at a relatively fundamental level, especially in a conceptually difficult discipline like physics. MD has the ability to bring the entire invisible universe of the molecule to life, an experience that is equally rewarding for the expert scientist as it is for the complete tyro. However, simulation must be kept honest because seeing is believing, and animated displays, regardless of their veracity, can be quite convincing.

## **2.2 Overview of molecular dynamics simulation system**

The MD simulation method was applied to simulate thermal energy transport across the nanogap between the two planar solid walls and verify the existence of quasi-Casimir phonon heat transfer. The three kinds of MD simulation systems were adopted in this thesis. In all simulation cases, the dimensions of the simulation cell are  $L_x = 5.552$  nm,  $L_y = 3.847$  nm, and  $L_z = 1.813$ – $4.165$  nm. Each solid wall consists of four layers of atoms settled as  $\langle 111 \rangle$ -oriented face-centered cubic lattices. The solid walls are composed of platinum atoms, and the liquid or vapor confined between two solid walls is made of argon atoms. The outermost layers of the heating and cooling walls were maintained at the temperature of 120–300 K and 100 K, respectively.

In chapter 3, the heating and cooling solid walls were separated by a vacuum nanogap  $D$  of 0–0.784 nm. The gap distance was modulated to confirm the existence of quasi-Casimir coupling between two interfacial solid layers. In chapter 4, the two parallel solid walls were separated by a distance  $D$  of 0.392–2.352 nm. Comparing the simulation systems with the vacuum gap, the liquid layers were adsorbed on the solid surfaces, resulting in a minor distance  $d$  of 0–2.057 nm. In chapter 5, the gap distance  $D$  between two solid walls ranges from 0.392–1.176 nm. The non-adsorbed liquid atoms were confined in nanogap between two solid walls under the weak solid–liquid interaction. The liquid atoms move randomly and collide with other liquid and interfacial solid atoms. Accordingly, the new heat transfer mode was investigated by modeling the above three kinds of MD simulation systems.

## 2.3 Molecular dynamics simulation method

### 2.3.1 Intermolecular potentials

The interatomic potential defines how the atoms and molecules interact in the system. In this study, we have utilized non-bonded Lennard–Jones potential. The solid–solid and liquid–liquid interactions are expressed by the Lennard–Jones potential as follows:

$$\phi(r_{ij}) = 4\varepsilon \left[ \left( \frac{\sigma}{r_{ij}} \right)^{12} - \left( \frac{\sigma}{r_{ij}} \right)^6 \right] \quad (2-1)$$

where  $r_{ij}$  is the distance between two atoms  $i$  and  $j$ ,  $\sigma$  is the length parameter, and  $\varepsilon$  is the energy parameter. The parameters are  $\sigma = \sigma_l = 3.405 \text{ \AA}$ ,  $\varepsilon = \varepsilon_l = 1.67 \times 10^{-21}$

J for the liquid–liquid interaction of argon, and  $\sigma = \sigma_s = 2.475 \text{ \AA}$ ,  $\varepsilon = \varepsilon_s = 8.35 \times 10^{-20} \text{ J} (\approx 50\varepsilon_l)$  for solid–solid interaction of platinum.

For the solid–liquid interaction, the following modified LJ potential is utilized:

$$\phi_{sl}(r_{ij}) = 4\varepsilon_{sl} \left[ \left( \frac{\sigma_{sl}}{r_{ij}} \right)^{12} - \beta \left( \frac{\sigma_{sl}}{r_{ij}} \right)^6 \right] = 4\alpha \sqrt{\varepsilon_l \varepsilon_s} \left[ \left( \frac{\sigma_{sl}}{r_{ij}} \right)^{12} - \beta \left( \frac{\sigma_{sl}}{r_{ij}} \right)^6 \right] \quad (2-2)$$

where  $\sigma_{sl} = (\sigma_l + \sigma_s)/2$ , and the energy parameter  $\varepsilon_{sl}$  is given by  $\varepsilon_{sl} = \alpha \sqrt{\varepsilon_l \varepsilon_s}$  based on the Lorentz-Berthelot combining rule [87,88]. Here,  $\alpha$  is the potential energy factor indicating the strength of hydrophilic interaction and  $\beta$  is the potential energy factor indicating the attraction for hydrophobic interaction. Eq.(2-2) is a modified form of the LJ potential, which is a combination of the potential models used by Din and Michaelides [89] as well as by Barrat and Bocquet [90]. The potential distribution of a classic LJ model as a function of intermolecular distance is shown in Fig. 2.2. In this work, the values of both  $\alpha$  and  $\beta$  with responding values of the contact angle are taken from Nagayama’s study for the droplet formation on the substrate [91].

### 2.3.2 Intermolecular force

The coordinate components of the position vector  $r_i$  for the atom  $i$  are  $x_i, y_i, z_i$ . The force exerted by atom  $i$  on atom  $j$  is denoted by  $F_{ij}$  and its components in  $x, y, z$  directions are  $F_{x,ij}, F_{y,ij}, F_{z,ij}$ . The unit vectors in the  $x, y, z$  directions of this Cartesian coordinate system are  $e_x, e_y, e_z$ . Then, the position vector  $r_i$  of the atom  $i$  can be expressed as

$$r_i = x_i e_x + y_i e_y + z_i e_z . \quad (2-3)$$

The force obtained from the potential is given as

$$F_{ij} = -\nabla_i \phi_{ij} , \quad (2-4)$$

$$\nabla_i = e_x \frac{\partial}{\partial x_i} + e_y \frac{\partial}{\partial y_i} + e_z \frac{\partial}{\partial z_i} . \quad (2-5)$$

The distance between atoms  $i$  and  $j$  is

$$r_{ij} = |r_i - r_j| = \sqrt{(x_i - x_j)^2 + (y_i - y_j)^2 + (z_i - z_j)^2} . \quad (2-6)$$

Finally, the components of  $F_{ij}$  in  $x$ ,  $y$ ,  $z$  directions can be derived by

$dr_{ij}/dx_i = (x_i - x_j)/r_{ij}$  as follows:

$$F_{x,ij} = -\frac{d\phi(r_{ij})}{dr_{ij}} \frac{x_i - x_j}{r_{ij}} , \quad (2-7)$$

$$F_{y,ij} = -\frac{d\phi(r_{ij})}{dr_{ij}} \frac{y_i - y_j}{r_{ij}} , \quad (2-8)$$

$$F_{z,ij} = -\frac{d\phi(r_{ij})}{dr_{ij}} \frac{z_i - z_j}{r_{ij}} . \quad (2-9)$$

Molecular dynamics simulation applies Newton's equation of motion to determine the velocity, position, and trajectories of atoms or molecules in an ensemble. Newton's second law is given by

$$\frac{d^2 r_i}{dt^2} = \frac{F_i}{m} , \quad (2-10)$$

where  $r_i$  is the position of atom  $i$ ,  $t$  is the time,  $m$  is the mass of atom  $i$ , and  $F_i$  is the total force acting on atom  $i$ .

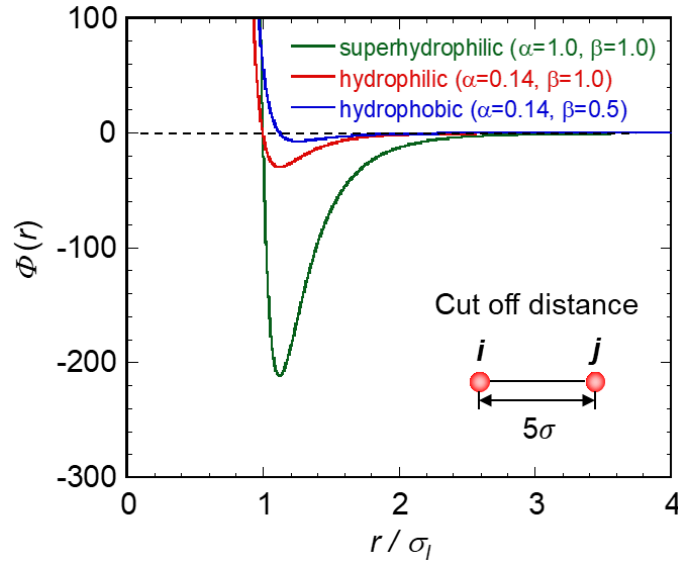


Fig. 2.2 LJ potential as a function of intermolecular distance.

### 2.3.3 Integration methods

Molecular dynamics simulation is a time integration method where positions and velocity are determined with the trajectory of the molecules and atoms obtained with time. In this work, the velocity Verlet algorithm was utilized in each molecular dynamics simulation [92], which is based on  $r(t)$ ,  $v(t)$ , and  $a(t)$  to obtain the next position and velocities. In this algorithm, the position and velocities are derived from the Taylor series of expansion as follows:

$$r_i(t + \Delta t) = r_i(t) + v_i(t)\Delta t + \frac{1}{2} \frac{F_i(t)}{m} (\Delta t)^2 + O((\Delta t)^3), \quad (2-11)$$

$$r_i(t - \Delta t) = r_i(t) - v_i(t)\Delta t + \frac{1}{2} \frac{F_i(t)}{m} (\Delta t)^2 + O((\Delta t)^3). \quad (2-12)$$

where  $O(\Delta t^4)$  is the higher-order term. The sum and difference of the above two equations are

$$r_i(t + \Delta t) + r_i(t - \Delta t) = 2r_i(t) + \frac{F_i(t)}{m} (\Delta t)^2 + O((\Delta t)^4), \quad (2-13)$$

$$r_i(t + \Delta t) - r_i(t - \Delta t) = 2v_i(t)\Delta t + O((\Delta t)^3). \quad (2-14)$$

Then, we can obtain the coordinates at  $t + \Delta t$  and velocities at  $t$  as follows:

$$r_i(t + \Delta t) = 2r_i(t) - r_i(t - \Delta t) + \frac{F_i(t)}{m} (\Delta t)^2 + O((\Delta t)^4). \quad (2-15)$$

The Verlet algorithm does not use velocity to determine a solution to the atomic position for the next time step. The velocity is approximated using the forward and backward positions as

$$v_i(t) = \frac{1}{2\Delta t} \{r_i(t + \Delta t) - r_i(t - \Delta t)\} + O((\Delta t)^2). \quad (2-16)$$

One disadvantage of the Verlet algorithm is that it requires storing in memory two sets of positions at  $t$  and  $t + \Delta t$ . Therefore, the velocity Verlet algorithm is utilized to reformulate the expansions. This algorithm initially uses the positions, velocities and acceleration at the current time to calculate the new positions at  $t + \Delta t$ . Based on the new positions, the accelerations at  $t + \Delta t$  are calculated. Then, new velocities are found from current velocity and acceleration and forward acceleration as follows:

$$r_i(t + \Delta t) = r_i(t) + v_i(t)\Delta t + \frac{1}{2} \frac{F_i(t)}{m} (\Delta t)^2, \quad (2-17)$$

$$v_i(t + \Delta t) = v_i(t) + \frac{1}{2} \frac{F_i(t + \Delta t) + F_i(t)}{m} \Delta t. \quad (2-18)$$

### 2.3.4 Thermodynamic ensembles

Molecular dynamics simulations are based on the frameworks of statistical mechanics and thermodynamics. MD corresponds to the ensemble average of the microscopic properties of a large number of particles in a molecular system obtained by integrating the equation of motion at a particular thermodynamics state. In statistical mechanics, an ensemble is described as the collection of possible microscopic states of a molecular system satisfying the requirements of a particular thermodynamic state. Usually, the thermodynamic state of the system is characterized by several parameters, such as particle number ( $N$ ), volume ( $V$ ), temperature ( $T$ ), energy ( $E$ ), and pressure ( $P$ ). In this work, the two ensembles used in statistical mechanics include canonical ensemble ( $NVT$ ) and microcanonical ensemble ( $NVE$ ).

The  $NVT$  ensemble represents the combination of possible thermodynamic states of an atomic system in thermal equilibrium using a heat bath at a constant temperature. The system can exchange energy with its environment so that the total energy is a function of time. In this ensemble, the temperature is controlled by the temperature scaling in initialization and thermostats during the data storage stage. The canonical ensemble is named  $NVT$  because the particle number, volume, and temperature are constant.  $NVT$  does not control the pressure of the system.

The *NVE* ensemble describes the combination of possible thermodynamic states of an atomic system at specified total energy, which is called *NVE* because the particle number, volume, and energy keep constant. The equation of motion is solved without any control of temperature and pressure, so the system is isolated from its environment, preventing energy exchange. *NVE* ensemble represents an ideal thermodynamic situation. It is difficult to fix the energy in practice due to ambiguities in temperature, pressure, entropy, etc. For equilibrium simulation, the *NVE* ensemble is not recommended because the desired temperature might not be achieved without any control of temperature using a heat bath. Moreover, the *NVE* ensemble is very useful for a system at constant energy, consisting of  $N$  particles in an insulated box where heat flows do not come in or get out.

### 2.3.5 Periodic boundary condition

Due to the finite and infinite systems being entirely dissimilar, there is no unique answer to the question of how large a relatively tiny system must be to produce outcomes that closely match the behavior of an infinite system. The simulation is carried out in a specific type of container, and it is tempting to regard the container walls as strict boundaries that atoms collide with as they try to escape the simulation region. Periodic boundary conditions can be used to create a system that is bounded but free of physical walls, shown in Fig 2.3. The introduction of periodic boundaries is functionally equivalent to considering an infinite, space-filling array of identical copies of the simulation region. An atom that exits the simulation region through a specific bounding face immediately rejoins the region through the opposite face. Atoms located

within the distance  $r_c$  of the boundary interact with other atoms in an adjacent copy of the system or with other atoms near the opposite boundary. Another approach to thinking about periodic boundaries is to imagine the region being mapped onto a four-dimensional torus. There are no physical boundaries, as is evident. It is feasible to model systems that are effectively bounded but spatially homogeneous in terms of boundaries in this way. Both the integration of the equations of motion and the interaction computations must account for the wraparound impact of the periodic boundaries. The coordinates must be inspected after each integration step, and if an atom is discovered to move outside the region, its coordinates must be modified to bring it back inside.

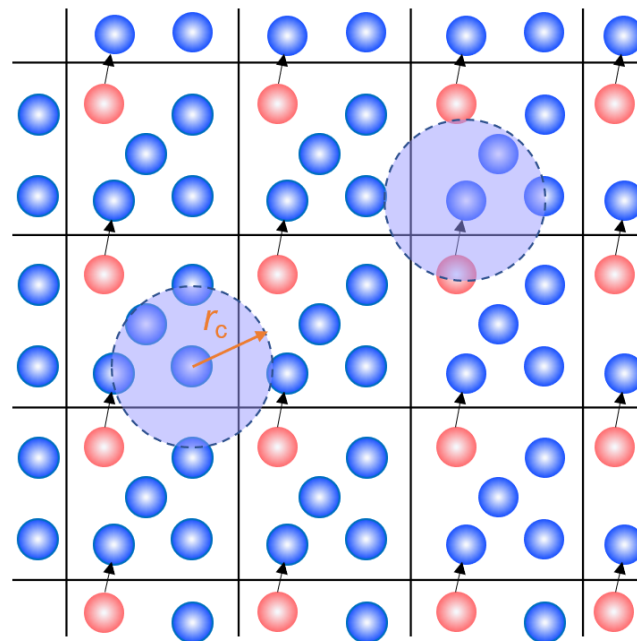


**Fig. 2.3** Periodic boundary conditions (the two-dimensional case is shown).

Periodic boundaries are easiest to manage when the region is rectangular in two dimensions or a rectangular prism in three dimensions. The goal of adopting alternative

region shapes is to maximize the volume to surface ratio and increase the maximum distance between atoms before periodic ambiguity occurs, with the sphere being the most desirable three-dimensional shape but not space-filling. Another motivation for using more complicated region shapes is to model crystalline structures with non-orthogonal axes. If there are strong connections between atoms separated by distances approaching the region size, problems will occur since periodic wraparound can generate spurious effects. For example, the vibration of an atom produces sound waves, if the disturbance is not properly dampened, it can propagate throughout the system and finally impact the atom. Even with periodic boundaries, finite-size effects are still present and depend on the kind of system and the properties of interest. At a minimum, the size should be greater than the range of any significant correlations, but even in larger systems, there may be more subtle effects.

### **2.3.6 Thermostating**

Molecular dynamics simulation is performed in the microcanonical ensemble ( $NVE$ ), including the constant number of atoms ( $N$ ), the volume of the system ( $V$ ), and the total number of energy ( $E$ ). The control of the system temperature, also known as the canonical ensemble, is an alternative to the microcanonical ensemble. Temperature control in the  $NVE$  ensemble can also be accomplished by controlling the kinetic energy of the system, a process known as velocity rescaling. A thermostat is used to keep the temperature at a constant value; all fluids or groups in a system can be controlled by a thermostat. Taken the instant temperature (which is not the ensemble average temperature) for system  $T_1$  and the adjusted temperature of the ensemble  $T_2$ . Then, the

temperature of the ensemble can be controlled by the velocity rescaling method as follows:

$$v_i' = v_i \sqrt{T_2/T_1} \quad (2-19)$$

where  $v_i$  is the instant velocity of atom  $i$  and  $v_i'$  is the new velocity of atom  $i$  after performing the velocity rescaling method.

## 2.4 Computational details

### 2.4.1 Density profiles

The density profiles are obtained by simply allocating the mass of the atoms into respective bins and averaging with the bin volume as follows:

$$\rho = \frac{N \cdot m}{V}, \quad (2-20)$$

where  $N$  is the molecular number in the bin,  $m$  is the mass of molecular, and  $V$  is the volume of the bin.

### 2.4.2 Temperature profiles

The temperature of each bin in the steady state is calculated based on the Equipartition theorem as:

$$T = \frac{1}{N} \sum_{n=1}^N \frac{2}{3k_B} \sum_{i=1}^3 \frac{1}{2} m (v_{n,i} - \bar{v}_i)^2, \quad (2-21)$$

where  $N$  is the particle number in the bin,  $k_B$  is the Boltzmann constant,  $m$  is the mass of the solid atom,  $v_{n,i}$  is the velocity of atom  $n$  in the  $i$  ( $=x, y, z$ ) direction, and  $\bar{v}_i$  is the mean velocity of the solid atoms in the bin.

### 2.4.3 Atomic vibrational characteristics

The atomic vibrational displacements and frequencies are measured using a wave graph to observe the vibrational properties of the atoms. The wave graphs are obtained by outputting the positions of the atoms from the MD simulation data and conducting signal processing [93]. The equilibrium position of the atoms in the  $z$ -direction is calculated by:

$$\bar{z} = \frac{1}{t_f - t_0} \sum_{t_0}^{t_f} z_{i,t}, \quad (2-22)$$

where  $z_{i,t}$  is the position of atom  $i$  at time  $t$ , and atom  $i$  is located at the center of each solid layer;  $t_0$  is the initial time at which the data output begins, and  $t_f$  is the long finite time for 10,000 time steps. The original vibrational displacements of atom  $i$  are calculated as  $\Delta z_{i,t} = z_{i,t} - \bar{z}$ , which is a function of time. Then, we calculate the Fourier transform of the original vibrational displacements to obtain the distribution of signal power in the frequency domain (power spectrum). The dominant frequency band is selected to perform signal filtering on the original vibrational displacements and obtain the regular wave graphs. The peak amplitude and frequency are determined from the wave graphs.

#### 2.4.4 Vibrational density of states

The velocities of all the atoms in the interfacial layers obtained from the MD simulation data, are used to calculate the vibrational density of states (VDOS) [42,94] of the interfacial layers by the Fourier transform of the velocity autocorrelation function

$$VDOS(\omega) = \int_0^{\infty} \langle \vec{v}(t) \vec{v}(0) \rangle e^{-i\omega t} dt. \quad (2-23)$$

Here,  $\omega$  is the angular frequency, and  $v(t)$  is the atomic velocity at time  $t$ .

#### 2.4.5 Net heat flux

The heat flux passing through the system is acquired as follows:

$$q = \frac{1}{A} \cdot \frac{\partial E}{\partial t}, \quad (2-24)$$

where  $A$  is the cross-sectional area of the  $x$ - $y$  plane,  $\partial E / \partial t$  is the rate of heat transfer in the heating or cooling thermostat, and  $E$  is the cumulative energy of the heating ( $E_H$ ) or cooling ( $E_C$ ) thermostat.

#### 2.4.6 Local heat flux

The simulation system is divided into eight bins along both the  $x$ - and  $z$ -directions to calculate the average local heat flux by Irving–Kirkwood (I–K) method of each layer, as shown in Fig. 2.4(a). The components of thermal energy are calculated to estimate the

effective energy of heat transfer across a vacuum gap along the z-direction by using the I-K equation [95,96],

$$J_q = J_k + J_p + J_i = \frac{1}{V} \sum_i E_i^k v_{z,i} + \frac{1}{V} \sum_i \phi_i v_{z,i} + \frac{1}{2V} \sum_i \sum_j (F_{ij} v_j) r_{z,ij}, \quad (2-25)$$

where  $J_k$  and  $J_p$  represent the energies transported by the molecules with kinetic and potential energy, respectively, and  $J_i$  represents the intermolecular energy transfer.  $V$  is the volume of the solid layer,  $E_i^k$  is the kinetic energy of molecule  $i$ ,  $\phi_i$  is the potential energy of molecule  $i$ ,  $v_{z,i}$  is the velocity component of molecule  $i$  along the z-direction,  $F_{ij}$  is the intermolecular force between molecules  $i$  and  $j$ ,  $v_j$  is the velocity of molecule  $j$ , and  $r_{z,ij}$  is the distance between molecules  $i$  and  $j$  along the z-direction. Eq. (2-25) gives the heat flux averaged over a control volume  $V$  of each solid layer (see Fig. 2.4(b)).

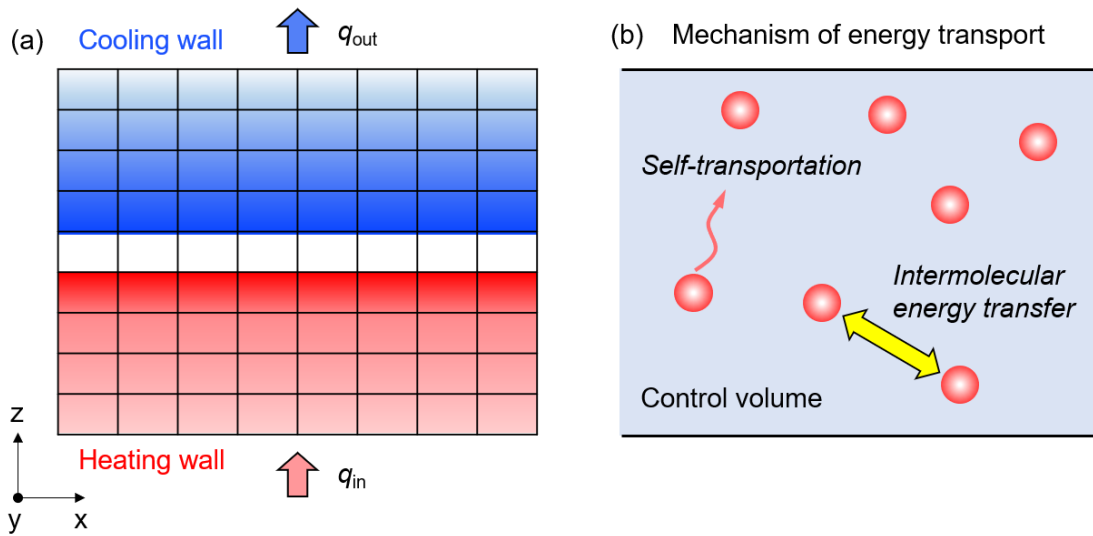


**Fig. 2.4** (a) Computational domain is divided into eight bins along both the x- and z-directions. (b) Mechanism of energy transport in a control volume.



## **Chapter 3**

# **3 Quasi-Casimir heat transfer across a vacuum gap**

## **3.1 Introduction**

In vacuum, thermal energy is transported by photons (thermal radiation) but not phonons. Recent studies, however, indicated that phonon heat transfer across a vacuum gap is mediated by the quantum fluctuation of electromagnetic fields. Specifically, in the heat exchange between two objects separated by a nanoscale vacuum gap, phonons carry thermal energy more efficiently than photons. However, it remains unclear if phonons can propagate without electromagnetic fields. Here, we demonstrate that phonon transmission across a sub-nanometer vacuum gap can be induced by quasi-Casimir force subjected to the Lennard–Jones atoms using classical molecular dynamics simulation. The net heat flux across the vacuum gap increases exponentially as the gap distance decreases, owing to acoustic phonon transmission. The apparent local heat flux by I–K method, increases singularly at the interfacial layers, while that at the inner layers agrees well with the net heat flux. These findings provide evidence of the strong thermal resonance induced by quasi-Casimir coupling between the interfacial layers. Thus, we conclude that the quasi-Casimir coupling induced by intermolecular interaction is a heat transfer mode for phonon heat transfer across a vacuum gap in nanoscale.

## 3.2 Simulation method

Consider two solid walls that consist of monoatomic molecules connected by springs, which correspond to the harmonic potential at heating and cooling walls, as illustrated in Fig. 3.1(a). The two solid walls are bonded with a quasi-Casimir coupling characterized by the spring coupling in a vacuum gap. This quasi-Casimir coupling acts as the channel for phonon transmission in the vacuum gap, which is similar to acoustic phonon tunneling in an evanescent electric field, thus providing an additional channel to enhance thermal energy transfer across the vacuum gap [30]. A constant heat flux  $q$  passes through the vacuum gap with thermal conductance  $G$  from the interfacial layer of the heating wall at a high temperature  $T_{\text{Hi}}$  to that of the cooling wall at a low temperature  $T_{\text{Ci}}$ .

The MD technique [58,95,97–104] was applied to simulate thermal energy transport across the sub-nanometer vacuum gap between the heating wall (red wall heated by a thermostat layer of 120–300 K) and the cooling wall (blue wall cooled by a thermostat layer of 100 K). The velocity scaling method was used to maintain the temperatures of the heating and cooling thermostats [105]. The two parallel solid walls were separated by a gap distance  $D$  of 0–0.784 nm ( $0-2a$ ), where  $a$  denotes the lattice constant of platinum and is equivalent to 0.392 nm [106], as shown in Fig. 3.1(b). As  $D$  decreases, the strength of the intermolecular interactions between two solid walls in vacuum increases, which induces the quasi-Casimir coupling with high thermal energy transport, as will be described in Section 3.3.

The dimensions of the simulation cell are  $L_x = 5.552$  nm,  $L_y = 3.847$  nm, and  $L_z = 1.813-2.597$  nm. Each solid wall consists of four layers of atoms that are settled as

<111>-oriented face-centered cubic lattices. The solid walls are presumed to be composed of 2560 platinum atoms. Periodic boundary conditions are employed along the  $x$ - and  $y$ -directions. The solid–solid interaction is expressed by the Lennard–Jones potential using Eq. (2-1).

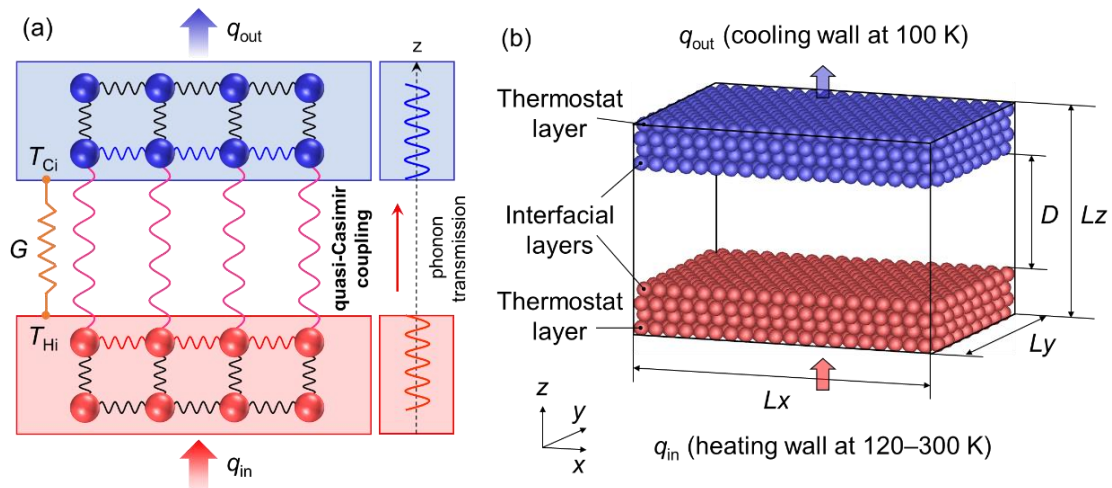


**Fig. 3.1** (a) Schematic of acoustic phonon transmission across a vacuum gap by quasi-Casimir coupling. (b) MD simulation system: heat exchange between two parallel solid walls separated by a gap distance  $D$ .

The equilibrium system at 100 K is simulated after achieving a steady state from the initial state for five ns. Subsequently, the NEMD simulation is performed from the equilibrium state to the steady state for 50 ns. In all of the NEMD simulations, the cumulative input and output energies  $E_H$  and  $E_C$  in the heating (120–300 K) and cooling (100 K) thermostats, respectively, are monitored. After the system achieves a steady state with constant heat flow ( $\Delta E = E_H - E_C \cong 0$ ) shown in Fig. 3.2, an extra un-steady NEMD simulation is conducted by switching off the cooling thermostat but operating the heating thermostat for five ns. The transient thermal behaviors are discussed in

Section 3.3.1. Further data analyses for the steady NEMD simulations are described in the next section.

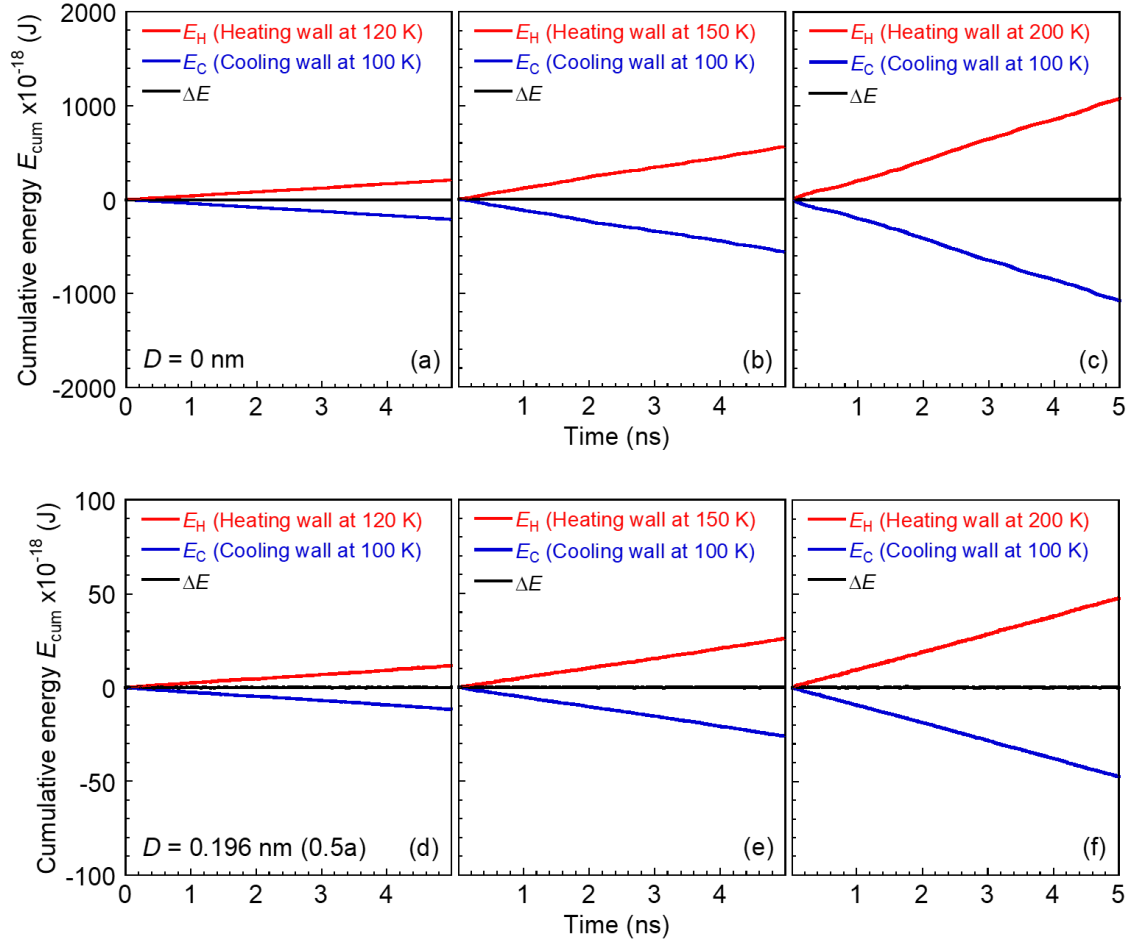


**Fig. 3.2** Cumulative input and output energy  $E_{cum}$  as a function of time  $t$  in the heating and cooling thermostats at different temperature difference  $\Delta T$ : (a–c) Constant gap distance  $D = 0$  nm; (d–f) constant  $D = 0.196$  nm ( $0.5a$ ).

The simulation system is divided into eight bins along both the  $x$ - and  $z$ -directions to obtain the temperature profile in the steady state for five ns. The local temperature  $T$  of each bin can be calculated by Eq. (2-21). The heat flux passing through the system is acquired by Eq. (2-24) from the mean value over the last 15 ns within a 50 ns time

window. The thermal conductance between the two solid walls is calculated by  $G = q / (T_{\text{Hi}} - T_{\text{Ci}})$ , where  $T_{\text{Hi}}$  is the temperature of the heating interfacial solid layer, and  $T_{\text{Ci}}$  is the temperature of the cooling interfacial solid layer.

The atomic vibrational displacements and frequencies are measured using a wave graph to observe the vibrational properties of the atoms at the positions (A2, A3, A4, and B2, B3, B4) shown in Fig. 3.3. The wave graphs are obtained by outputting the positions of the atoms from the MD simulation data of 10,000 time steps and conducting signal processing [93]. The equilibrium position of the atoms in the  $z$ -direction is calculated by Eq. (2-22). The original vibrational displacements of atom  $i$  are calculated as  $\Delta z_{i,t} = z_{i,t} - \bar{z}$ , which is a function of time. Then, we calculate the Fourier transform of the original vibrational displacements to obtain the distribution of signal power in the frequency domain (power spectrum). The dominant frequency band is selected to perform signal filtering on the original vibrational displacements and obtain the regular wave graphs. The peak amplitude and frequency are determined from the wave graphs.

The velocities of all the atoms in the interfacial layers obtained from the MD simulation data of 10,000 time steps, are used to calculate the VDOS [42,94] of the interfacial layers by the Fourier transform of the velocity autocorrelation function given by Eq. (2-23).

The simulation system is divided into eight bins along both the  $x$ - and  $z$ -directions to calculate the average local heat flux by I-K method of each layer. The components of thermal energy are calculated to estimate the effective energy of heat transfer across a vacuum gap along the  $z$ -direction by using the I-K equation in Eq. (2-25) [95,96].

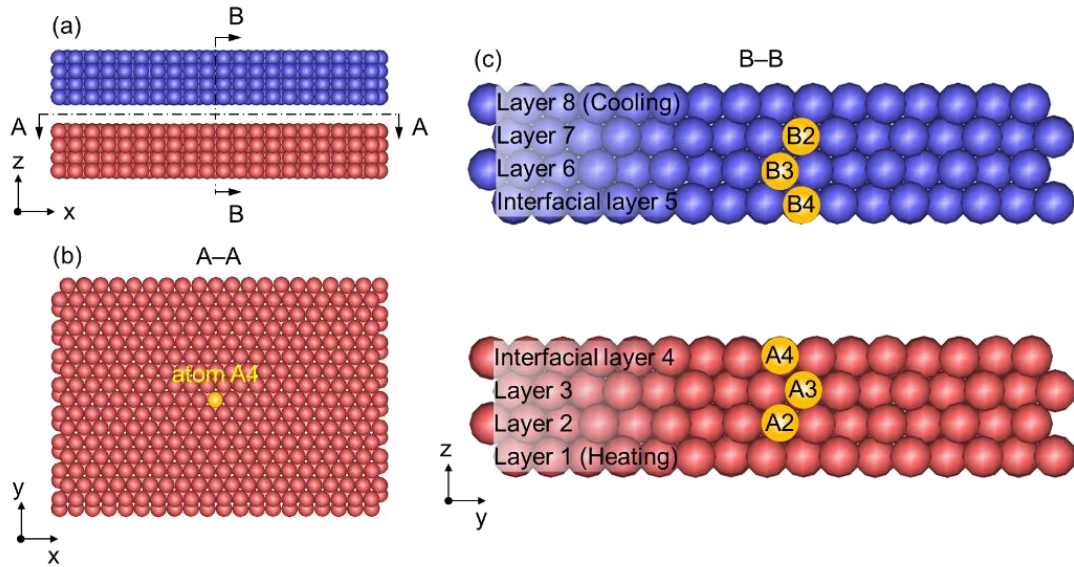


**Fig. 3.3** Positions of atoms selected to analyze the atomic vibrational characteristics from different views of the simulation model: (a) front view of the simulation model in the  $xz$ -direction; (b) atom A4 at interfacial layer 4 in the A–A directional view of the simulation model; (c) atoms A2, A3, A4 and B2, B3, B4 of the solid layers in the B–B directional enlarged view of the simulation model.

### 3.3 Results and discussion

#### 3.3.1 Transient thermal behavior in non-steady state

Since the temperature differences between the heating and cooling walls in the steady NEMD simulations can be maintained if the vacuum gap acts as the thermal insulation, we conducted the non-steady NEMD simulations to confirm if thermal energy can be transported from the heating wall to the cooling wall across the vacuum gap. The transient thermal behavior of the system is investigated based on the time history of the temperatures at the interfacial layers. The temperatures shown in Fig. 3.4 are obtained in the non-steady NEMD simulations by operating the heating thermostat but switching off

the cooling thermostat. The temperature difference between the interfacial layers of the

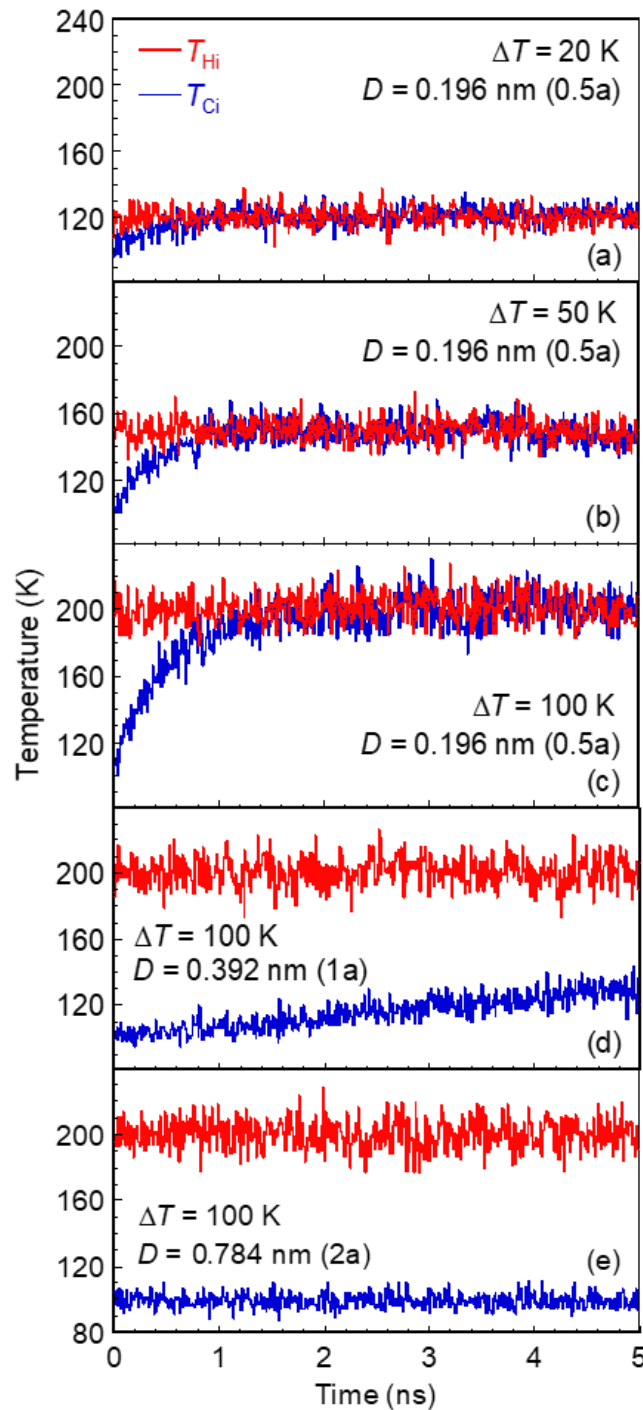


**Fig. 3.4** Thermal energy transport across a vacuum gap in non-steady NEMD simulations: (a–c) effects of  $\Delta T$  on the transient temperature of the interfacial layers at constant  $D = 0.5a$ ; (c–e) effects of  $D$  on the transient temperature of the interfacial layers at constant  $\Delta T = 100$  K.

heating and cooling walls separated by  $D = 0.5a$  is eliminated after a certain period of time within five ns, thus demonstrating the occurrence of thermalization between the two solid walls. This phenomenon indicates that energy must be transferred from the heating wall to the cooling wall across a vacuum gap, even for the Lennard–Jones atoms, in the absence of an electromagnetic field. The heat transfer between the two walls is enhanced with an increment in the temperature difference between thermostats  $\Delta T$  at  $D = 0.5a$ , as shown in Fig. 3.4(a)–(c), while diminishes with an increase in  $D$  at  $\Delta T = 100$  K as shown in Fig. 3.4(c)–(e), owing to the weakened interaction between the two interfacial layers.

### 3.3.2 Temperature profiles in steady state

The temperature profiles shown in Fig. 3.5 are obtained under the operation of the simultaneous heating and cooling thermostats after the NEMD system achieves a steady state, where the solid lines are a guide for the eye. Fig. 3.5(a)–(e) are results under the constant temperature difference between the two thermostats ( $\Delta T = 20$  K). In the case of  $D = 0$ , as shown in Fig. 3.5(a), a continuum temperature distribution is obtained from the cooling thermostat to the thermostat free layers, while a temperature jump is found between the heating thermostat and the neighboring thermostat free layer. This temperature jump is caused by the phonon mismatch between the thermostat and thermostat free layer owing to the dynamic rescaling of the thermostat [68,107], as shown in Fig. 3.6.

Increasing  $D$  from  $0.5a$  to  $2a$  ( $\Delta T = 20$  K), as shown in Fig. 3.5(b)–(e), the temperature distributes continuously in the inner layers, while discontinuously at the

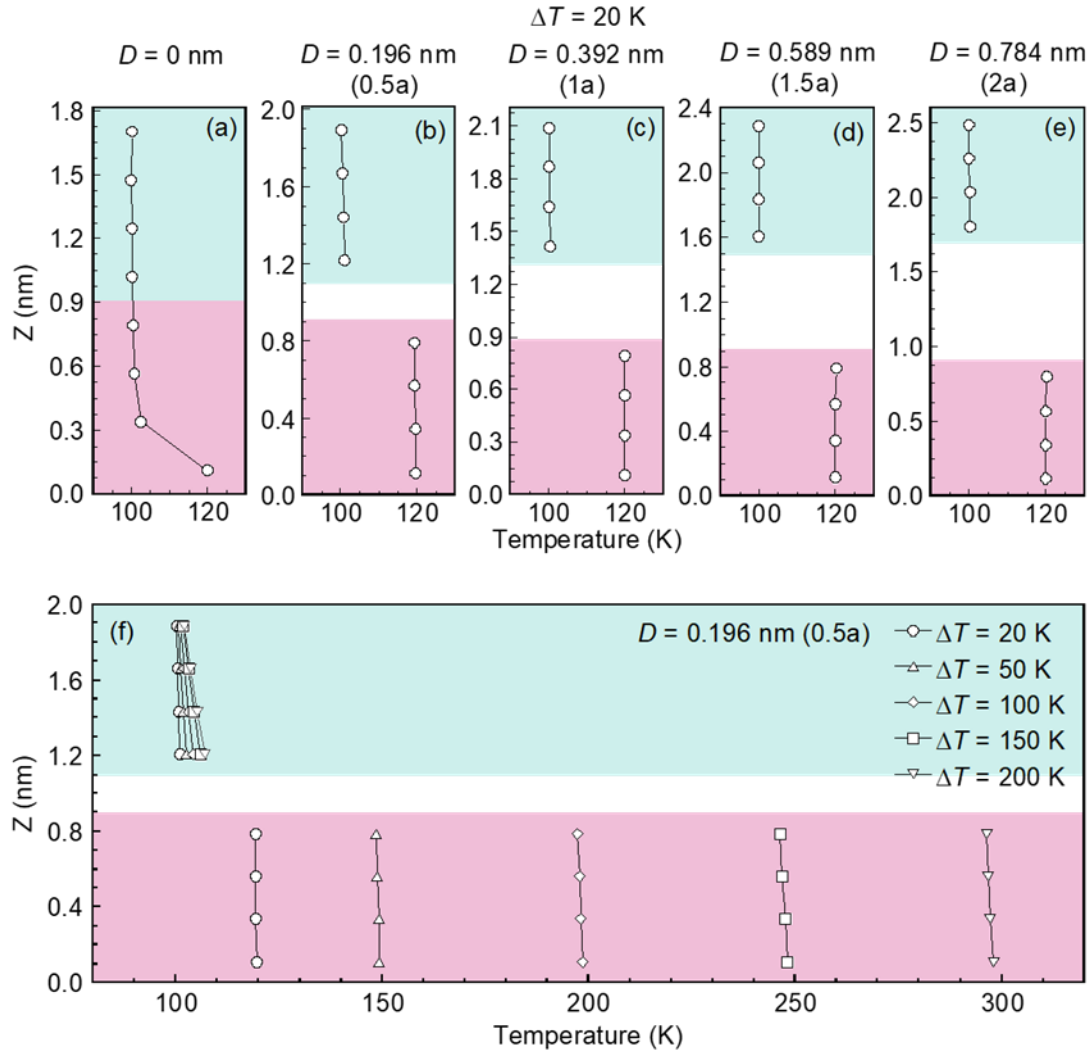


**Fig. 3.5** Temperature profiles of the solid walls in steady NEMD simulations: (a–e) varying  $D$  at constant  $\Delta T = 20$  K; (f) varying  $\Delta T$  at constant  $D = 0.196$  nm ( $0.5a$ ).

interfacial layers. The linear temperature distribution is obtained by the interactions of platinum atoms producing the natural phonon characteristics at the thermostat free layers. The temperature jump at the interfacial layers ( $T_{Hi} - T_{Ci}$ ) is nearly identical to  $\Delta T$  and independent of the gap distance  $D$ . In the case of  $D = 0.5a$ , as shown in Fig. 3.5(f), the temperature gradient of the heating wall is nearly same as that of the cooling wall, and  $T_{Hi} - T_{Ci}$  gets larger with an increment in  $\Delta T$ , showing the enhanced thermal energy exchange between the two solid walls.

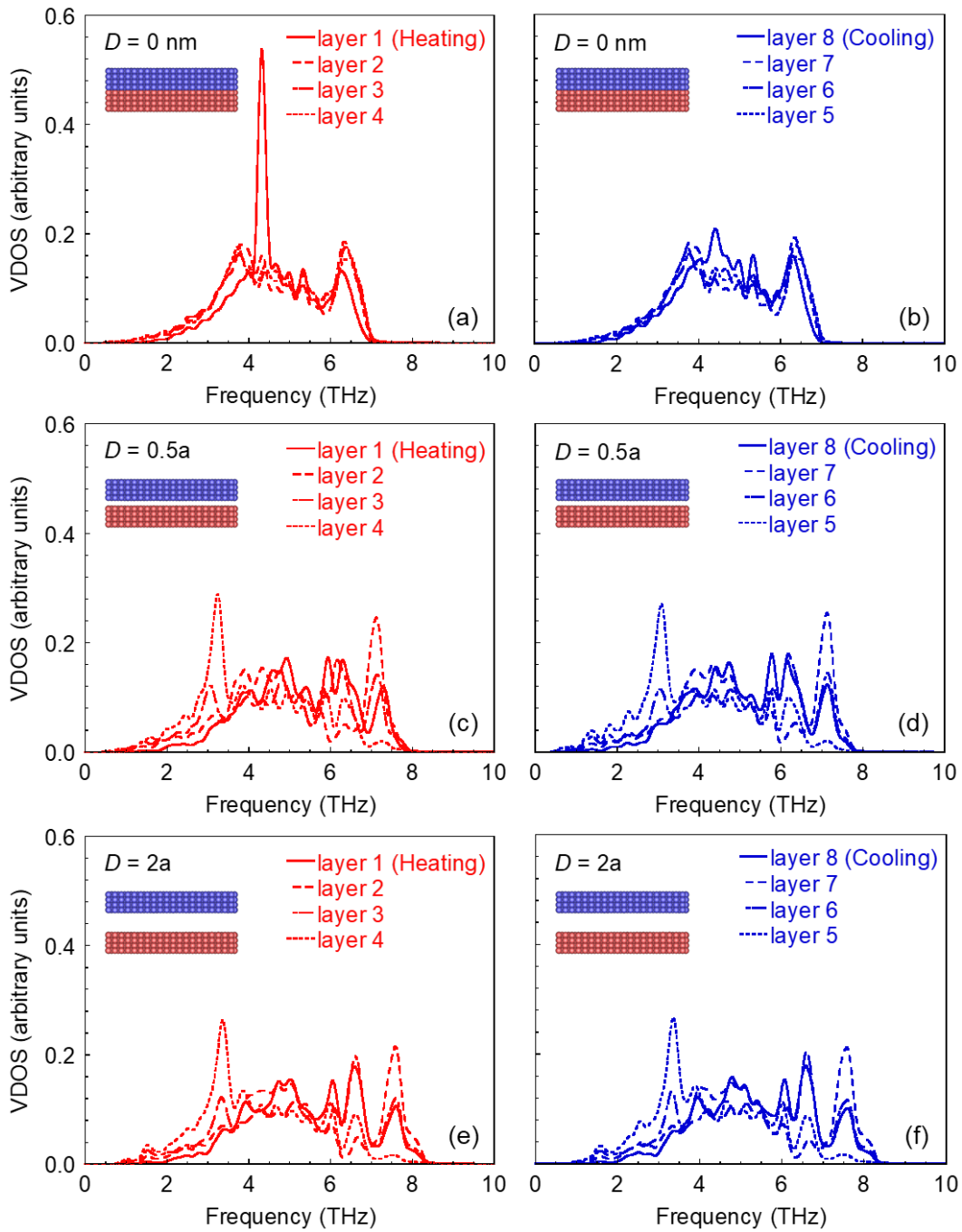


**Fig. 3.6** VDOSs of each layer at heating (left) and cooling (right) walls under  $\Delta T = 20$  K in the case of (a–b)  $D = 0$ , (c–d)  $D = 0.5a$  and (e–f)  $D = 2a$ .

### 3.3.3 Net heat flux and thermal conductance

In the steady state of the NEMD simulation, the net heat flux and thermal

conductance are obtained by conducting data sampling over a period of 15 ns. The net heat flux and thermal conductance in the sub-nanometer gap are approximately three to six orders of magnitude larger than that of blackbody radiation as a function of  $D$ , as shown in Fig. 3.7(a) and (b). These results give evidence of the existence of another heat transfer mode between the regimes of thermal radiation and heat conduction. This exponential heat transfer enhancement occurs owing to the strengthened intermolecular interaction between the two solid walls as  $D$  decreases. The heat flux and thermal conductance in the case of  $D = 0$  are larger than those for other cases of  $D$  due to the heat conduction in solid objects. Furthermore, the heat flux enhances with an increment in  $\Delta T$ , while  $\Delta T$  does not notably influence the thermal conductance, as shown in Fig. 3.7(c) and (d).

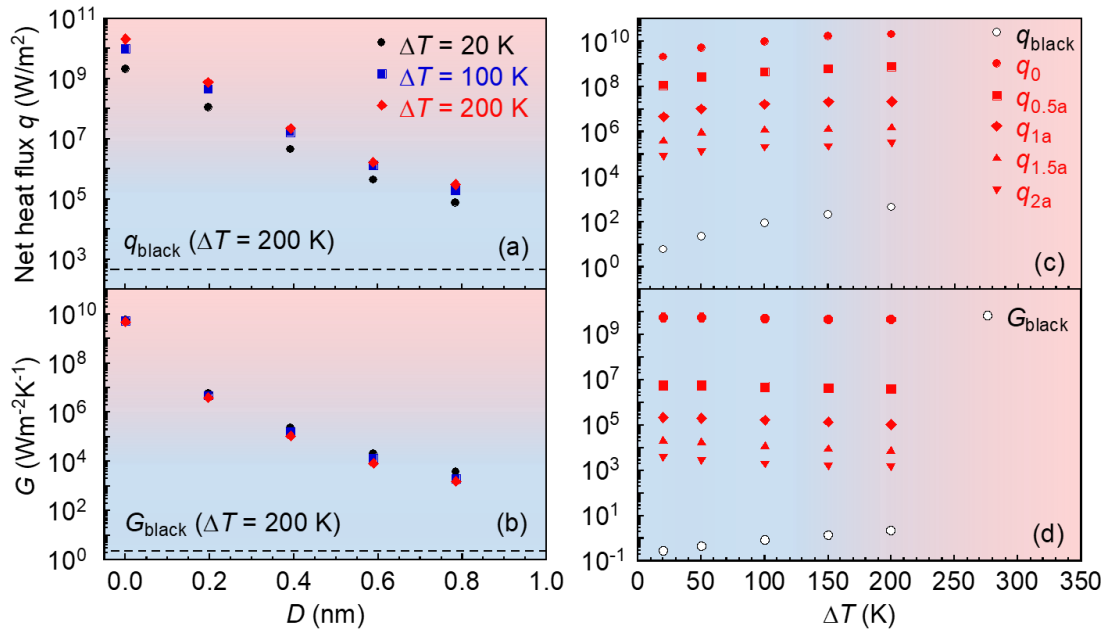


**Fig. 3.7** Effects of  $D$  on (a) net heat flux and (b) thermal conductance. Effects of  $\Delta T$  on (c) net heat flux and (d) thermal conductance.

### 3.3.4 Thermal resonance induced by quasi-Casimir coupling

To understand the mechanism of heat transfer enhancement with decreasing  $D$ , as shown in Fig. 3.7, we analyzed the atomic vibrational characteristics in a steady NEMD state under a constant  $\Delta T$  of 20 K. For  $D = 0.5a$ , the peak amplitudes of the interfacial atoms (A4 at the heating wall, B4 at the cooling wall) are significantly larger than those of the atoms (A2, A3, B2, B3) in the inner layers, as shown in Fig. 3.8 (b) and (f) and summarized in Table 3-1. Meanwhile, the vibrational frequencies of the interfacial atoms (A4, B4) are smaller than those of the inner layer atoms, as listed in Table 3-1. These deviations are unremarkable when  $D = 2a$  and  $5a$ , as shown in Fig. 3.8(c), (d), (g) and (h), while the peak amplitudes and frequencies of the inner layer atoms at  $D = 0$  are similar, as shown in Fig. 3.8(a) and (e). That is, when  $D$  is sufficiently small (several atomic diameters), the interfacial atoms are subjected to strong molecular interactions across the vacuum gap, which results in the thermal resonance induced by quasi-Casimir coupling.

This aspect can be proved by the perfectly overlapped vibrational displacements of the interfacial atoms A4 and B4 separated by the vacuum gap in Fig. 3.9(b) and (c), which show vibration behaviors similar to those of the inner layer atoms in the solid wall shown in Fig. 3.9(a). Therefore, the VDOSs based on the Fourier transform of the atomic velocity autocorrelation function [42,94] of solid layer 4 are consistent with those of layer 5, as shown in Fig. 3.9(e)–(h). Compared to the peaks of the VDOSs of the inner layers in the solid ( $D = 0$ ), those of the interfacial layers ( $D = 0.5a$  or  $2a$ ) are shifted toward the left of the low-frequency band. That is, the heat transfer across the sub-nanometer vacuum gap between the solid walls exhibits a trend similar to that of

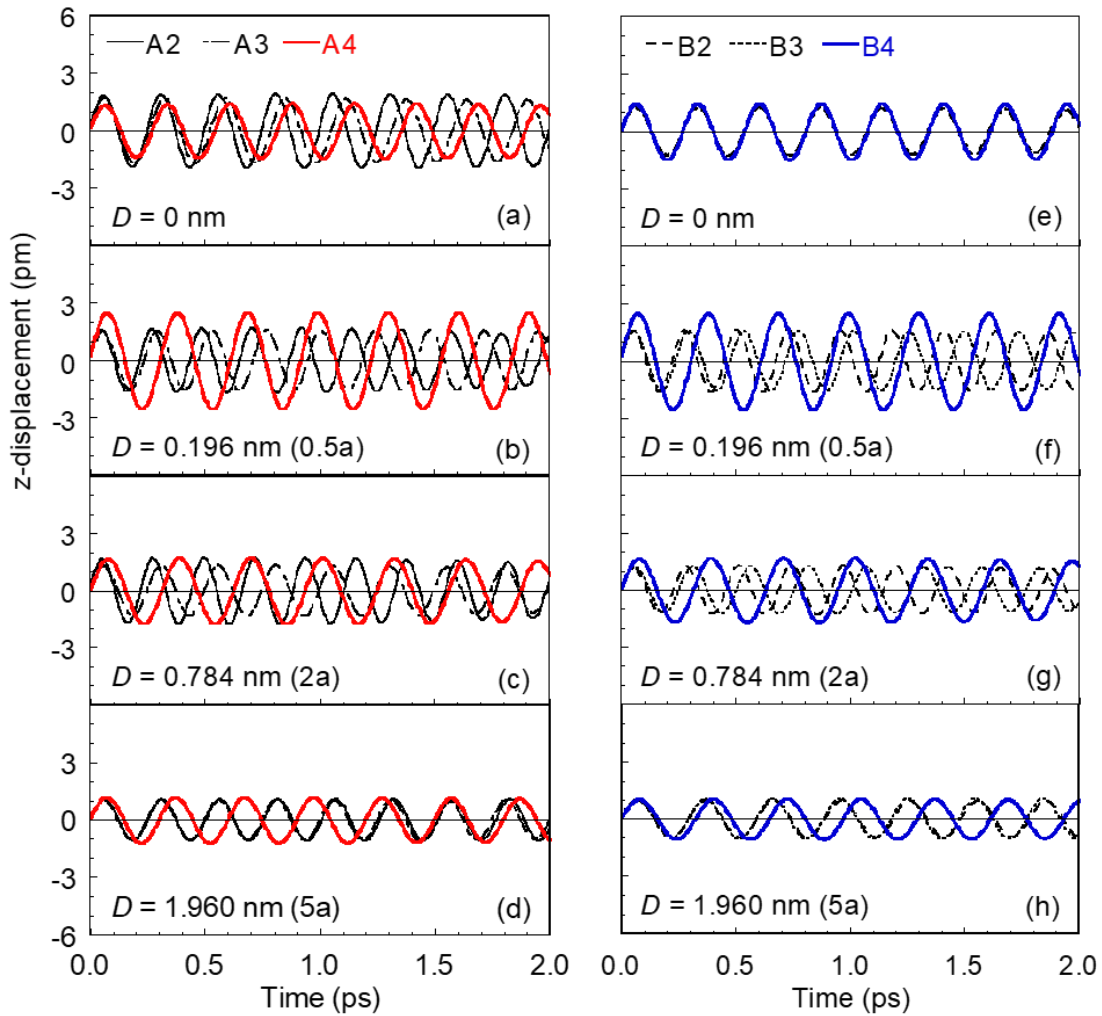


**Fig. 3.8** Effects of  $D$  on atomic vibrational displacements of layers in the heating and cooling walls at constant  $\Delta T = 20$  K: (a–c) vibrational displacements of atoms A2, A3, and A4 in the heating wall; (d–f) vibrational displacements of atoms B2, B3, and B4 in the cooling wall.

the solid walls without a gap, conducted through the acoustic phonons in the low-frequency band of 3–4 THz. The strong phonon coupling at the interfacial layers leads to the resonant excitation peaks of the VDOSs in the frequency band coinciding with the vibrational frequencies of the interfacial atoms A4 and B4, as summarized in Table 3-1. Moreover, the temperature difference  $\Delta T$  has slight effects on the vibrational

displacements of atoms A4, B4, and the VDOSs of the interfacial layers at the constant  $D = 0.5a$  (see Fig. 3.10). These results indicate that the gap distance  $D$  is the dominant factor governing the near-field heat transfer induced by the quasi-Casimir coupling.

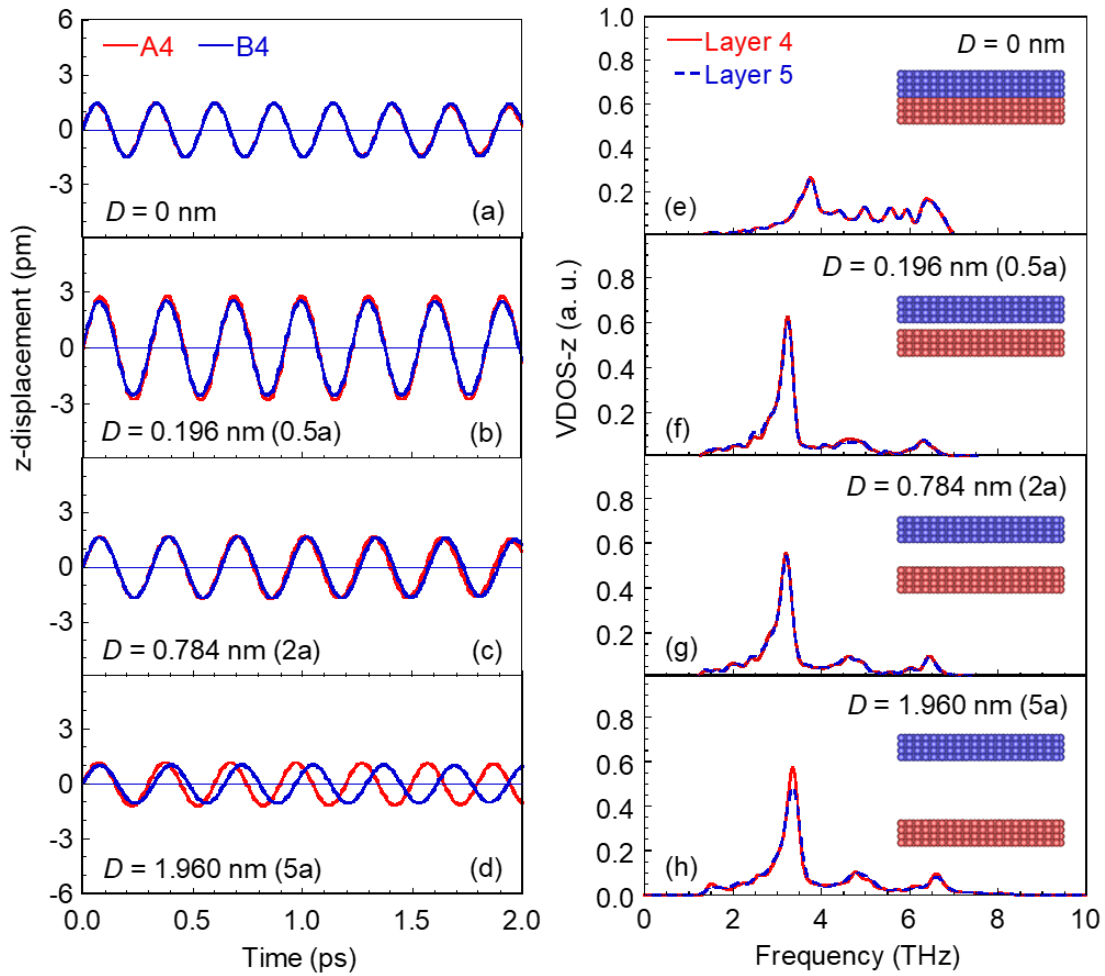


**Fig. 3.9** Effects of  $D$  on (a–d) the vibrational displacements of atoms A4 and B4 in the interfacial layers as well as (e–h) the VDOSs of layers 4 and 5.

### 3.3.5 Local heat flux by Irving–Kirkwood method

For the estimation of the local thermal properties in the heat exchange between two solid walls from an atomic perspective, a stable local heat flux distribution is established through data sampling for more than 50 ns by using the I–K method [95,96],

as shown in Fig. 3.11. The blue dashed lines represent the net heat flux of the system obtained from the energy balance of the two thermostats, the open circles are the local heat flux of each layer, and the black solid lines are guide for the eye. The component contributions of the heat transfer enhancement induced by the quasi-Casimir coupling are analyzed, as shown in Fig. 3.12. The local heat flux  $J_q$  of each solid layer is composed of four components, namely  $J_k$ ,  $J_p$ ,  $J_{is}$ , and  $J_{io}$  corresponding to the kinetic energy, potential energy, self-wall molecular interaction, and other wall molecular interaction, respectively.

**Table 3-1** Effects of  $D$  on the peak amplitudes and frequencies of atoms in the interfacial and inner layers at constant  $\Delta T = 20$  K.

$D$ (nm)	A2	B2	A3	B3	A4	B4
Peak amplitude (pm)						
0	1.909	1.244	1.722	1.246	1.471	1.468
0.196	1.646	1.583	1.570	1.559	2.775	2.526
0.784	1.733	1.302	1.335	1.235	1.734	1.693
Frequency $f$ (THz)						
0	4.041	3.699	3.790	3.701	3.736	3.727
0.196	4.578	4.452	4.207	4.207	3.277	3.257
0.784	4.483	4.359	4.017	3.949	3.180	3.149

When  $D = 0$ ,  $J_q$  is distributed uniformly and gets larger as  $\Delta T$  increases, as shown in Fig. 3.12(a)–(e).  $J_q$  satisfies the energy conservation law, which is equivalent to the net heat flux  $q$  obtained from the energy balance of the two thermostats. Clearly, the local heat flux components by I–K method  $J_{is}$  and  $J_{io}$  dominate the thermal energy transport

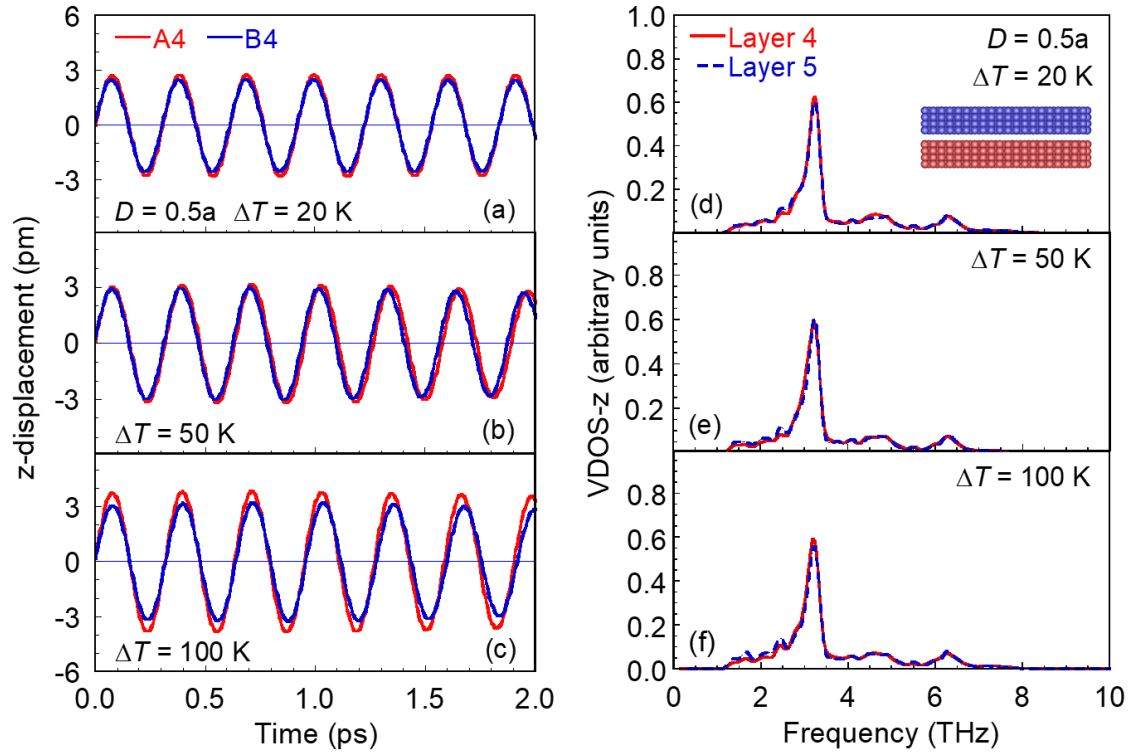


**Fig. 3.10** Effects of  $\Delta T$  on (a–c) the vibrational displacements of atoms A4 and B4 in the interfacial layers as well as (d–f) the VDOSs of layers 4 and 5.

in the solid, and  $J_k$  and  $J_p$  are negligible, as shown in Fig. 3.12(a)–(c). Here,  $J_{is}$  and  $J_{io}$  contribute equally at inner layers 4 and 5. When  $D = 0.5a$  (i.e., interfacial quasi-Casimir coupling), the apparent local heat flux increases singularly at the interfacial layers, whereas it is distributed uniformly at the inner layers, corresponding to  $q$ , as shown in Fig. 3.11(f)–(j). The apparent local heat flux at the interfacial layers enhances singularly, accompanied by considerable thermal resonance induced by quasi-Casimir coupling (see Fig. 3.9(b) and (f)). In Fig. 3.12(d)–(f), the singular increments of the apparent local heat flux at the interfacial layers are contributed to the increments of  $J_{io}$  (orange) and  $J_p$  (blue). Although  $J_{is}$  (green) is almost the same to the half of  $q$ ,  $J_{io}$  exceeds half of  $q$ , owing to the thermal resonance induced by the quasi-Casimir coupling. Additionally,

the interfacial vibration energy increases under the thermal resonance, resulting in the increment of  $J_p$  at the interface. In other words, the singular increments of the apparent local heat flux at the interfacial layers can be regarded as evidence of the quasi-Casimir coupling.

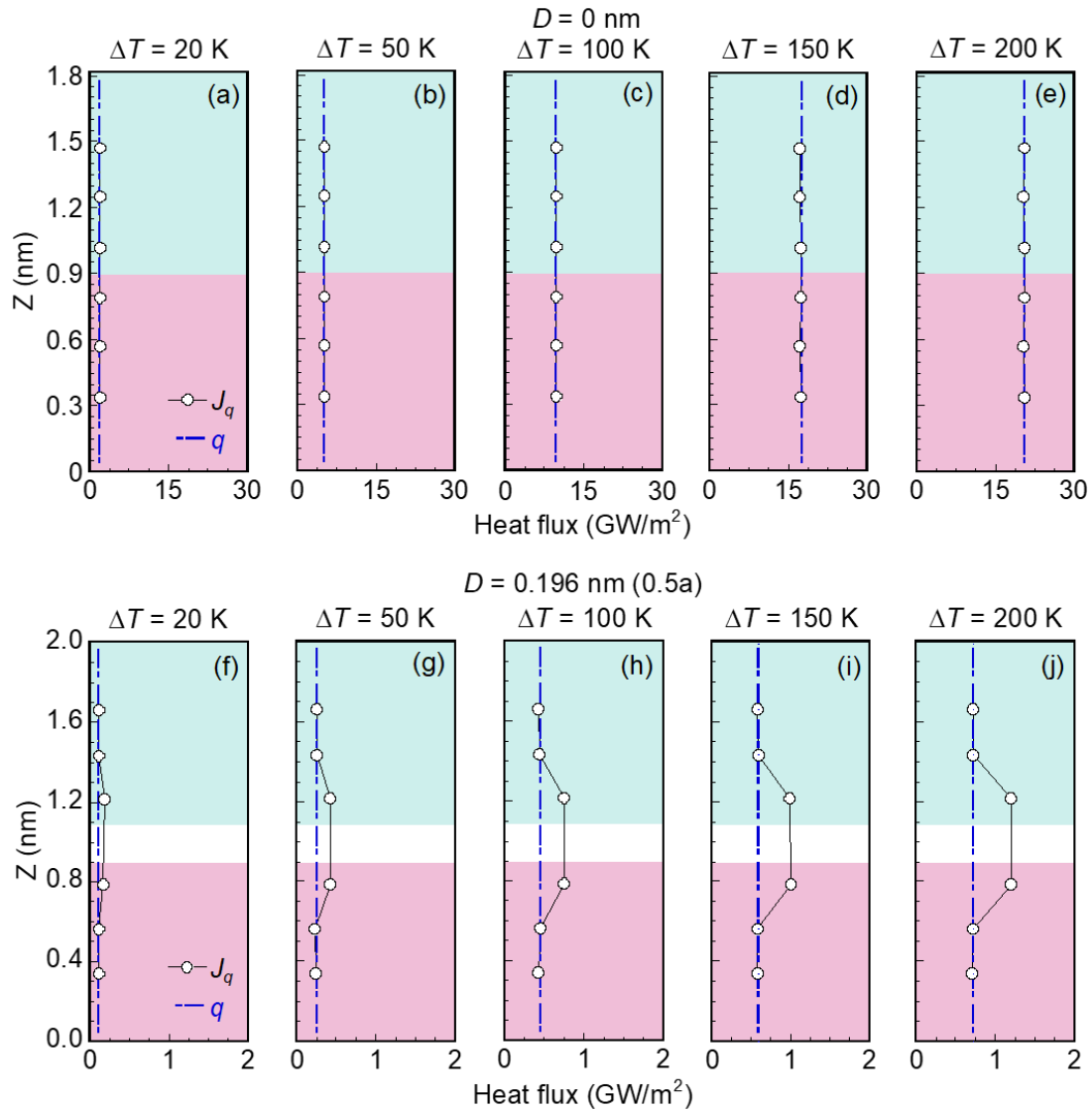


**Fig. 3.11** Effects of  $\Delta T$  on the local heat flux by I-K method of the interfacial and inner layers along the  $z$ -direction at (a-e)  $D = 0$  and (f-j)  $D = 0.5a$ .

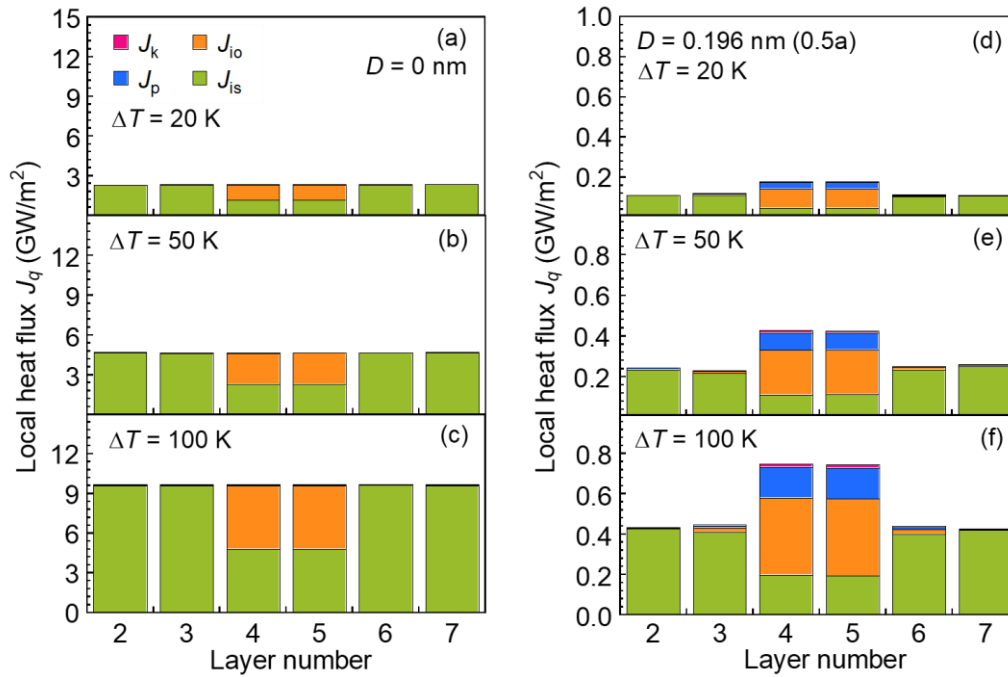


**Fig. 3.12** Effects of  $\Delta T$  on the contributions of the thermal energy components to the local heat flux by I–K method at the interfacial and inner layers at (a–c)  $D = 0$  and (d–f)  $D = 0.5a$ .

### 3.4 Summary

MD simulations were performed to investigate the phonon heat transfer across a vacuum gap induced by the quasi-Casimir force subjected to the Lennard–Jones atoms. We demonstrated that the heat exchange between two solid walls separated by a sub-nanometer vacuum gap increases exponentially as the gap distance decreases, following the energy conservation law. The heat transfer enhancement is caused by the acoustic phonon transport across a vacuum gap due to the strong thermal resonance induced by the quasi-Casimir coupling. This aspect is explained by the perfect overlap of the atomic vibrational displacements and VDOSs of the interfacial layers. Moreover, the apparent local heat flux, evaluated using the I–K method, increases singularly at the interfacial

layers, while that at the inner layers is consistent with the net heat flux. This finding provides evidence of the strong thermal resonance at the two interfacial layers, induced by quasi-Casimir coupling.

The phonon transport across a vacuum gap induced by quasi-Casimir coupling, is a phenomenon independent of electrostatic interaction, electron cloud overlap, surface phonon polaritons, and surface plasmon polaritons. This phenomenon is noticeably distinct from conventional heat conduction and thermal radiation, or the known NFRHT and Casimir heat transfer. The proposed quasi-Casimir coupling model of heat transfer provides fundamental insights into nanoscale energy transport between the regimes of NFRHT and heat conduction.



## Chapter 4

# 4 Quasi-Casimir coupling at the solid–liquid interface

## 4.1 Introduction

Phonon heat transfer through the thermal resonance induced by quasi-Casimir coupling has recently been verified in a vacuum nanogap without electromagnetic fields. However, whether phonons can be transmitted across a nanogap via liquid layers adsorbed on the superhydrophilic solid surfaces is still unknown. Here, we elucidate that the phonon transmission across a nanogap can be induced by quasi-Casimir coupling via liquid layers using classical non-equilibrium molecular dynamics simulation shown in Fig. 4.1. We show that the quasi-Casimir coupling exists between

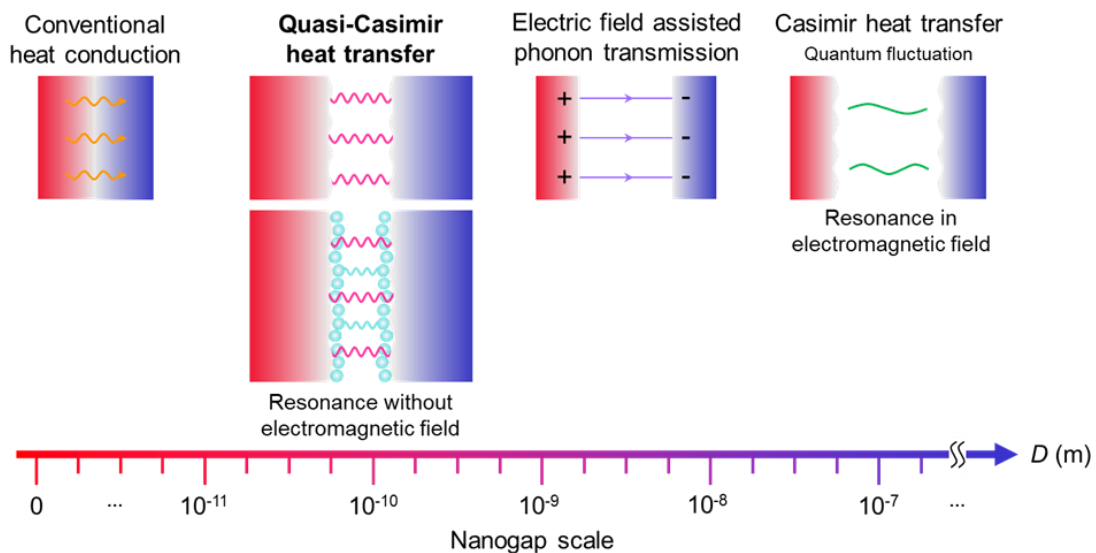


**Fig. 4.1** A schematic of quasi-Casimir heat transfer in a nanogap between two objects with the liquid layers in the transition regime from heat conduction to NFHT.

interfacial solid–liquid or liquid–liquid layers. The thermal resonance between two liquid layers can be induced by the quasi-Casimir coupling, agitating the co-occurrence of the thermal resonance between interfacial solid layers, while the liquid monolayer disturbs the resonance. On the occurrence of thermal resonance between liquid layers, more significant heat flux and thermal gap conductance can be obtained. Meanwhile, the interfacial liquid layer limits the acoustic phonon transmission in the interfacial solid layers. Consequently, our findings provide a fundamental understanding of quasi-Casimir heat transfer at the solid–liquid interface in a nanogap.

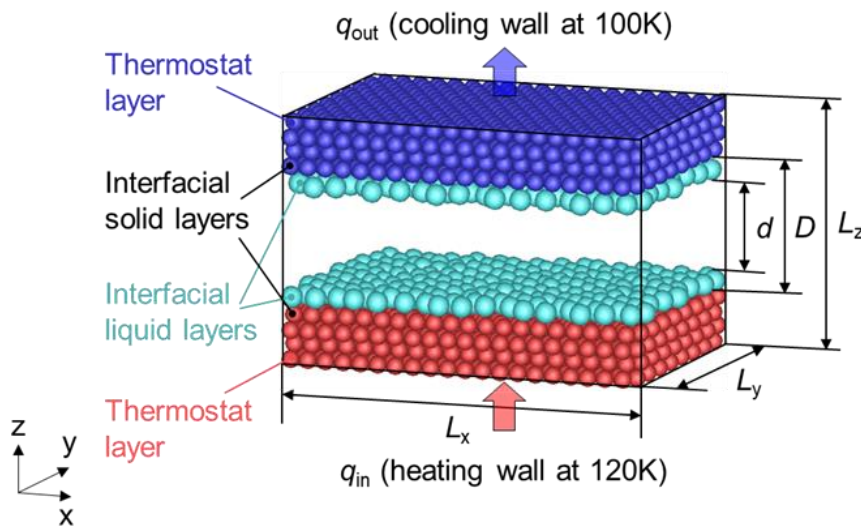


**Fig. 4.2** NEMD simulation system for thermal energy transport between two parallel solid walls separated by a nanogap including liquid layers.

## 4.2 Simulation method

The NEMD method [108,109] was utilized to simulate the phonon heat transfer across a nanogap, including the liquid layers between the heating wall (red) and the cooling wall (blue), as shown in Fig. 4.2. The dimensions of the computational domain were  $L_x = 5.552$  nm,  $L_y = 3.847$  nm, and  $L_z = 2.206$ – $4.165$  nm. The two parallel solid

walls were separated by a distance  $D$  of 0.392–2.352 nm ( $1a-6a$ , where  $a$  is the lattice constant of platinum 0.392 nm [106]). Each solid wall was composed of four layers of 1280 platinum atoms in face-centered cubic lattices, and its  $\langle 111 \rangle$  crystal plane faced the nanogap. The LJ liquid of 190–380 argon atoms was confined in the nanogap between the two solid walls, resulting in a smaller distance  $d$  of 0–2.057 nm than  $D$ . The maximum atom number for the liquid monolayer adsorbed on the solid surface was approximately 190, as shown in Fig. 4.3(a) and (c). The outermost layers of the heating and cooling walls were maintained at the constant temperature of 120 K and 100 K, respectively, using the velocity scaling method [105]. Periodic boundary conditions were utilized along the  $x$ - and  $y$ -directions.

The molecular interactions were modeled by the LJ potential using Eq. (2-1), where  $r_{ij}$  is the distance between two atoms  $i$  and  $j$ ,  $\sigma$  is the length parameter, and  $\varepsilon$  is the energy parameter. The parameters are  $\sigma = \sigma_1 = 3.405 \text{ \AA}$ ,  $\varepsilon = \varepsilon_1 = 1.67 \times 10^{-21} \text{ J}$  for the liquid–liquid interaction of argon, and  $\sigma = \sigma_s = 2.475 \text{ \AA}$ ,  $\varepsilon = \varepsilon_s = 8.35 \times 10^{-20} \text{ J}$  ( $\approx 50\varepsilon_1$ ) for the solid–solid interaction of platinum. For the solid–liquid interaction between argon and platinum,  $\sigma = \sigma_{sl} = (\sigma_1 + \sigma_s)/2$ , and  $\varepsilon = \varepsilon_{sl} = \sqrt{\varepsilon_1 \varepsilon_s}$  were utilized based on the Lorentz-Berthelot combining rule [87,88]. The contact angle of an argon droplet on a platinum surface has been found to be zero, representing a superhydrophilic solid surface [50,108].

All the simulations were carried out with a cut-off radius of 1.703 nm ( $5\sigma_1$ ) chosen for the spherically truncated and shifted potential. The velocity Verlet algorithm was utilized to integrate the equations of motion with a time step of 5 fs. The systems were initially equilibrated at 100 K after achieving a steady state for five ns. Subsequently, all

NEMD simulations were conducted to reach the steady state for 50 ns with constant heat flow ( $\Delta E = E_H - E_C \cong 0$ ) by monitoring the cumulative input and output energies  $E_H$  and  $E_C$  in the heating (120 K) and cooling (100 K) thermostats.

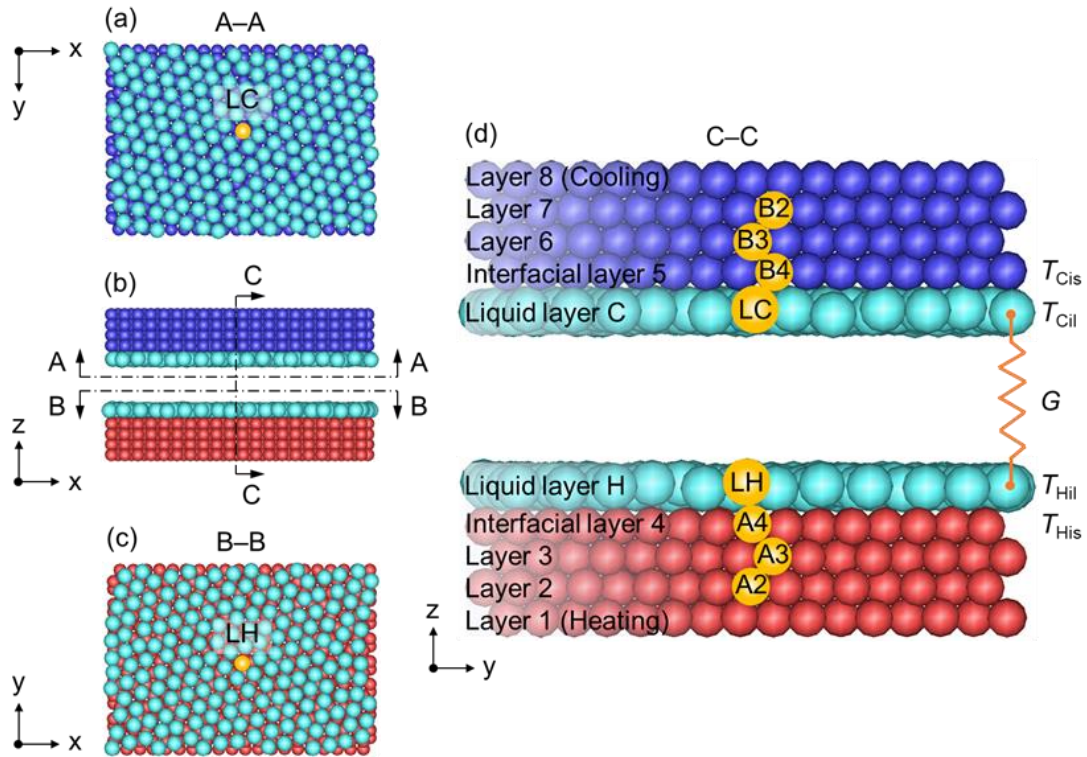


**Fig. 4.3** Atomic positions located at the center of interfacial and inner layers for analyzing the atomic vibrational characteristics: (a) atom LC at interfacial liquid layer C in the A–A directional view; (b) front view ( $x$ - $z$  plane); (c) atom LH at liquid layer H in the B–B directional view; (d) atoms A2, A3, A4 and B2, B3, B4 at the solid layers as well as atoms LH and LC at the liquid layers in the C–C directional enlarged view.

The data sampling was carried out for five ns to calculate the temperature of each solid and liquid layer in the steady state. The heat flux passing through the system was acquired using the mean value for the last 15 ns within a 50 ns time window. The heat

flux is calculated by Eq. (2-24). The thermal gap conductance between the interfacial layers can be calculated as  $G = q / (T_{\text{Hi}} - T_{\text{Ci}})$ , where  $T_{\text{Hi}}$  is the temperature of the heating interfacial solid layer ( $T_{\text{His}}$ ) or liquid layer ( $T_{\text{Hil}}$ ), and  $T_{\text{Ci}}$  is the temperature of the cooling interfacial solid layer ( $T_{\text{Cis}}$ ) or liquid layer ( $T_{\text{Cil}}$ ), as shown in Fig. 4.3(d).

To evaluate the atomic vibrational characteristics, the atomic vibrational displacements and frequencies were analyzed using the wave graph. The signal analysis of the atomic positions from the NEMD simulation data for 20,000 time steps was conducted to obtain the wave graphs [93]. The equilibrium position of the atoms in the  $z$ -direction is given by Eq. (2-22). The original vibrational displacements of atom  $i$  can be obtained from  $\Delta z_{i,t} = z_{i,t} - \bar{z}$ . Then, the Fourier transform of the original vibrational displacements was used to analyze the distribution of signal power in the frequency domain (power spectrum). To reduce the noise from the original vibrational displacements, the dominant frequency band was selected to conduct signal filtering. Therefore, the regular wave graphs can be plotted as the time history of the displacement for the specific atoms. The peak amplitude and frequency were determined from the wave graphs. The locations of the specific atoms for signal analysis are illustrated in Fig. 4.3, where A2, A3, and A4 are the center atoms in the solid layers of the heating wall, B2, B3, and B4 are the center atoms in the solid layers of the cooling wall, LH and LC are the center atoms in the interfacial liquid layers neighboring to A4 and B4, respectively.

The VDOS [110–112] of the interfacial layer was calculated by Eq. (2-23) using the velocities of all the atoms at the interfacial solid and liquid layers by the Fourier transform of the velocity autocorrelation function during a period of 20,000 time steps.

## 4.3 Results and discussion

### 4.3.1 Quasi-Casimir coupling via a liquid monolayer

We have demonstrated that the thermal resonance was induced by the quasi-Casimir coupling across a vacuum gap between the two interfacial solid layers [113]. In this section, we discuss the atomic vibrational characteristics when two solid walls are separated by a nanogap with a liquid monolayer.

To begin with, a firmly connected solid–liquid–solid system is compared with a system of a vacuum gap between two solids at  $D = 1a$ . The left side of Fig. 4.4 shows the snapshots of the simulated systems. For the solid–liquid–solid system, as shown in Fig. 4.4(a) and (b), the peak amplitudes of the atom LC/LH in the liquid monolayer (green) are larger than those of the solid atoms, while the interfacial solid atoms A4 (red) and B4 (blue) are in harmony with the liquid atom LC/LH. Compared with the inner solid atoms (A2, A3, B2, B3), the interfacial solid atom vibrates with a larger amplitude but a lower frequency. This phenomenon is more significant in the case of the liquid monolayer than that of a vacuum gap (without liquid monolayer), as shown in Fig. 4.4(c) and (d).

As demonstrated in our previous study [113], owing to the presence of two interfaces separated by a vacuum gap, the quasi-Casimir coupling stimulated the interfacial undulations and thus induced the thermal resonance through molecular interaction (see Fig. 4.5(c)). Similarly, in Fig. 4.5(a), the thermal resonance can be confirmed by the perfect overlapped vibrational displacements of the atoms A4 and B4. However, this thermal resonance is induced by quasi-Casimir coupling between two interfacial solid

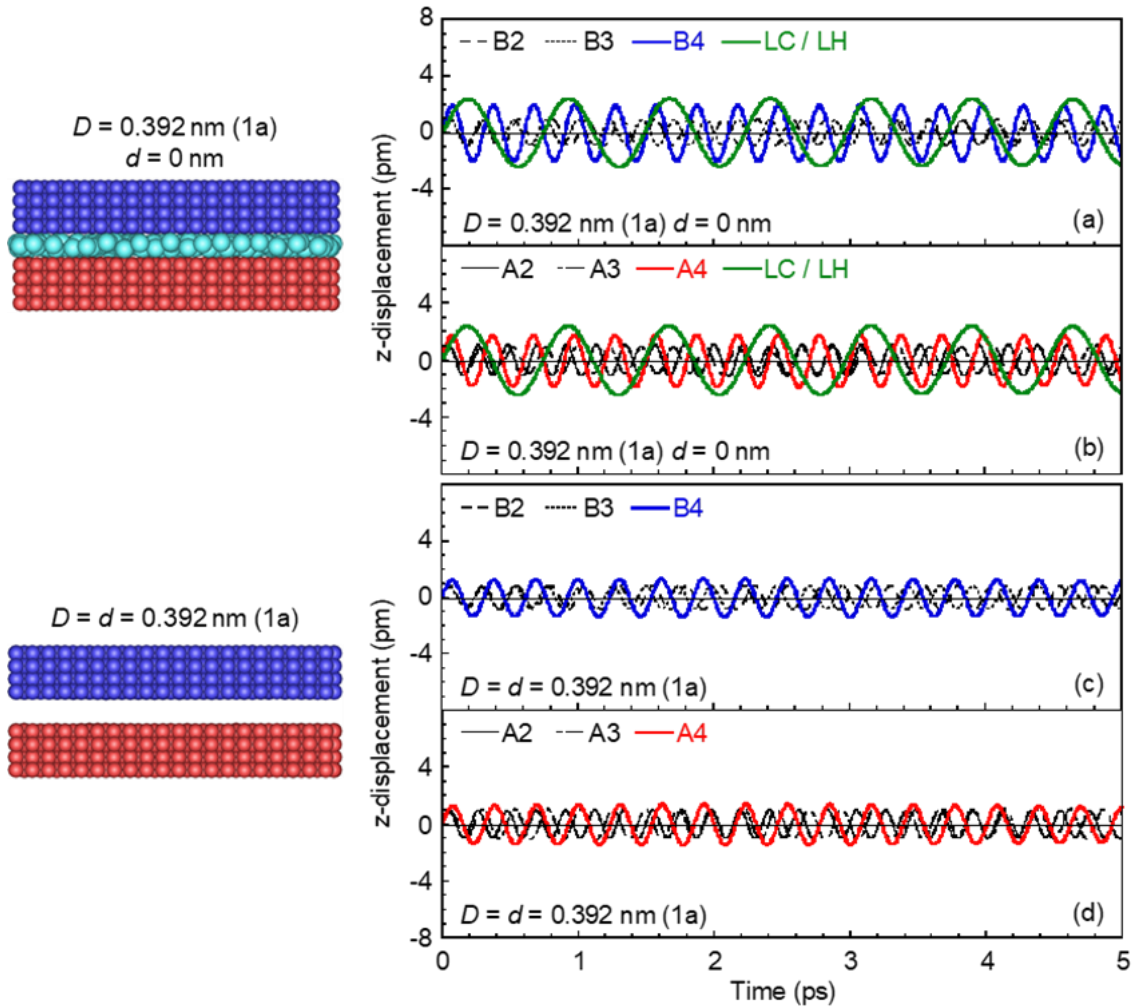


**Fig. 4.4** Atomic vibrational displacements of specific atoms: (a) at solid layers in cooling wall and liquid monolayer, (b) at solid layers in the heating wall and liquid monolayer, for a firmly connected solid–liquid–solid system; (c) at solid layers in cooling wall, (d) at solid layers in heating wall, for a solid–vacuum–solid system.

layers across a liquid monolayer instead of the vacuum gap. Accordingly, the VDOSs of solid layer 4 match entirely those of layer 5 in Fig. 4.5(b) and (d), where the peaks correspond to the vibrational frequencies of A4, B4 (see Table 4-1). Nevertheless, the VDOSs of the liquid monolayer (layer C/H) mismatch with those of the solid layers, and the vibrational frequency of LC/LH is much more minor than that of the solid atoms. Although the thermal resonance occurs in the simulation systems with liquid monolayer,

the interfacial solid layers with the liquid monolayer are subjected to a stronger surface undulation. That is, the liquid monolayer enhances the thermal resonance between the interfacial solid layers.

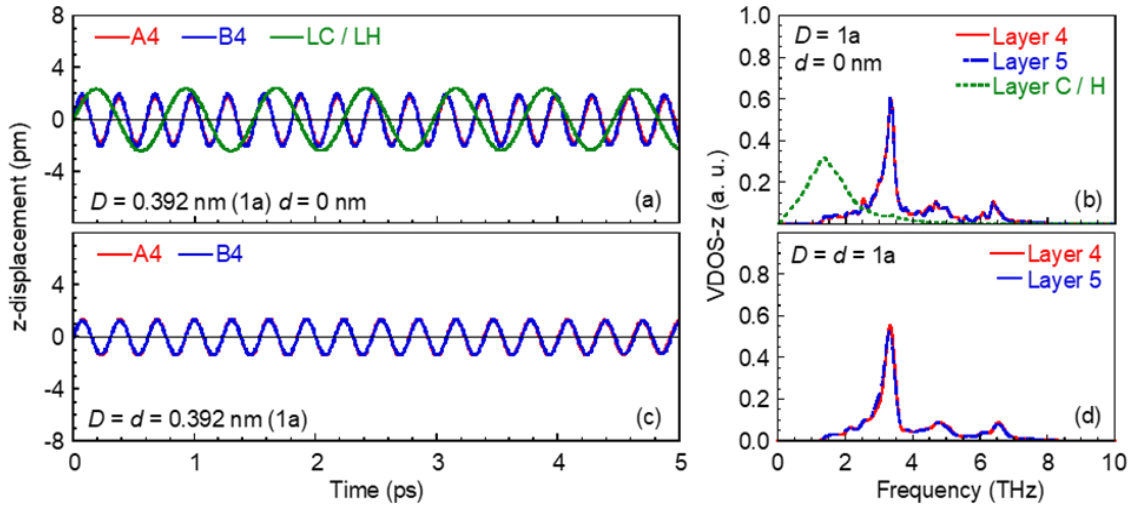


**Fig. 4.5** Atomic vibrational displacement of specific atoms and VDOSs at interfacial solid layers and liquid monolayer for (a–b) a firmly connected solid–liquid–solid system, (c–d) a solid–vacuum–solid system.

To verify the quasi-Casimir coupling between the interfacial solid and liquid layers separated by a nanogap, we analyzed the atomic vibrational characteristics when the liquid monolayer was adsorbed on the cooling solid surface. The snapshots of the simulated systems with different gap distance  $D$  are shown on the left side of Fig. 4.6. In the case of  $D = 1.5a$ , the interfacial liquid atom LC vibrates with a higher peak amplitude than the solid atoms, as shown in Fig. 4.6(a) and (b). This difference diminishes at  $D = 2a$  and almost disappears at  $D = 6a$ , owing to the weaker molecular interactions between the interfacial solid and liquid atoms (see Fig. 4.6(c)–(f)). Meanwhile, the peak amplitudes of the interfacial solid atoms A4 and B4 are larger than those of the inner solid atoms at  $D = 1.5a$  and  $2a$ , but nearly identical at  $D = 6a$ .

**Table 4-1** The peak amplitudes and frequencies of atoms in the inner solid layers as well as interfacial solid and liquid layers.

$D/d$ (nm)	Ar atoms	A2	A3	A4	B2	B3	B4	LH	LC
Peak amplitude (pm)									
0.392 / 0.392	0	1.006	1.077	1.380	0.844	0.812	1.363	–	–
0.392 / 0.000	190	1.100	0.955	2.031	0.944	0.890	1.930	2.474	–
0.588 / 0.293	190 (C)	0.925	0.992	1.562	0.932	1.064	1.267	–	3.152
0.588 / 0.293	190 (H)	1.093	0.924	1.756	1.093	0.956	1.738	3.802	–
0.588 / 0.000	380	1.012	0.909	1.818	0.996	0.975	1.806	3.122	3.033
0.784 / 0.489	190 (C)	1.071	0.921	1.328	1.006	0.969	1.015	–	2.032
0.784 / 0.489	190 (H)	1.065	0.943	1.555	1.058	1.031	1.356	2.050	–
0.784 / 0.193	380	0.985	0.959	1.576	0.938	0.986	1.595	4.249	4.077
2.352 / 2.057	190 (C)	0.977	1.015	1.061	0.961	0.970	1.085	–	1.185
2.352 / 2.057	190 (H)	0.983	1.067	1.070	0.955	0.963	1.032	1.250	–
2.352 / 1.761	380	0.971	0.923	1.070	1.066	1.029	0.932	1.285	1.131
Frequency $f$ (THz)									
0.392 / 0.392	0	4.673	4.157	3.242	3.982	4.159	3.236	–	–
0.392 / 0.000	190	4.607	4.247	3.325	3.976	4.236	3.322	1.345	–
0.588 / 0.293	190 (C)	4.547	4.171	3.310	4.061	3.832	3.474	–	2.358
0.588 / 0.293	190 (H)	4.597	4.236	3.525	4.375	4.160	3.394	2.424	–
0.588 / 0.000	380	4.618	4.304	3.261	4.270	4.136	3.250	2.768	2.769
0.784 / 0.489	190 (C)	4.376	4.246	3.302	4.077	4.281	3.462	–	2.313
0.784 / 0.489	190 (H)	4.388	4.284	3.539	4.248	4.154	3.348	2.384	–
0.784 / 0.193	380	4.587	4.254	3.515	4.037	4.221	3.510	2.668	2.668
2.352 / 2.057	190 (C)	4.379	4.173	3.178	4.002	4.280	3.442	–	2.163
2.352 / 2.057	190 (H)	4.323	4.058	3.215	4.233	4.149	3.149	2.168	–
2.352 / 1.761	380	4.134	4.220	3.165	4.079	4.181	2.765	2.374	2.125

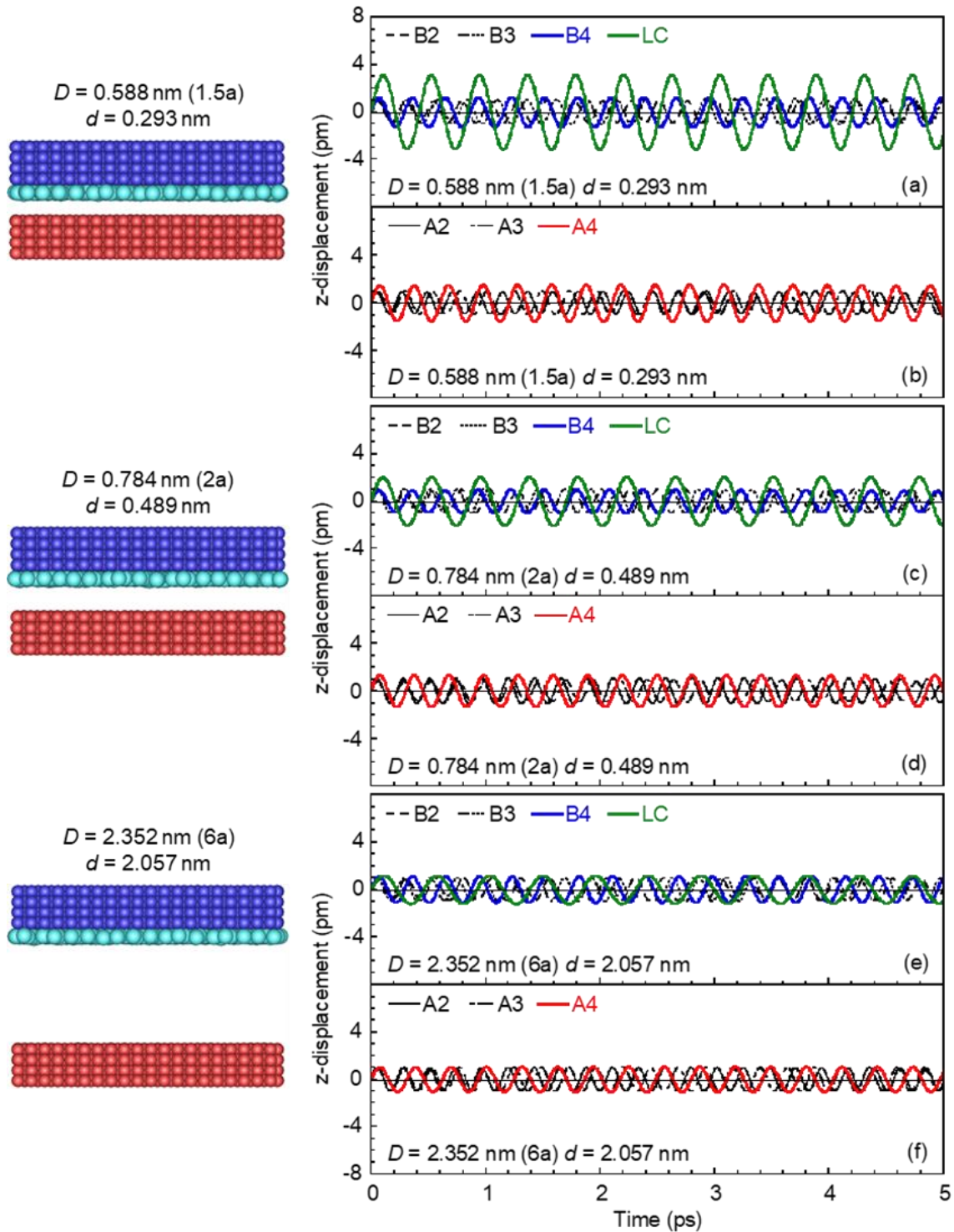


**Fig. 4.6** Atomic vibrational displacements of specific atoms in the heating and cooling walls as well as the liquid monolayer adsorbed on the cooling solid surface at varying gap distance: (a–b)  $D = 1.5a$ ; (c–d)  $D = 2a$ ; (e–f)  $D = 6a$ .

From Fig. 4.7(a), (c), and (e), the liquid monolayer disturbs the thermal resonance on account of the completely different atomic vibrational displacements. The vibrational frequency of the atom LC is lower than that of the solid atoms as listed in Table 1. Therefore, the apparent phonon mismatches were observed in the VDOSs of solid layers 4, 5, and liquid layer C, as depicted in Fig. 4.7(b), (d), and (f). Although the peaks of the VDOSs for the interfacial solid layers separated by the vacuum gap overlap well (see in Fig. 4.5(d)), those for the cooling interfacial solid layer 5 decreased significantly due to the presence of the adsorbed liquid layer. That is, the liquid layer limits the peak of the VDOS at the cooling interfacial solid layer and thus suppresses the acoustic phonon transmission. Nevertheless, these results verify the existence of the quasi-Casimir coupling between the liquid monolayer adsorbed on the cooling surface and the interfacial solid layer.

The snapshots of the simulated systems for the liquid monolayer adsorbed on the heating solid surface are shown on the left side of Fig. 4.8. The vibrational displacements of the interfacial solid and liquid atoms increase with a decrease of the gap distance, owing to the enhanced quasi-Casimir coupling. Interestingly, the peak amplitudes and vibrational frequencies of the interfacial solid and liquid atoms in the cases of  $D = 1.5a$  are larger than those shown in Fig. 4.6. Several liquid atoms are excluded from the adsorbed liquid layer on the heating solid surface in the case of  $D = 1.5a$ . Unlike the interfacial solid layers 4 and 5 separated by the vacuum gap (see Fig. 4.5(d)), the peaks of the VDOSs for the heating interfacial solid layer 4 decreased significantly due to the presence of the adsorbed liquid layer, as shown in Fig. 4.9. The liquid layer limits the peak of the VDOS at the adjacent interfacial solid layer and thus reduces the acoustic phonon transmission through the adjacent solid layer.

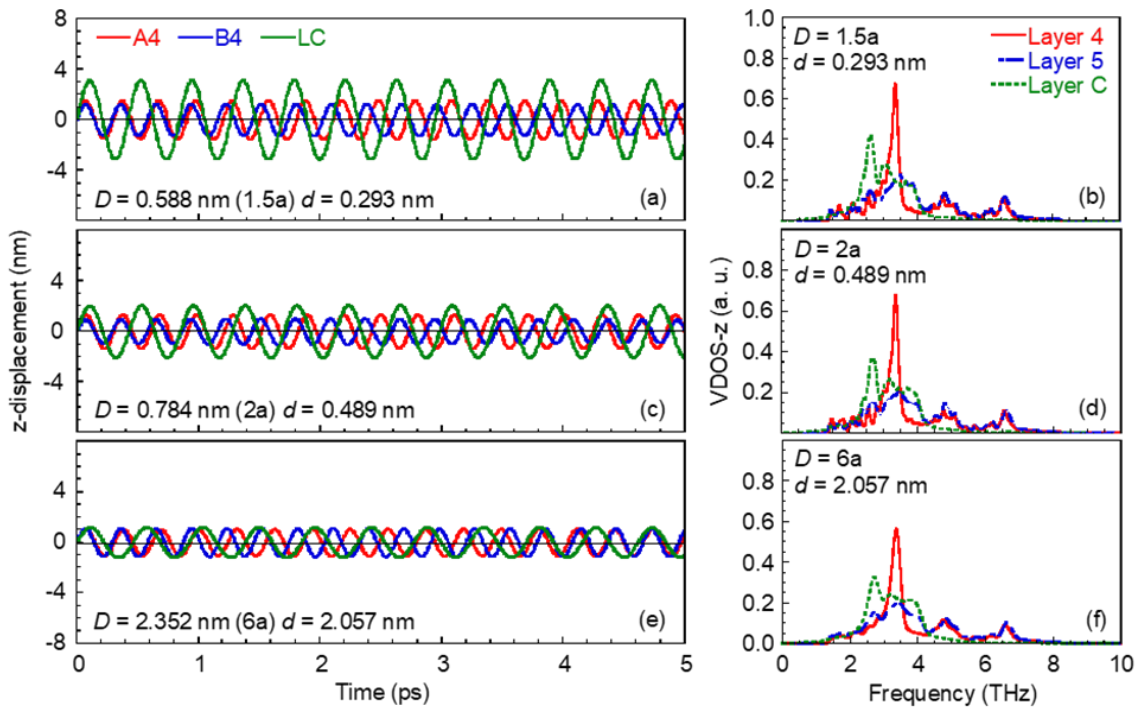


**Fig. 4.7** Atomic vibrational displacement of specific atoms and VDOSs at interfacial solid layers and liquid monolayer adsorbed on the cooling solid surface at (a–b)  $D = 1.5a$ , (c–d)  $D = 2a$  and (e–f)  $D = 6a$ .

### 4.3.2 Thermal resonance between two liquid layers

The effect of the liquid monolayer on the phonon transmission has been clarified in Section 4.3.1, subsequently, those of two liquid layers adsorbed on both the heating and cooling solid surfaces are discussed hereafter. The snapshots of the simulated systems including two liquid layers are shown on the left side of Fig. 4.10. In the case of  $D = 2a$ , the peak amplitudes of interfacial liquid atoms LH (yellow) and LC (green) are significantly larger than those of the solid atoms, while this difference decreases at  $D = 1.5a$  and becomes insignificant at  $D = 6a$ , as shown in Fig. 4.10(a)–(f). In accordance with Section 4.3.1, the undulations of the interfacial liquid layers are strengthened as a result of the increased molecular interactions with decreasing  $D$ . Thus, the quasi-

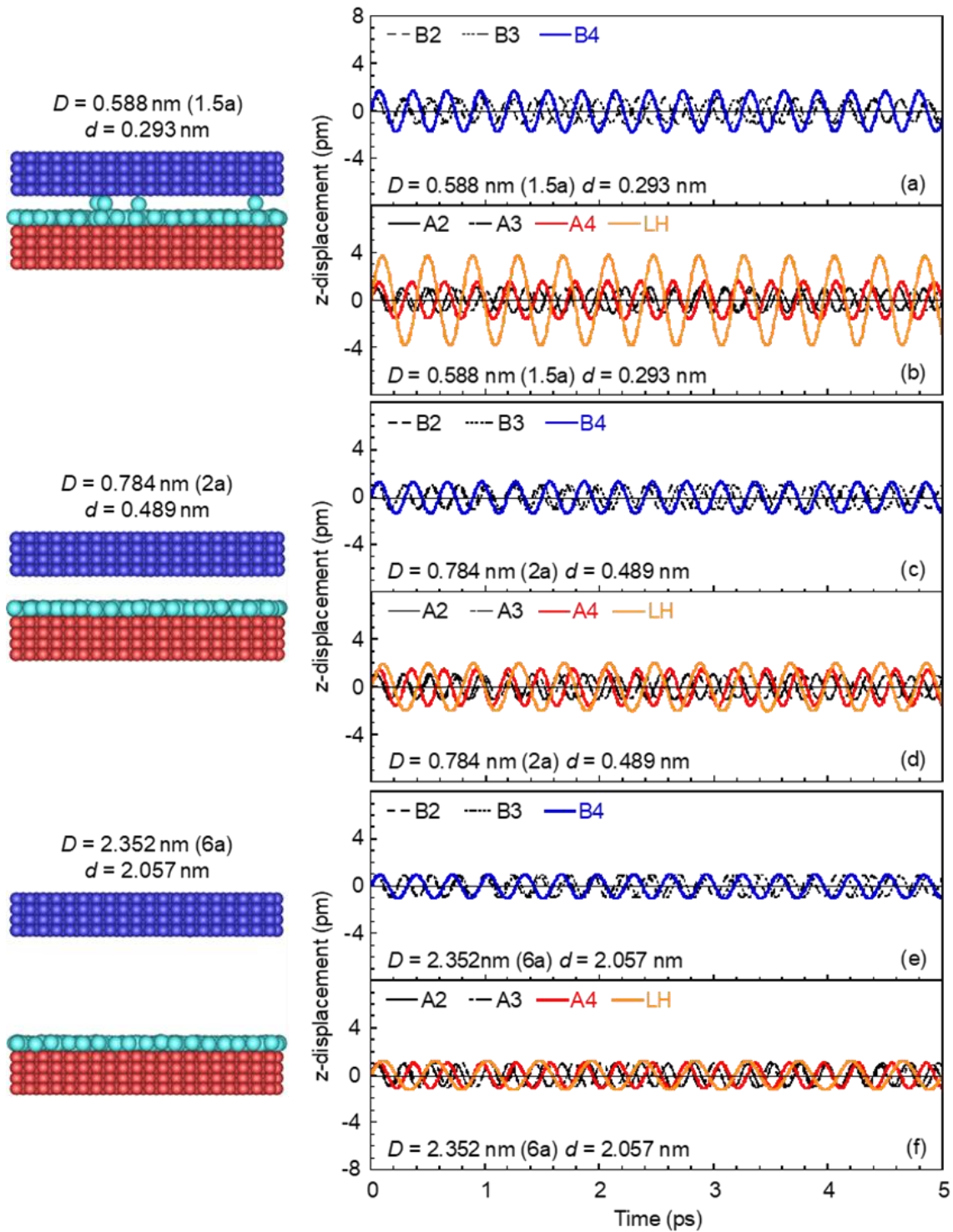


**Fig. 4.8** Atomic vibrational displacements of specific atoms in the heating and cooling walls as well as the liquid monolayer adsorbed on the heating solid surface at varying gap distance: (a–b)  $D = 1.5a$ ; (c–d)  $D = 2a$ ; (e–f)  $D = 6a$ .

Casimir coupling can exist between two interfacial liquid layers H and C. Meanwhile, the interfacial solid atoms A4 (red) and B4 (blue) vibrate with a larger peak amplitude at  $D = 1.5a$  and  $2a$  than  $D = 6a$ . Additionally, in the cases of  $D = 1.5a$  and  $2a$ , the thermal resonance occurs between the interfacial solid layers 4 and 5 as well as liquid layers H and C, respectively, which is evidenced by the perfect overlapped vibrational displacements of the atoms A4–B4 and LH–LC (see Fig. 4.11(a) and (c)). Similar to the interfacial solid layers, the VDOSs of liquid layers completely match each other, even though the adsorbed liquid layers limit the peaks of the VDOSs in the interfacial solid layers and suppress the acoustic phonon transmission (see Fig. 4.11(b) and (d)). However, the thermal resonance disappears in the case of  $D = 6a$  shown in Fig. 4.11(e) and (f). It is worth noting that the thermal resonance between two liquid layers agitates the co-occurrence of the thermal resonance between interfacial solid layers. These results demonstrate that the quasi-Casimir coupling at the solid–liquid interface can induce the thermal resonance between liquid layers in a nanogap.

Similar results can be found in Fig. 4.10 and 4.11, where  $\varepsilon_{sl} / \varepsilon_1 \approx 5.6$  and  $3.5$  at  $D = 2a$ . Coinciding with the case of  $\varepsilon_{sl} / \varepsilon_1 \approx 7$ , the quasi-Casimir coupling is verified between two interfacial liquid layers H and C (Fig. 4.12(a)–(f)). In Fig. 4.13(a)–(f), the thermal resonance between the interfacial solid layers 4 and 5 occurs as well as that between liquid layers H and C, while decreasing  $\varepsilon_{sl}$  results in an increase in the atomic vibrational displacements. That is, when the stable liquid layers are adsorbed on the solid surfaces,  $\varepsilon_{sl}$  is not the key factor for the quasi-Casimir heat transfer and thermal resonance via adsorbed liquid layers.

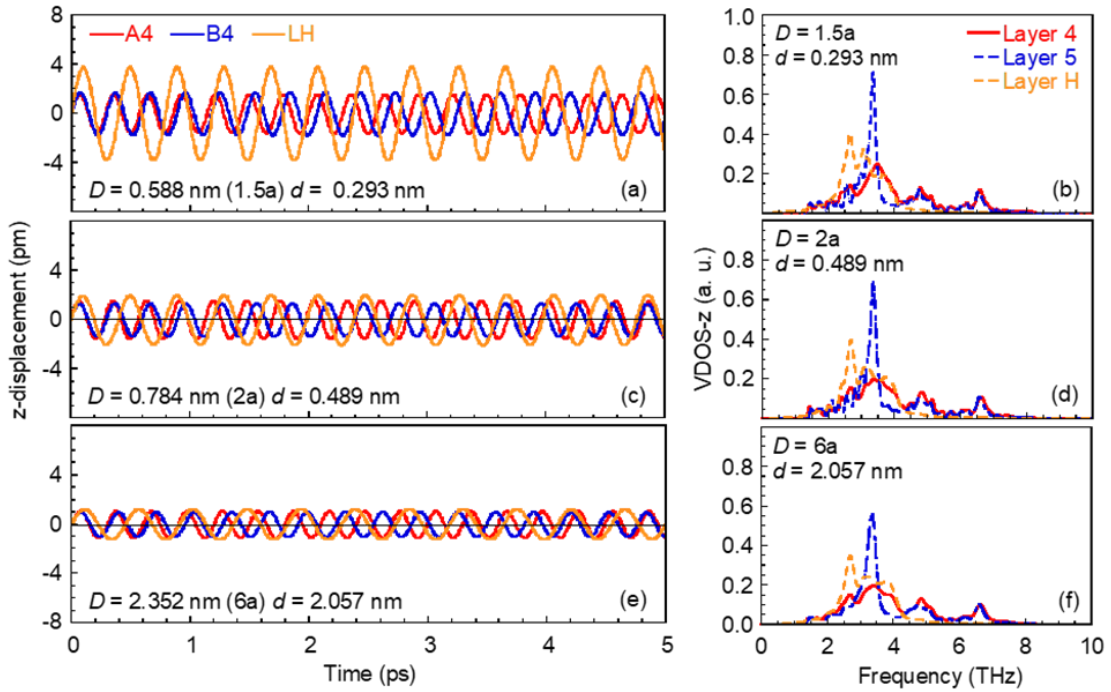


**Fig. 4.9** Atomic vibrational displacement of specific atoms and VDOSs at interfacial solid layers and liquid monolayer adsorbed on the heating solid surface at (a–b)  $D = 1.5a$ , (c–d)  $D = 2a$  and (e–f)  $D = 6a$ .

### 4.3.3 Thermal energy transport across a nanogap

In Section 3.3.3, it is found that the net heat flux and thermal gap conductance are dominated by the gap distance between two solid walls. Here, the thermal energy transport across a nanogap via liquid layers is discussed. For the reason that both heating and cooling surfaces are subjected to the quasi-Casimir coupling induced by molecular interactions, the thermal energy transports from the heating object to the cooling one with the surface undulations. Accordingly, the net heat flux  $q$  of the system and thermal gap conductance  $G$  between the interfacial layers (see Fig. 4.3(d)) were obtained by performing the data sampling over 15 ns to investigate the gap-dependent thermal energy transport.

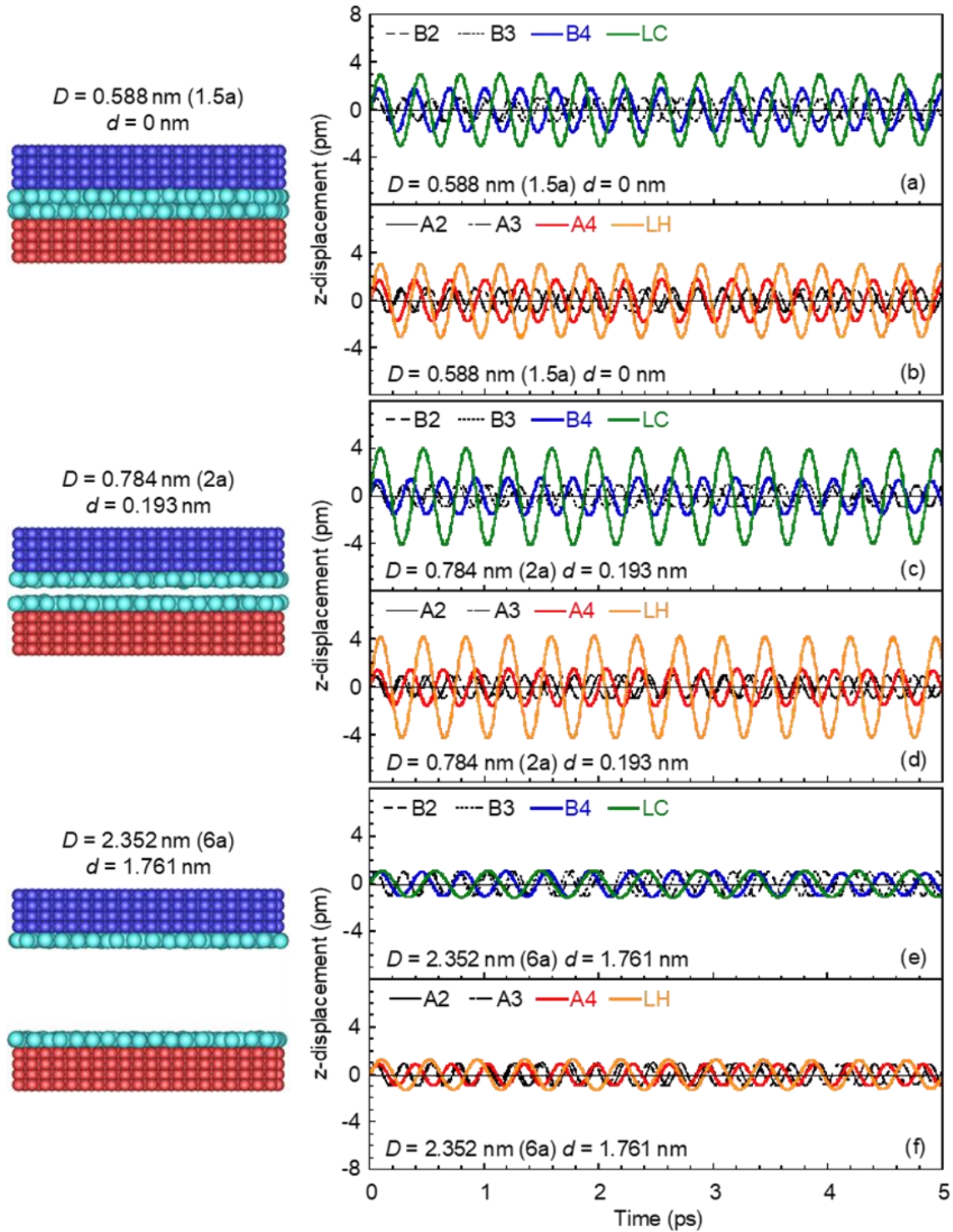


**Fig. 4.10** Atomic vibrational displacements of specific atoms in the heating and cooling walls as well as the liquid layers adsorbed on the cooling and heating solid surfaces at varying gap distance: (a–b)  $D = 1.5a$ ; (c–d)  $D = 2a$ ; (e–f)  $D = 6a$ .

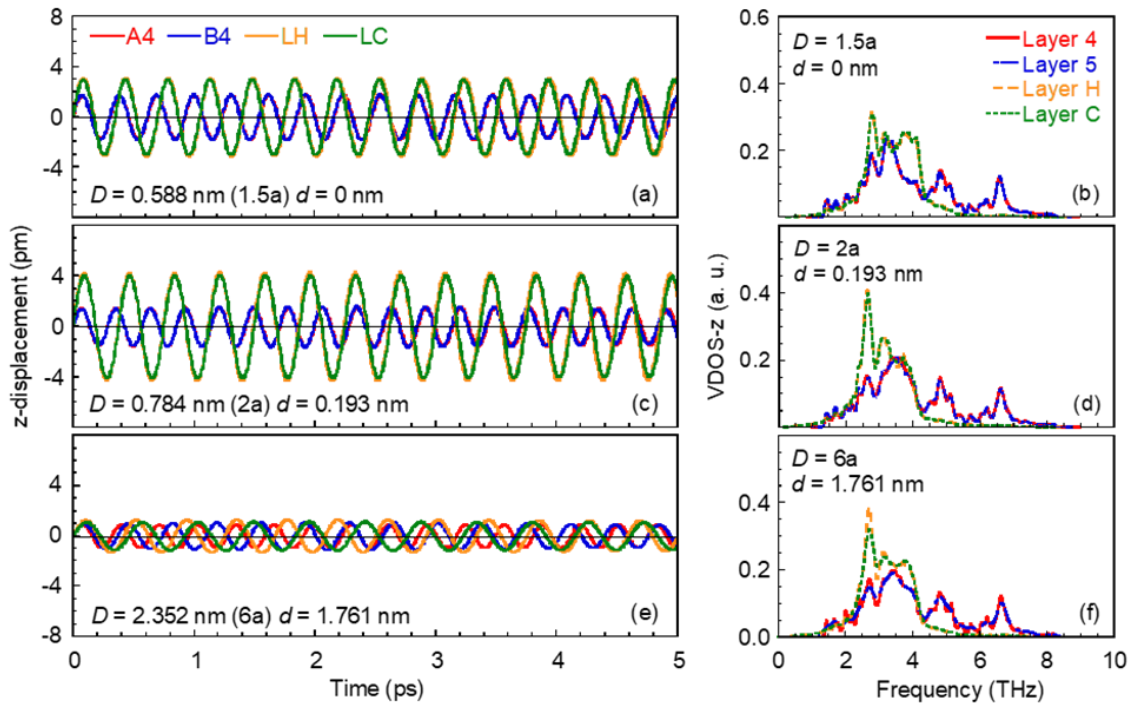


**Fig. 4.11** Atomic vibrational displacements of specific atoms and VDOSs at interfacial solid layers and liquid monolayer adsorbed on the cooling and heating solid surfaces: (a–b)  $D = 1.5a$ , (c–d)  $D = 2a$  and (e–f)  $D = 6a$ .

Due to the strengthened molecular interactions between the interfacial solid and liquid atoms,  $q$  and  $G$  exponentially increase with decreasing  $D$  (see Fig. 4.14(a), (b), and Table 2). Larger  $q$  and  $G$  are acquired in the cases of the liquid layers adsorbed onto the solid surfaces, compared with the cases of the vacuum gap (circle dots). Surprisingly, one to three orders of magnitude enhancement in  $q$  and  $G$  (red dots) is achieved under the thermal resonance between the two liquid layers. Additionally,  $q$  and  $G$  for the liquid monolayer adsorbed on the heating solid surface (blue dots) are larger than those on the cooling solid surface (green dots) at  $D = 0.588$  nm. The root reason for this deviation attributes to the stronger vibration of the interfacial atoms at the heating surface than that at the cooling surface.

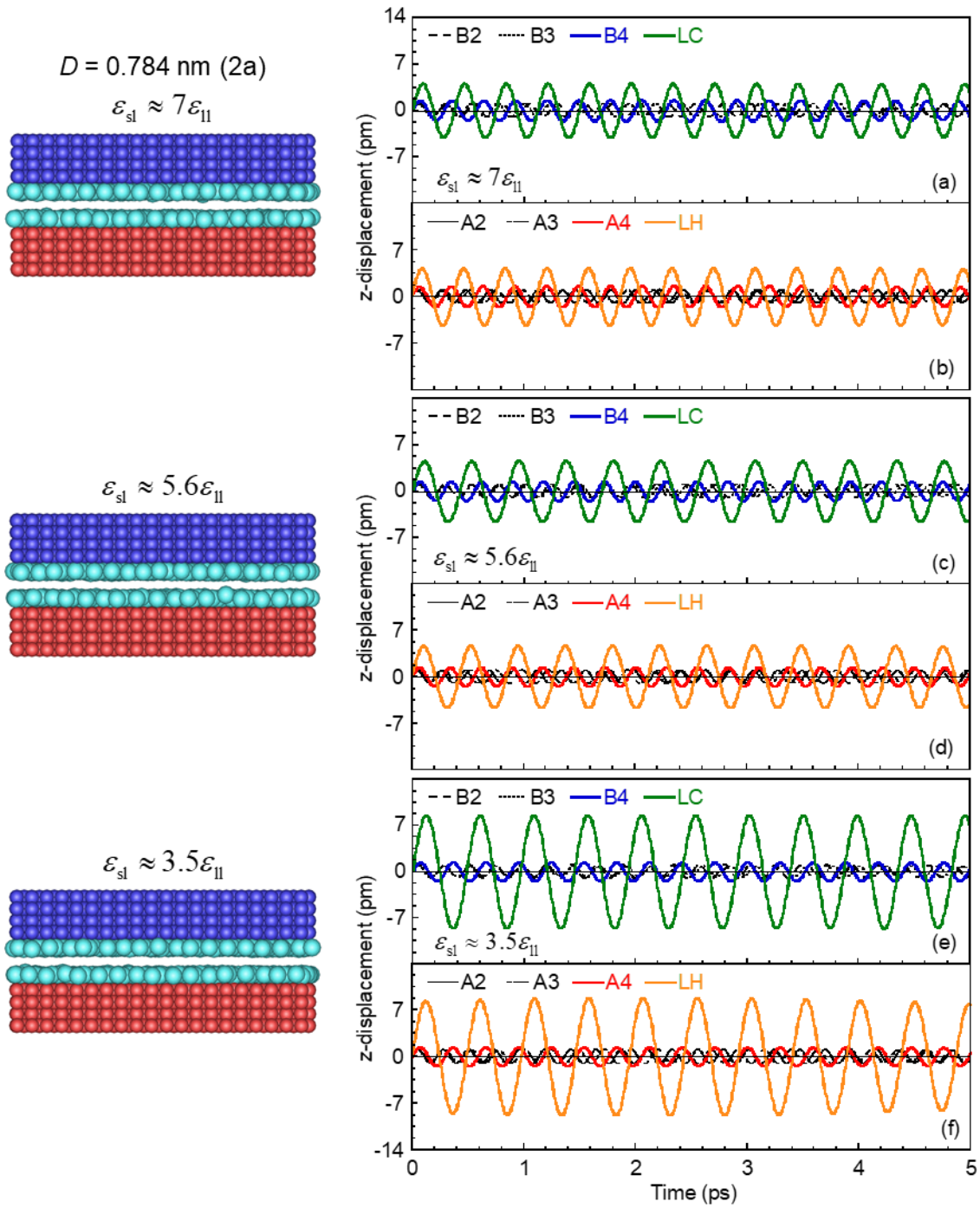


**Fig. 4.12.** Atomic vibrational displacements of specific atoms in the heating and cooling walls as well as the liquid layers adsorbed on the cooling and heating solid surfaces at varying energy parameters  $\epsilon_{sl}$ : (a–b)  $\epsilon_{sl} \approx 7\epsilon_{II}$ ; (c–d)  $\epsilon_{sl} \approx 5.6\epsilon_{II}$ ; (e–f)  $\epsilon_{sl} \approx 3.5\epsilon_{II}$ .

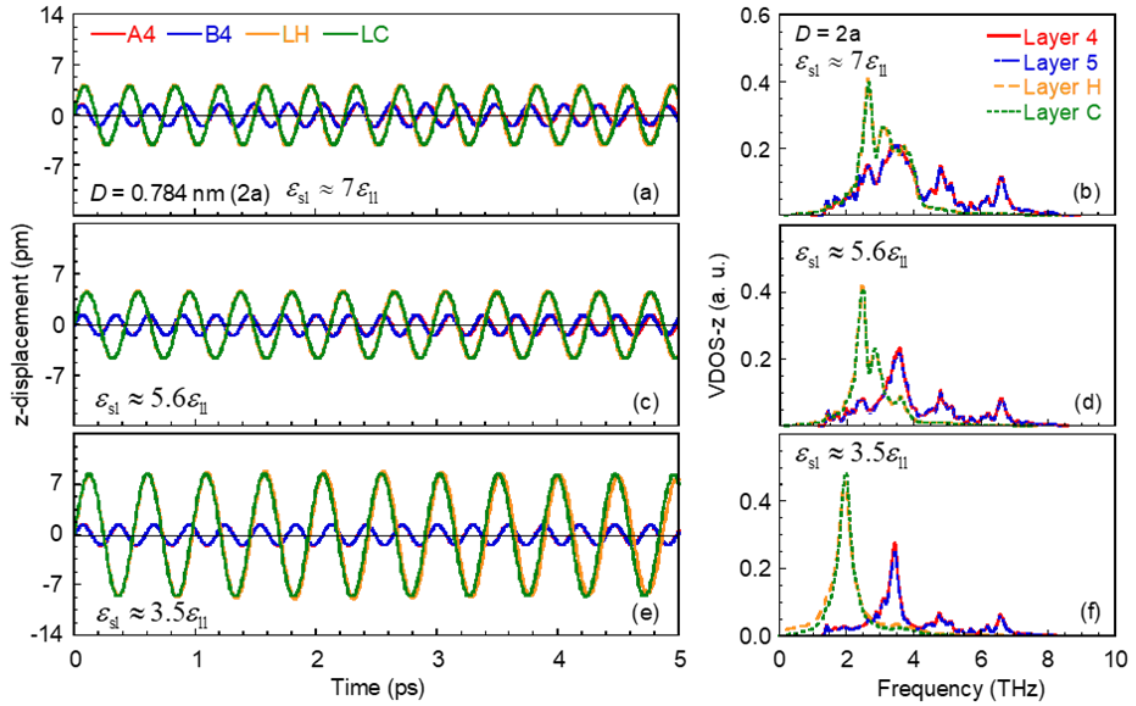


**Fig. 4.13.** Atomic vibrational displacements of specific atoms and VDOSs at interfacial solid layers and liquid monolayers adsorbed on the cooling and heating solid surfaces at varying energy parameters  $\varepsilon_{sl}$ : (a–b)  $\varepsilon_{sl} \approx 7\varepsilon_{||}$ ; (c–d)  $\varepsilon_{sl} \approx 5.6\varepsilon_{||}$ ; (e–f)  $\varepsilon_{sl} \approx 3.5\varepsilon_{||}$ .

For reference, on the basis of an alternative gap distance  $d$  between the interfacial solid–liquid or liquid–liquid layers for the  $x$ -axis,  $q$  and  $G$  are lower than those in the cases of the vacuum gap shown in Fig. 4.14(c) and (d). This is because that the quasi-Casimir coupling between the interfacial liquid–liquid or solid–liquid layers is weaker than that between the interfacial solid–solid layers at the same  $d$ . It is notable that  $q$  and  $G$  with two liquid layers (red dots at  $D = 0.588$  nm,  $d = 0$ ) are greater than those with liquid monolayer (green/blue dots at  $D = 0.392$  nm,  $d = 0$ ). Due to the simultaneous existence of quasi-Casimir coupling and thermal resonance in nanoscale heat conduction,  $q$  and  $G$  at  $d = 0$  raise considerably compared with those at  $d > 0$ . Nevertheless, for a given  $D$  in molecular scale, the liquid layer still can contribute to the

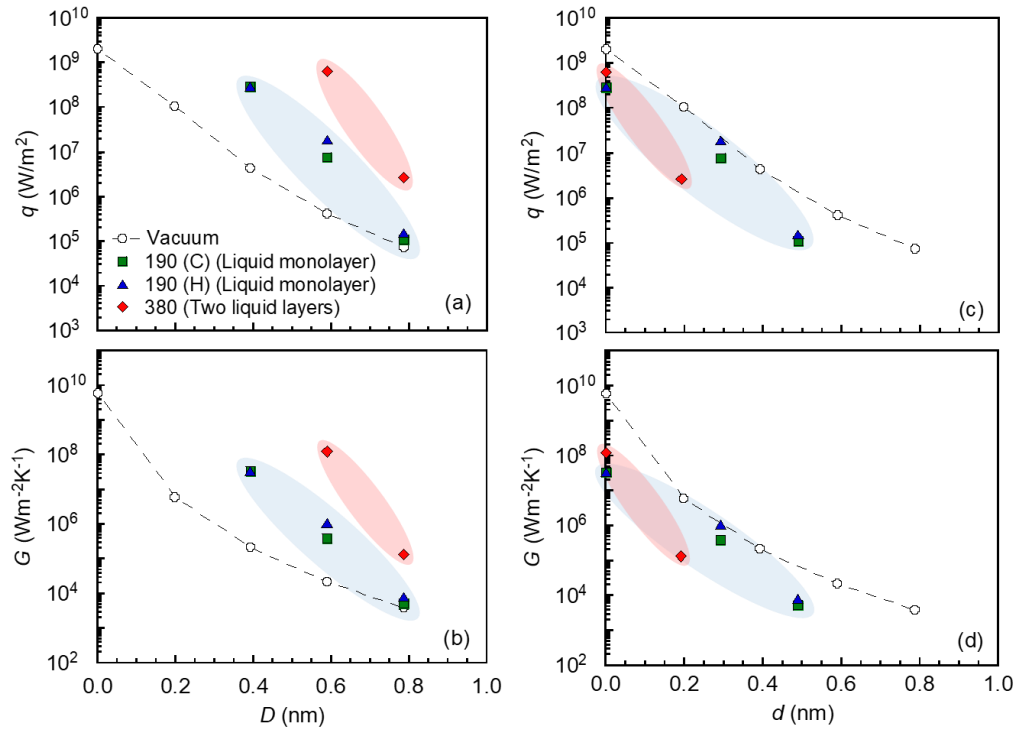


**Fig. 4.14** Heat flux and thermal gap conductance versus gap distance (a–b)  $D$  between the interfacial solid layers, (c–d)  $d$  between the interfacial solid–liquid or liquid–liquid layers. The dashed line is a guide for the eyes.

**Table 4-2** Simulation results obtained at different gap distances in the steady non-equilibrium systems.

$D / d$ (nm)	Ar atoms	$T_{\text{His}}$ (K)	$T_{\text{Cis}}$ (K)	$T_{\text{Hil}}$ (K)	$T_{\text{Cil}}$ (K)	$\Delta T$ (K)	$q$ ( $\times 10^6$ Wm $^{-2}$ )	$G$ ( $\times 10^3$ Wm $^{-2}$ K $^{-1}$ )
0.392 / 0.000	190	118.73	101.36	108.74	108.74	8.69	295.66	34042.55
0.588 / 0.293	190 (C)	119.85	100.24	–	100.88	18.97	7.69	405.31
0.588 / 0.293	190 (H)	119.86	100.72	117.86	–	17.14	18.64	1087.76
0.588 / 0.000	380	117.97	102.27	111.62	106.39	5.23	655.48	125331.51
0.784 / 0.489	190 (C)	120.10	100.14	–	99.13	20.97	0.11	5.36
0.784 / 0.489	190 (H)	120.21	100.25	118.90	–	18.65	0.15	8.16
0.784 / 0.193	380	120.20	100.03	120.75	100.36	20.39	2.73	133.85

thermal energy transport in the absence of thermal resonance and thus enhances NFHT. Consequently, the quasi-Casimir coupling at the solid–liquid interface is verified as an additional channel for phonon heat transfer across a nanogap.

#### **4.4 Summary**

NEMD simulations were carried out to study the phonon heat transfer across a nanogap induced by the quasi-Casimir coupling between interfacial layers of solid–liquid or liquid–liquid. The liquid monolayer adsorbed over the cooling/heating surface, and two liquid layers adsorbed over both the cooling and heating surfaces were focused on to clarify the effect of the liquid layer on phonon transmission across a nanogap. The following conclusions have been drawn.

- (1) The quasi-Casimir coupling exists at the solid–liquid interface, not only between solid–liquid but also between liquid–liquid layers.
- (2) The thermal resonance between the two liquid layers can be induced by the quasi-Casimir coupling, agitating the co-occurrence of the thermal resonance between the interfacial solid layers. In contrast, a liquid monolayer disturbs the thermal resonance between the interfacial solid layers.
- (3) Owing to the thermal resonance between two liquid layers, heat flux and thermal conductance across the nanogap increase one to three orders of magnitude compared with those across the vacuum gap. Meanwhile, the liquid layer limits the acoustic phonon transmission in the interfacial solid layers.

- (4) The heat flux and thermal gap conductance exponentially increase with decreasing gap distance with the aid of liquid layer, evidencing the significance of quasi-Casimir heat transfer in NFHT.

In the present study, we verified that the acoustic phonons could be transmitted across a nanogap via liquid layer, attributing to the quasi-Casimir coupling and thermal resonance under strong molecular interaction between liquid and solid. However, there is no guarantee for the same phenomena under the weak molecular interaction between liquid and solid. Therefore, future work is expected to explore the effects of the weak molecular interaction (e.g., surface hydrophobicity) on the quasi-Casimir phonon heat transfer across a nanogap. In particular, understanding the quasi-Casimir heat transfer mechanism shall open a new window to optimize NFHT for nanoscale thermal management.

## **Chapter 5**

# **5 Weak solid–liquid interaction enhances phonon heat transfer**

### **5.1 Introduction**

Phonon heat transfer across a nanogap via the liquid layers adsorbed on the superhydrophilic surfaces has been verified, attributed to the quasi-Casimir coupling and thermal resonance under strong molecular interaction between liquid and solid. However, it is unclear whether phonons can transmit across a nanogap under weak solid–liquid molecular interactions. To address this issue, in this study, we varied the solid–liquid interaction by the potential energy factors to investigate quasi-Casimir coupling across a nanogap including the non-adsorbed liquid atoms using non-equilibrium molecular dynamics simulations. Unlike the adsorbed solid-like liquid layers, the liquid atoms move randomly and frequently collide with other liquid and interfacial solid atoms. We demonstrate that the weak solid–liquid interaction can enhance thermal energy transportation across a nanogap between two planar solid walls. The mechanism of thermal energy transport across a nanogap with liquid includes both the contribution of solid atomic vibrations and liquid atomic collisions. Phonon mismatch between the interfacial solid layers decreases with the aid of liquid atomic collisions, resulting in the maximum heat flux and thermal conductance despite the gap distance between two solid walls.

## 5.2 Simulation method

The NEMD simulations were conducted to study the thermal energy transportation across a nanogap, including the liquid between the heating wall (red) and the cooling wall (blue), as shown in Fig. 5.1. The dimensions of the computational domain were  $L_x = 5.552$  nm,  $L_y = 3.847$  nm, and  $L_z = 2.206$ – $2.991$  nm. The two parallel solid walls were separated by a distance  $D$  of  $0.392$ – $1.176$  nm ( $1a$ – $3a$ , where  $a$  is the lattice constant of platinum  $0.392$  nm [106]). Each solid wall was composed of four layers of 1280 platinum atoms in face-centered cubic lattices, and its  $\langle 111 \rangle$  crystal plane faced the nanogap. The LJ liquid of 190 argon atoms was confined in the nanogap between the two solid walls. Periodic boundary conditions were utilized along the  $x$ - and  $y$ -directions.

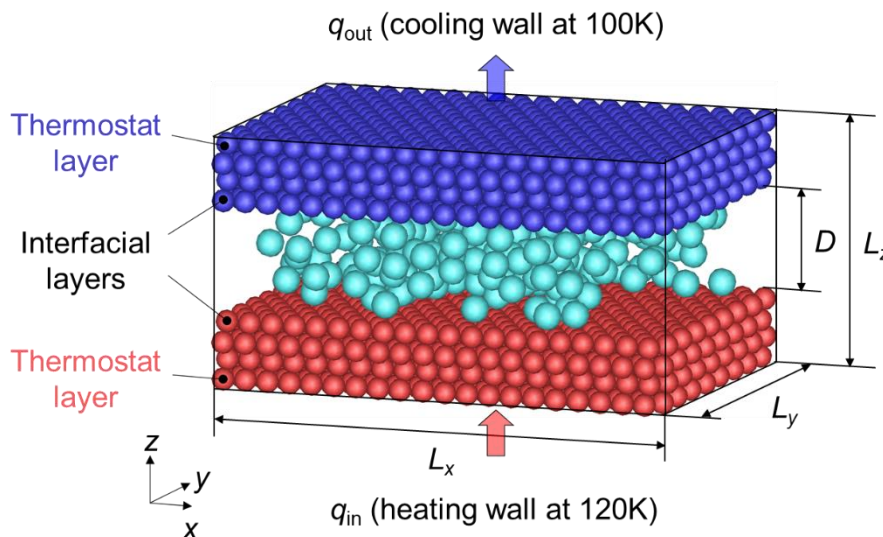


**Fig. 5.1.** NEMD simulation system for thermal energy transport between two parallel solid walls separated by a nanogap including liquid.

The solid–solid and liquid–liquid interactions are expressed by the LJ potential using Eq. (2-1), where  $r_{ij}$  is the distance between two atoms  $i$  and  $j$ ,  $\sigma$  is the length parameter,

and  $\varepsilon$  is the energy parameter. The parameters are  $\sigma = \sigma_1 = 3.405 \text{ \AA}$  ,  
 $\varepsilon = \varepsilon_1 = 1.67 \times 10^{-21} \text{ J}$  for the liquid–liquid interaction of argon, and  $\sigma = \sigma_s = 2.475 \text{ \AA}$  ,  
 $\varepsilon = \varepsilon_s = 8.35 \times 10^{-20} \text{ J}$  ( $\approx 50\varepsilon_1$ ) for the solid–solid interaction of platinum.

The solid–liquid interaction between argon and platinum is modeled by the modified LJ potential using Eq. (2-2), where  $\sigma = \sigma_{sl} = (\sigma_1 + \sigma_s)/2$  , and  $\varepsilon = \varepsilon_{sl} = \alpha \sqrt{\varepsilon_1 \varepsilon_s}$  were utilized based on the Lorentz-Berthelot combining rule [87,114]. Here,  $\alpha$  is the potential energy factor indicating the strength of hydrophilic interaction and  $\beta$  is the potential energy factor indicating the attraction for hydrophobic interaction. The modified form of the LJ potential is a combination of the potential models used by Din and Michaelides [89] as well as by Barrat and Bocquet [90]. In this study, we set  $\alpha = 1, 0.5, 0.2,$  and  $0.14$  as well as  $\beta = 1.0, 0.5,$  and  $0.1$  to obtain the 5 cases with varying strength of solid–liquid molecular interaction, as shown in Fig. 5.2.

All the simulations were carried out with a cut-off radius of  $1.703 \text{ nm}$  ( $5\sigma_1$ ) chosen for the spherically truncated and shifted potential. The velocity Verlet algorithm was utilized to integrate the equations of motion with a time step of five fs. The systems were initially equilibrated at  $100 \text{ K}$  after achieving a steady state for five ns. Subsequently, the outermost layers (thermostats) of the heating and cooling walls were maintained at the constant temperature of  $120 \text{ K}$  and  $100 \text{ K}$ , respectively, using the velocity scaling method. Nevertheless, the other solid and liquid layers were free from thermostats in NEMD simulations. The temperature difference was imposed on the heating and cooling walls to induce a heat flow passing through the system. All NEMD simulations were conducted to reach the steady state for  $50 \text{ ns}$  with constant heat flow

( $\Delta E = E_H - E_C \cong 0$ ) by monitoring the cumulative input and output energies  $E_H$  and  $E_C$  in the heating and cooling thermostats.

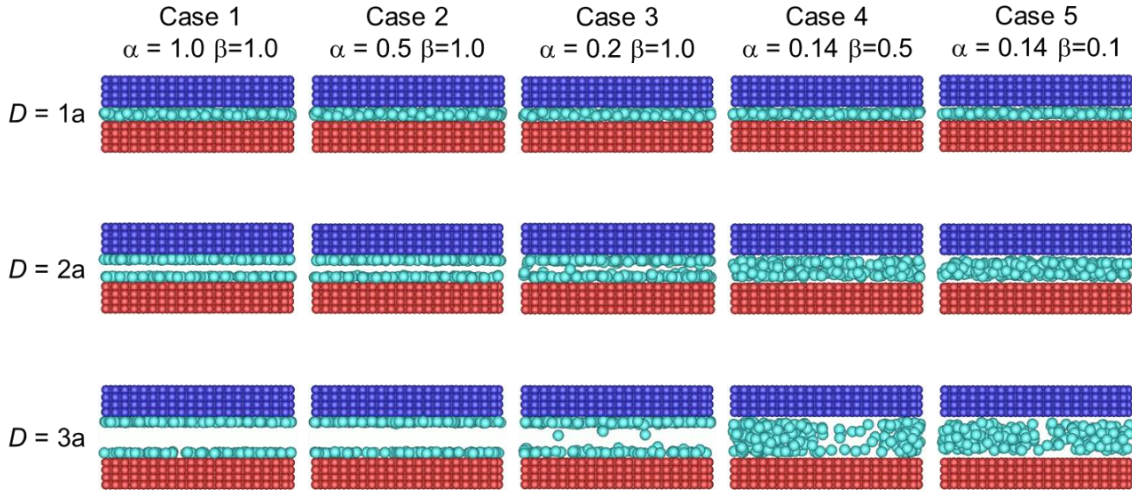


**Fig. 5.2.** All simulation systems at  $D = 1-3a$  under varying solid–liquid interactions.

The data sampling was carried out for five ns to calculate the temperature of each solid and liquid layer using Eq. (2-21) in the steady state. The heat flux passing through the system was acquired by Eq. (2-24) using the mean value for the last 15 ns within a 50 ns time window. The thermal gap conductance between the interfacial layers can be calculated as  $G = q/(T_{Hi} - T_{Ci})$ , where  $T_{Hi}$  is the temperature of the heating interfacial solid layer, and  $T_{Ci}$  is the temperature of the cooling interfacial solid layer ( $T_{Cis}$ ), as shown in Fig. 5.3.

The atomic vibrational displacements and frequencies were analyzed using the wave graph. The signal analysis of the atomic positions from the NEMD simulation data for 20,000 time steps was conducted to obtain the wave graphs [46]. The equilibrium position of the atoms in the  $z$ -direction is given by (2-22). The original vibrational

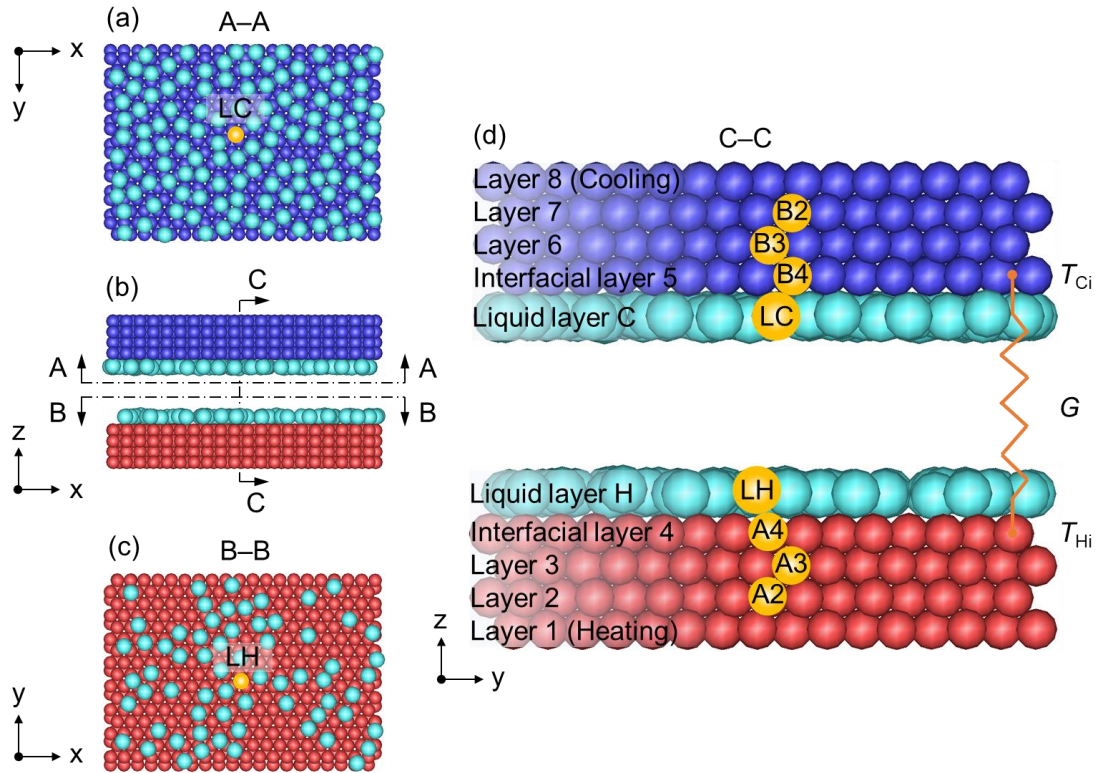


**Fig. 5.3** Atomic positions located at the center of interfacial and inner layers for analyzing the atomic vibrational characteristics: (a) atom LC at interfacial liquid layer C in the A–A directional view; (b) front view ( $x$ - $z$  plane); (c) atom LH at liquid layer H in the B–B directional view; (d) atoms A2, A3, A4 and B2, B3, B4 at the solid layers as well as atoms LH and LC at the liquid layers in the C–C directional enlarged view.

displacements of atom  $i$  can be obtained from  $\Delta z_{i,t} = z_{i,t} - \bar{z}$ . Then, the Fourier transform of the original vibrational displacements was used to analyze the distribution of signal power in the frequency domain (power spectrum). To reduce the noise from the original vibrational displacements, the dominant frequency band was selected to conduct signal filtering. Therefore, the regular wave graphs can be plotted as the time history of the displacement for the specific atoms. The peak amplitude and frequency were determined from the wave graphs. The locations of the specific atoms for signal analysis are illustrated in Fig. 5.3, where A2, A3, and A4 are the center atoms in the

solid layers of the heating wall, B2, B3, and B4 are the center atoms in the solid layers of the cooling wall, LH and LC are the center atoms in the interfacial liquid layers neighboring to A4 and B4, respectively.

The VDOS of the interfacial layer was calculated by Eq. (2-23) using the velocities of all the atoms at the interfacial solid and liquid layers by the Fourier transform of the velocity autocorrelation function during a period of 20,000 time steps.

## 5.3 Results and discussion

### 5.3.1 Density profiles

The density profile is an important parameter that can help evaluate the effect of different solid–liquid interactions on the liquid argon. Fig. 5.4 shows the density profiles of liquid argon in nanogap along  $z$ -direction for all simulation cases. When  $D = 1a$ , only one peak value in the density of liquid atoms due to one liquid monolayer confined in nanogap is much higher than that of liquid density for  $D = 2a$  and  $3a$  under the varying solid–liquid interaction. However, when  $D = 2a$ , there are two peaks in the density of liquid atoms near heating and cooling solid surfaces. The density of the liquid layer neighboring the cooling solid surface is larger than that of the heating solid surface owing to the stronger solid–liquid interaction in cases 1–3. This difference disappears in cases 4 and 5 with weak solid–liquid interaction. Similarly, for  $D = 3a$ , the density of the liquid layer adsorbed on the cooling solid surface is more significant than that on the heating solid surface in cases 1–3, while the density distribution becomes uniform in cases 4 and 5 due to the much weaker solid–liquid interaction.

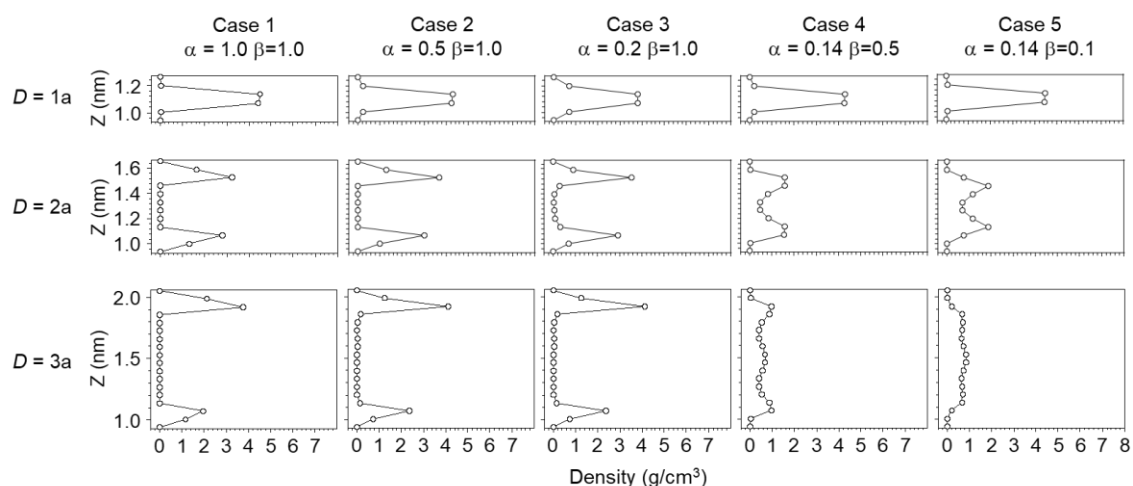


**Fig. 5.4** Density profiles of liquid confined between two solid walls in  $z$ -direction for all simulation cases. The solid line is a guide for the eye.

### 5.3.2 Potential and kinetic energy

To observe the effects of solid–liquid interaction on thermal energy transport across a nanogap, we calculated the potential and kinetic energy of liquid atoms as shown in Fig. 5.5 and 5.6. The potential energy can reflect the interaction energy and degree of coupling between atoms at the nanoscale. Investigating the potential energy distribution can reveal the variation of the solid–liquid coupling strength.

In the previous studies, the thermal energy transport will be enhanced by increasing the strength of solid–liquid coupling. Thus, we calculate the potential energy of liquid to observe the heat transfer across a nanogap, as shown in Fig. 5.5. The red and blue regions are the high and low potential energy regions, respectively. There is only one significantly high potential energy region in case 1 at  $D = 1a$  because the liquid layer is confined firmly with the strong solid–liquid molecular interaction in the nanogap between two solid walls. Nevertheless, the potential energy of the liquid layer decreases with the weakening of the solid–liquid molecular interaction from cases 1 to 5. In the

case of  $D = 2a$ , the potential energy of the liquid is concentrated on the two sides near solid surfaces when two liquid layers are adsorbed onto the solid surfaces in cases 1–3, while it is uniformly distributed in the nanogap in cases 4–5. The yellow points exist in the two layers of potential energy near solid surfaces owing to the more extended time residence of argon atoms. Additionally, we can observe similar potential energy results in the case of  $D = 3a$ .

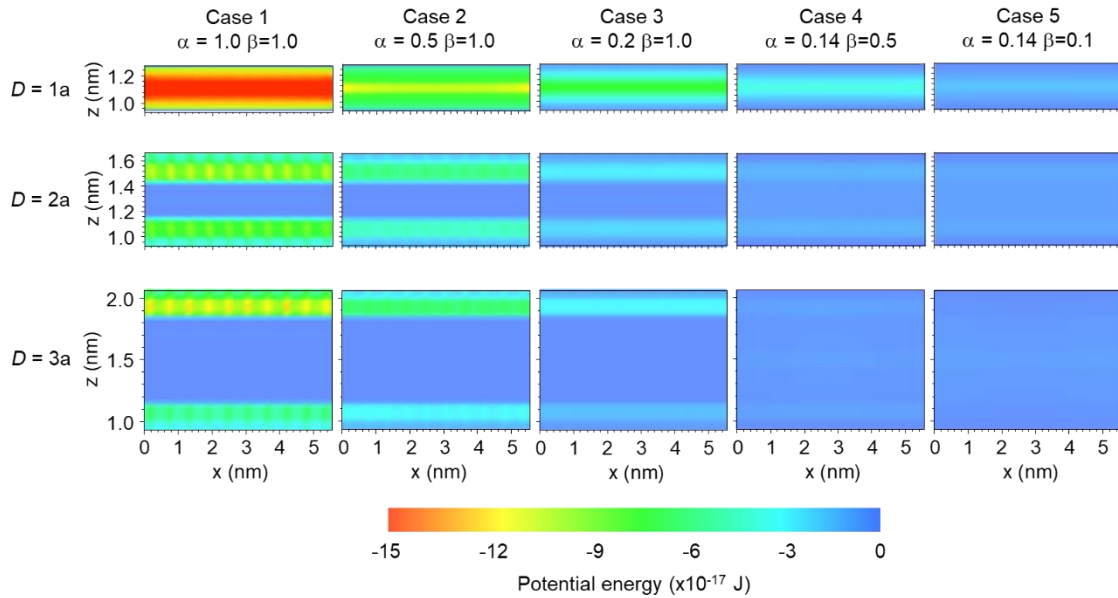


**Fig. 5.5** Contours of potential energy under the varying solid–liquid interaction at  $D = 1–3a$ .

Coinciding with the potential energy results, in the case of  $D = 1a$ , the kinetic energy of the liquid is significantly higher than that at  $D = 2a$  and  $3a$ , owing to the liquid monolayer confined firmly in the nanogap between two solid walls. The kinetic energy of the liquid layer keeps nearly constant even though the interaction energy is varied by energy parameter  $\alpha$  and  $\beta$  from cases 1 to 5. However, in the case of  $D = 2a$ , the kinetic energy of the liquid is concentrated on the two sides near solid walls when

two liquid layers are adsorbed onto the solid surfaces in cases 1–3, while it is uniformly distributed in the nanogap in cases 4–5. In addition, we can observe similar results of kinetic energy when  $D = 3a$  under the different solid–liquid interactions.

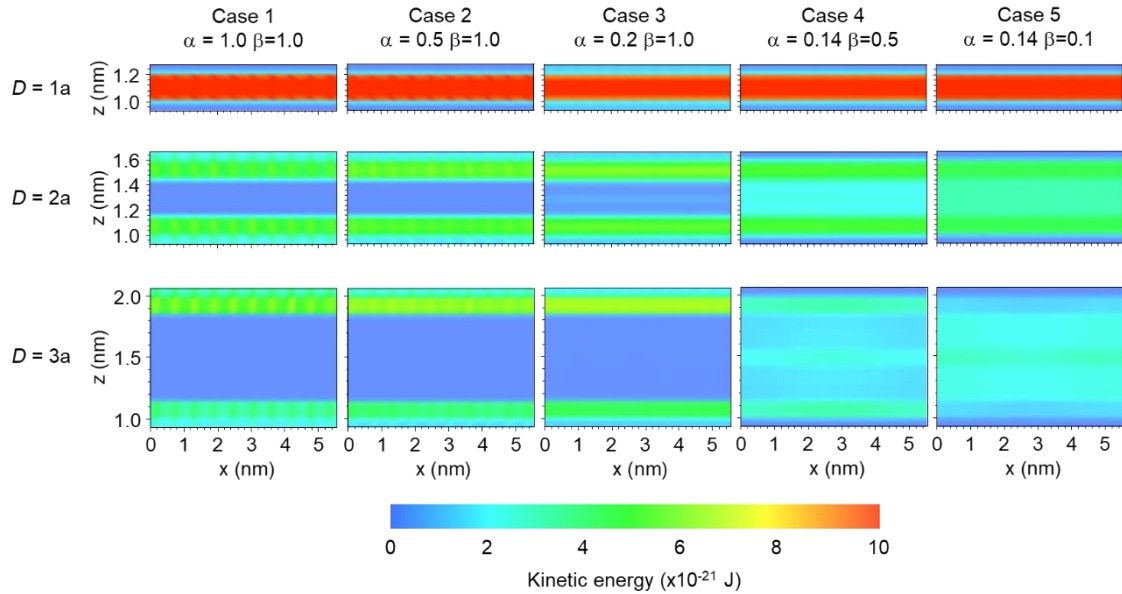


**Fig. 5.6** Contours of kinetic energy under the varying solid–liquid interaction at  $D = 1–3a$ .

### 5.3.3 Net heat flux and thermal gap conductance

The net heat flux  $q$  and thermal gap conductance  $G$  are obtained by conducting data sampling over a period of 15 ns after NEMD simulation systems achieve the steady state, as shown in Fig. 5.7. In the case of  $D = 1a$ ,  $q$  and  $G$  increase with strengthening the solid–liquid interaction, which agrees well with the results in previous studies. Interestingly,  $q$  and  $G$  get up to maximum under weak solid–liquid interaction in case 3 at  $D = 2a$  and in case 4 at  $D = 3a$ , respectively. As shown in Fig. 5.2, when liquid atoms diffuse in a nanogap, thermal energy transportation across a nanogap is improved

significantly. Thus, the mechanism of thermal energy transport across a nanogap with non-adsorbed liquid atoms includes both the contributions of solid atomic vibrations and liquid atomic collisions.

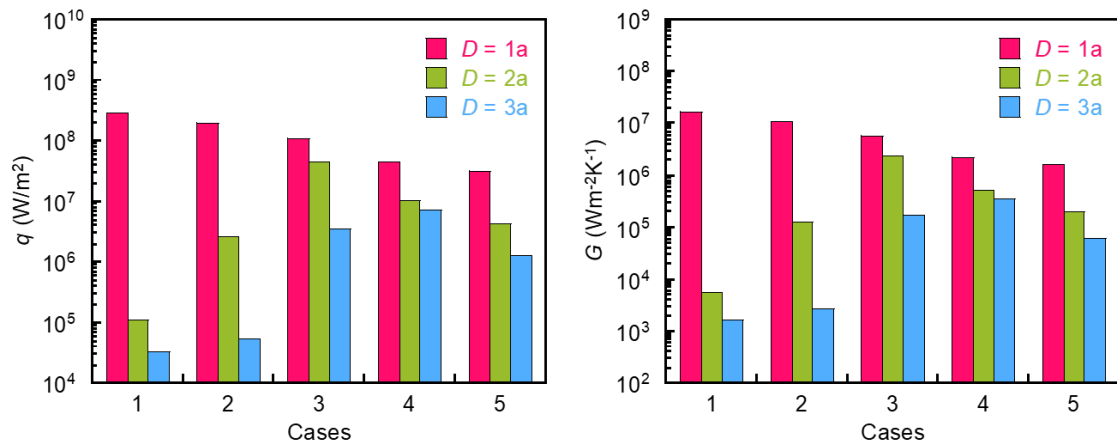


**Fig. 5.7** Heat flux and thermal gap conductance in all cases with varying solid–liquid interaction at  $D = 1-3a$ .

### 5.3.4 Atomic vibrational displacement of liquid atoms

To verify the heat transfer enhancement under weak solid–liquid interaction at  $D = 2a$ , the atomic vibrational displacements of liquid atoms neighboring the heating and cooling solid surfaces are analyzed, as shown in Fig. 5.8. The peak amplitudes of the liquid atoms increase with weakening the solid–liquid interactions from cases 1–5; meanwhile, the vibrational frequencies of the liquid atoms become smaller due to the weaker couple degree between solid and liquid atoms. Moreover, we observed that the wave packet is generated when the liquid atoms are adsorbed on the solid surfaces, while the mechanism of heat transfer enhancement with weak solid–liquid interaction is still unclear.

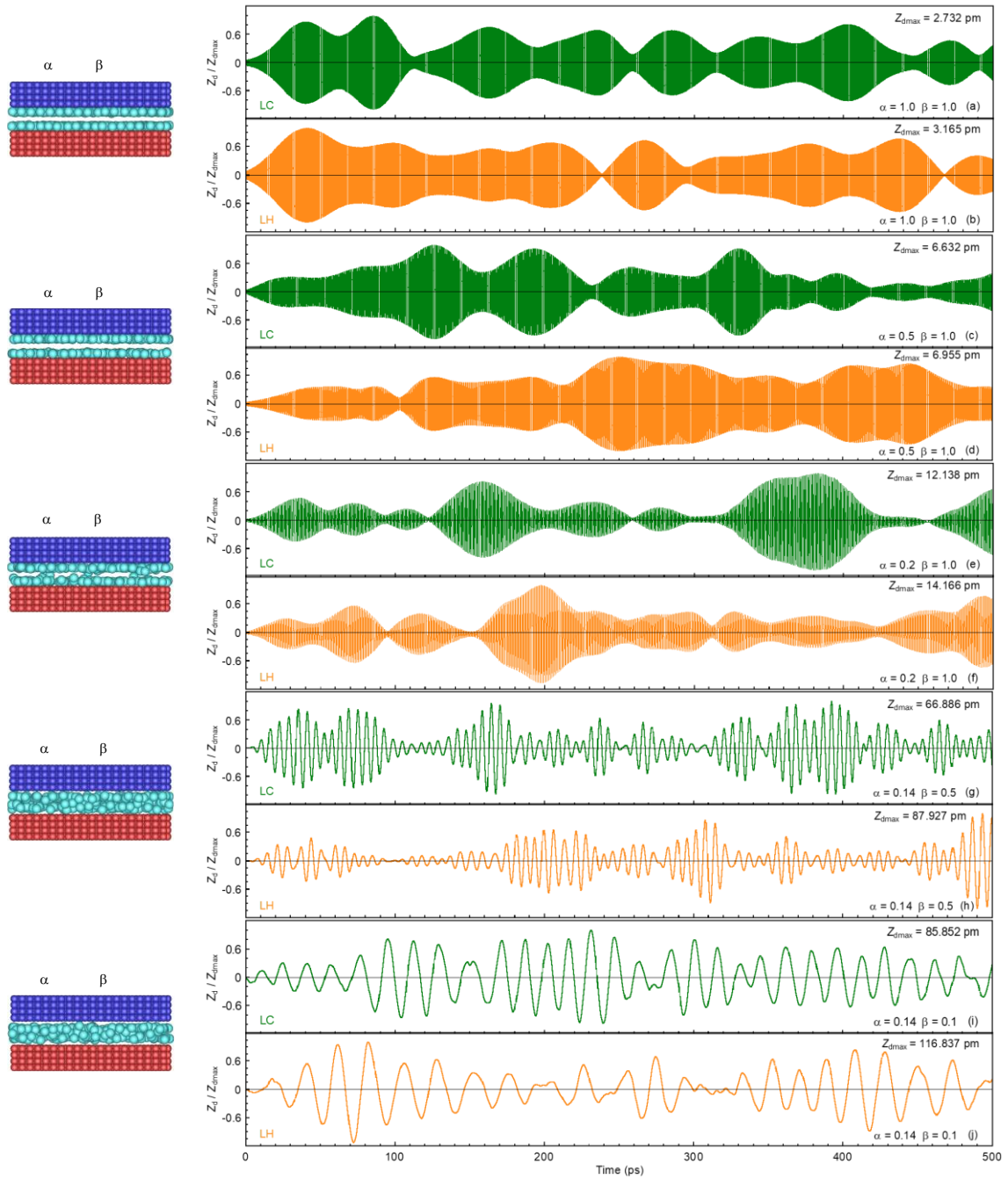


**Fig. 5.8** Atomic vibrational displacements of specific liquid atoms near heating and cooling solid surfaces at varying potential energy factor: (a–b)  $\alpha = 1.0$  and  $\beta = 1.0$ ; (c–d)  $\alpha = 0.5$  and  $\beta = 1.0$ ; (e–f)  $\alpha = 0.2$  and  $\beta = 1.0$ ; (g–h)  $\alpha = 0.14$  and  $\beta = 0.5$ ; (i–j)  $\alpha = 0.14$  and  $\beta = 0.1$ .

### 5.3.5 VDOS of interfacial solid layers

To understand the mechanism of heat transfer enhancement deeply with weak solid–liquid interaction, we calculated the VDOS of interfacial solid layers 4 and 5, as shown in Fig. 5.9. In the case of  $D = 1a$ , the thermal resonance occurs between the interfacial solid layers 4 and 5, which is evidenced by the overlapped VDOS of layers 4 and 5 shown in Fig. 5.9(a)–(e). Moreover, the peak of the VDOSs of the interfacial solid layers increases with the strengthening of the solid–liquid interaction, resulting in the improvement of thermal energy transportation. In the case of  $D = 2a$ , the thermal resonance only exists between interfacial solid layers when  $\alpha = 0.2$  and  $\beta = 1.0$ . Accordingly, the net heat flux  $q$  and thermal gap conductance  $G$  get maximum under the weak solid–liquid interaction in Fig. 5.9(f–j). Furthermore, in the case of  $D = 3a$ , the phonon mismatch between the interfacial solid layers is almost negligible when  $\alpha = 0.14$  and  $\beta = 0.5$ , resulting in the highest net heat flux and thermal gap conductance.

### 5.3.6 Knudsen number effects

The effects of the solid–liquid interaction and the nanogap size between the two solid walls on phonon heat transfer across a nanogap were analyzed in the above sections. Subsequently, the number of argon atoms in the nanogap was varied to investigate the relationship between Knudsen number  $Kn$  and thermal energy transport across the nanogap. The snapshots of the simulated systems with different argon atoms are shown in Fig. 5.10. The Knudsen number is defined as the ratio of the mean free path  $\lambda$  to the characteristic length of the domain  $L$ .

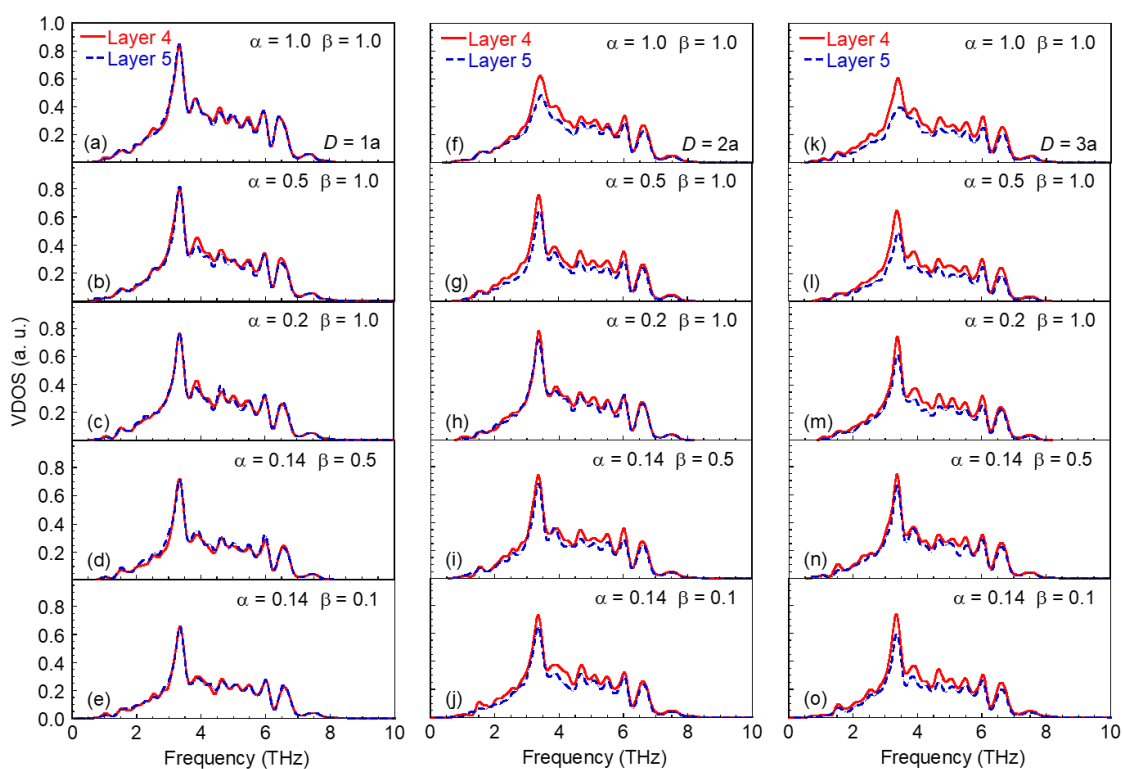


**Fig. 5.9** VDOS of layers 4 and 5 under different solid–liquid interaction at varying gap distance: (a–e)  $D = 1a$ ; (f–j)  $D = 2a$ ; (k–o)  $D = 3a$ .

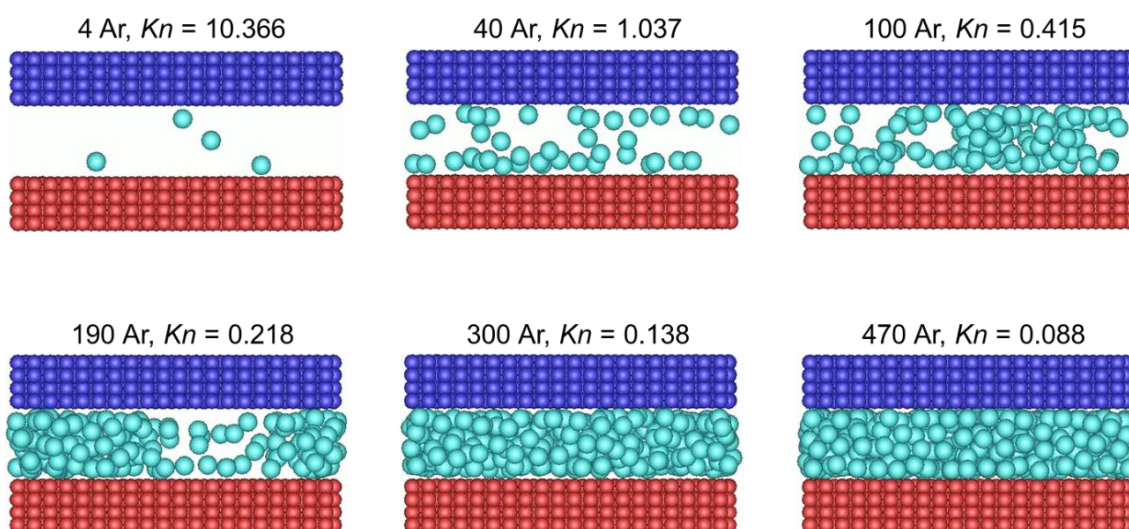


**Fig. 5.10** Snapshots of the simulated systems at varying Knudsen numbers.

In our particular cases, we calculated the values of  $Kn$  from  $Kn = \lambda / L = 1 / \sqrt{2\pi n \sigma^2 L}$ , where  $n$  is the number density of argon atoms and  $\sigma$  is the length parameter signifying the atom diameter. The values of parameters are shown in Table 5-1.

**Table 5-1** Simulation cases and the values of parameters.

Cases	Ar atoms	$n \times 10^{26}$ (1/m <sup>3</sup> )	$\lambda \times 10^{-10}$ (m)	$Kn$
1	4	1.593	121.905	10.366
2	40	15.925	12.190	1.037
3	100	39.813	4.876	0.415
4	190	75.644	2.566	0.218
5	300	119.438	1.625	0.138
6	470	187.119	1.037	0.088

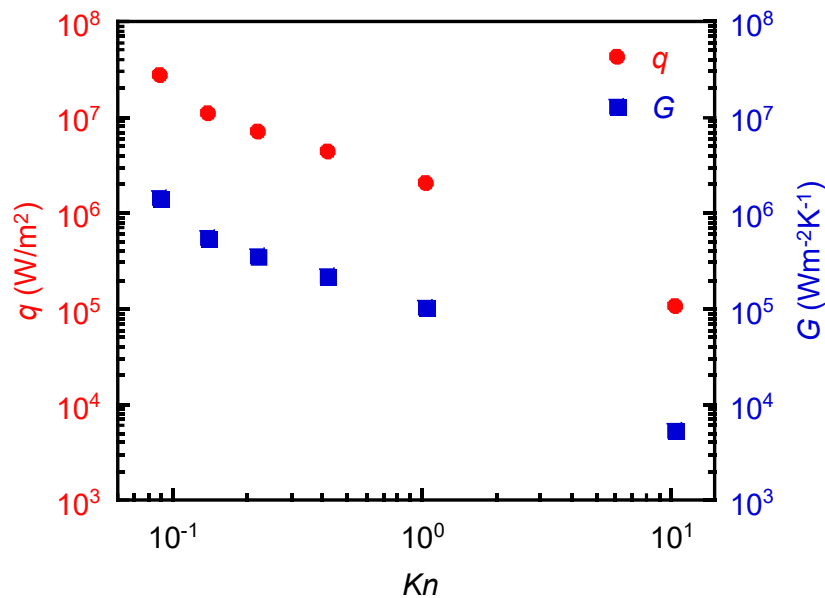


**Fig. 5.11** Heat flux and thermal gap conductance versus Knudsen number.

The net heat flux  $q$  and thermal gap conductance  $G$  were obtained by performing the data sampling over 15 ns to investigate the  $Kn$ -dependent phonon heat transfer across a nanogap. As shown in Fig. 5.11,  $q$  and  $G$  decrease exponentially with increasing Knudsen number, which are most significant in the slip flow regime and most minor in the free molecular flow regime. Therefore, the liquid atomic number in a nanogap is a critical factor for quasi-Casimir phonon heat transfer across a nanogap.

## **5.4 Summary**

NEMD simulations were performed to analyze the effects of solid–liquid interaction on phonon heat transfer across a nanogap. The solid–liquid interaction was changed by the potential energy factors to investigate quasi-Casimir coupling across a nanogap including the non-adsorbed liquid atoms. Our findings can be summarized as follows:

- (1) Quasi-Casimir coupling can exist between the interfacial solid layers in simulation systems with non-adsorbed liquid atoms in the nanogap under weak solid–liquid interaction.
- (2) Differing from the adsorbed solid-like liquid layers, the liquid atoms move randomly and frequently collide with other liquid and interfacial solid atoms. Therefore, the mechanism of thermal energy transport includes both the contribution of solid atomic vibrations and liquid atomic collisions.
- (3) Phonon mismatch between the interfacial solid layers decreases with liquid atomic collisions, resulting in the enhancement of phonon heat transfer across a nanogap.

In this study, we verified that the weak solid–liquid interaction could enhance phonon heat transfer across a nanogap, including non-adsorbed liquid atoms. However, phonon

transmission across a nanogap, including water layers with and without an external electric field is still an open question. In future work, we expect to investigate the quasi-Casimir phonon heat transfer across a nanogap via the water layers. The counterintuitive finding of the phonon heat transfer under weak solid–liquid interaction provides insight into the development of near-field heat transfer.

## **Chapter 6**

# **6 Conclusions and outlook**

## **6.1 Conclusions**

In this thesis, the molecular dynamics simulation method was utilized to explore a new heat transfer mode, named quasi-Casimir heat transfer across a nanogap. This mode is different from conventional heat conduction, convection, radiation and is independent of electrostatic interaction, electron cloud overlap, surface phonon polaritons, and surface plasmon polaritons. We verified that quasi-Casimir coupling could exist between solid–solid, solid–liquid, and liquid–liquid layers. The main findings of this study are summarized below.

The first study presented a quasi-Casimir coupling model for phonon heat transfer between two parallel solid walls separated by a sub-nanometer vacuum gap in the absence of an electromagnetic field. The phonon heat transfer is investigated in systems by performing a classical molecular dynamics simulation to verify the quasi-Casimir coupling model. We evidenced the phonon heat transfer induced by the intermolecular interactive force across the vacuum gap with significant interfacial resonance.

The second study examined the phonon heat transfer across a nanogap with liquid layers, with a focus on the quasi-Casimir coupling and thermal resonance, using the classical non-equilibrium molecular dynamics simulations. The liquid monolayer adsorbed on the cooling/heating surfaces and two liquid layers adsorbed on both the cooling and heating surfaces were simulated to verify the quasi-Casimir coupling and

thermal resonance. The thermal resonance between the two liquid layers induced by quasi-Casimir coupling can agitate the co-occurrence of the thermal resonance between the interfacial solid layers.

The third study analyzed the mechanism of phonon heat transfer across a nanogap including liquid, under the varying strength of molecular interaction between solid and liquid. We have evidenced that weak solid–liquid interaction can enhance thermal energy transportation across a nanogap. The root reason for this heat transfer enhancement attributes to the decreased phonon mismatch between the interfacial solid layers.

## **6.2 Outlook**

Near-field heat transfer has a promising future due to its relevance to nanoscale thermal management and potential industrial applications. Our current studies only provide the fundamental understanding of the quasi-Casimir heat transfer across a sub-nanometer gap, which motivates us to develop it in nanoscale thermal devices. Thus, in the near future, we would like to perform more MD simulations to verify the existence of quasi-Casimir heat transfer in other systems, including the dielectric solid materials and water. Furthermore, the quasi-Casimir heat transfer across a nanogap with an electrical field will be compared with the present study using the MD simulation method by LAMMPS. We also would like to investigate the effects of surface orientation, solid thickness, and nanostructures on quasi-Casimir phonon heat transfer across a nanogap. Finally, we will perform experiments to confirm this new heat transfer mechanism of quasi-Casimir coupling.

## Reference

- [1] B. Song, A. Fiorino, E. Meyhofer, P. Reddy, Near-field radiative thermal transport: From theory to experiment, *AIP Adv.* 5 (2015) 53503.
- [2] A.I. Volokitin, Contribution of the acoustic waves to near-field heat transfer, *J. Phys. Condens. Matter.* 32 (2020) 215001.
- [3] M. Nomura, Near-field radiative heat transfer: The heat through the gap, *Nat. Nanotechnol.* 11 (2016) 496–497.
- [4] B. Song, Y. Ganjeh, S. Sadat, D. Thompson, A. Fiorino, V. Fernández-Hurtado, J. Feist, F.J. Garcia-Vidal, J.C. Cuevas, P. Reddy, E. Meyhofer, Enhancement of near-field radiative heat transfer using polar dielectric thin films, *Nat. Nanotechnol.* 10 (2015) 253–258.
- [5] B. Song, D. Thompson, A. Fiorino, Y. Ganjeh, P. Reddy, E. Meyhofer, Radiative heat conductances between dielectric and metallic parallel plates with nanoscale gaps, *Nat. Nanotechnol.* 11 (2016) 509–514.
- [6] K. Kim, B. Song, V. Fernández-Hurtado, W. Lee, W. Jeong, L. Cui, D. Thompson, J. Feist, M.T.H. Reid, F.J. García-Vidal, J.C. Cuevas, E. Meyhofer, P. Reddy, Radiative heat transfer in the extreme near field, *Nature.* 528 (2015) 387–391.
- [7] M.P. Bernardi, D. Milovich, M. Francoeur, Radiative heat transfer exceeding the blackbody limit between macroscale planar surfaces separated by a nanosize vacuum gap, *Nat. Commun.* 7 (2016) 1–7.
- [8] A. Fiorino, D. Thompson, L. Zhu, B. Song, P. Reddy, E. Meyhofer, Giant Enhancement in Radiative Heat Transfer in Sub-30 nm Gaps of Plane Parallel

- Surfaces, *Nano Lett.* 18 (2018) 3711–3715.
- [9] A. Fiorino, D. Thompson, L. Zhu, R. Mittapally, S.A. Biehs, O. Bezencenet, N. El-Bondry, S. Bansropun, P. Ben-Abdallah, E. Meyhofer, P. Reddy, A Thermal Diode Based on Nanoscale Thermal Radiation, *ACS Nano*. 12 (2018) 5174–5179.
- [10] L. Zhu, A. Fiorino, D. Thompson, R. Mittapally, E. Meyhofer, P. Reddy, Near-field photonic cooling through control of the chemical potential of photons, *Nature*. 566 (2019) 239–244.
- [11] B. Guha, C. Otey, C.B. Poitras, S. Fan, M. Lipson, Near-field radiative cooling of nanostructures, *Nano Lett.* 12 (2012) 4546–4550.
- [12] J. Cho, K.E. Goodson, Thermal transport: Cool electronics, *Nat. Mater.* 14 (2015) 136–137.
- [13] A. Fiorino, L. Zhu, D. Thompson, R. Mittapally, P. Reddy, E. Meyhofer, Nanogap near-field thermophotovoltaics, *Nat. Nanotechnol.* 13 (2018) 806–811.
- [14] H. Li, B. Liu, T.C. Chong, Thermal study of nanometer-spaced head-disk systems, *Jpn. J. Appl. Phys.* 44 (2005) 7445–7447.
- [15] E. Albisetti, D. Petti, M. Pancaldi, M. Madami, S. Tacchi, J. Curtis, W.P. King, A. Papp, G. Csaba, W. Porod, Nanopatterning reconfigurable magnetic landscapes via thermally assisted scanning probe lithography, *Nat. Nanotechnol.* 11 (2016) 545–551.
- [16] B. V. Budaev, D.B. Bogy, Computation of radiative heat transport across a nanoscale vacuum gap, *Appl. Phys. Lett.* 104 (2014) 061109.
- [17] L. Tranchant, S. Hamamura, J. Ordonez-Miranda, T. Yabuki, A. Vega-Flick, F. Cervantes-Alvarez, J.J. Alvarado-Gil, S. Volz, K. Miyazaki, Two-Dimensional Phonon Polariton Heat Transport, *Nano Lett.* 19 (2019) 6924–6930.

- 
- [18] S. Shen, A. Narayanaswamy, G. Chen, Surface phonon polaritons mediated energy transfer between nanoscale gaps, *Nano Lett.* 9 (2009) 2909–2913.
- [19] K. Kloppstech, N. Köhne, S.A. Biehs, A.W. Rodriguez, L. Worbes, D. Hellmann, A. Kittel, Giant heat transfer in the crossover regime between conduction and radiation, *Nat. Commun.* 8 (2017) 1–6.
- [20] G. Domingues, S. Volz, K. Joulain, J.J. Greffet, Heat transfer between two nanoparticles through near field interaction, *Phys. Rev. Lett.* 94 (2005) 2–5.
- [21] I. Altfeder, A.A. Voevodin, A.K. Roy, Vacuum phonon tunneling, *Phys. Rev. Lett.* 105 (2010) 1–4.
- [22] C. Yang, X. Wei, J. Sheng, H. Wu, Phonon heat transport in cavity-mediated optomechanical nanoresonators, *Nat. Commun.* 11 (2020) 2–7.
- [23] M. Prunnila, J. Meltaus, Acoustic phonon tunneling and heat transport due to evanescent electric fields, *Phys. Rev. Lett.* 105 (2010) 1–4.
- [24] J.B. Pendry, K. Sasihithlu, R. V. Craster, Phonon-assisted heat transfer between vacuum-separated surfaces, *Phys. Rev. B.* 94 (2016) 1–10.
- [25] B. V. Budaev, D.B. Bogy, On the role of acoustic waves (phonons) in equilibrium heat exchange across a vacuum gap, *Appl. Phys. Lett.* 99 (2011) 1–4.
- [26] A. Alkurdi, C. Adessi, F. Tabatabaei, S. Li, K. Termentzidis, S. Merabia, Thermal transport across nanometre gaps: Phonon transmission vs. air conduction, *Int. J. Heat Mass Transf.* 158 (2020) 119963.
- [27] D.P. Sellan, E.S. Landry, K. Sasihithlu, A. Narayanaswamy, A.J.H. McGaughey, C.H. Amon, Phonon transport across a vacuum gap, *Phys. Rev. B.* 85 (2012) 1–6.
- [28] A.I. Volokitin, Effect of an Electric Field in the Heat Transfer between Metals in the Extreme Near Field, *JETP Lett.* 109 (2019) 749–754.

- 
- [29] S. Xiong, K. Yang, Y.A. Kosevich, Y. Chalopin, R. D'Agosta, P. Cortona, S. Volz, Classical to Quantum Transition of Heat Transfer between Two Silica Clusters, *Phys. Rev. Lett.* 112 (2014) 114301.
- [30] V. Chiloyan, J. Garg, K. Esfarjani, G. Chen, Transition from near-field thermal radiation to phonon heat conduction at sub-nanometre gaps, *Nat. Commun.* 6 (2015) 6755.
- [31] T. Tokunaga, A. Jarzembski, T. Shiga, K. Park, M. Francoeur, Extreme Near-Field Heat Transfer Between Gold Surfaces, *Phys. Rev. B.* 104 (2021) 25–30.
- [32] A. Jarzembski, T. Tokunaga, J. Crossley, J. Yun, C. Shaskey, R.A. Murdick, I. Park, M. Francoeur, K. Park, Force-induced acoustic phonon transport across single-digit nanometre vacuum gaps, *ArXiv: 1904.09383.* (2019).
- [33] M.C. Coles, C.D. Buckley, Heat transferred in a previously unknown way, *Nature.* 576 (2019) 216–217.
- [34] H.B.G. Casimir, On the attraction between two perfectly conducting plates, *Proc. K. Ned. Akad.* 360 (1948) 793–795.
- [35] Y. Ezzahri, K. Joulain, Vacuum-induced phonon transfer between two solid dielectric materials: Illustrating the case of Casimir force coupling, *Phys. Rev. B.* 90 (2014) 1–7.
- [36] K.Y. Fong, H.-K. Li, R. Zhao, S. Yang, Y. Wang, X. Zhang, Phonon heat transfer across a vacuum through quantum fluctuations, *Nature.* 576 (2019) 243–247.
- [37] Z. Ge, D.G. Cahill, P. V. Braun, Thermal conductance of hydrophilic and hydrophobic interfaces, *Phys. Rev. Lett.* 96 (2006) 1–4.
- [38] H. Harikrishna, W.A. Ducker, S.T. Huxtable, The influence of interface bonding

- 
- on thermal transport through solid-liquid interfaces, *Appl. Phys. Lett.* 102 (2013) 251606.
- [39] J. Ghorbanian, A. Beskok, Scale effects in nano-channel liquid flows, *Microfluid. Nanofluidics.* 20 (2016) 1–11.
- [40] D.P. Sellan, E.S. Landry, J.E. Turney, A.J.H. McGaughey, C.H. Amon, Size effects in molecular dynamics thermal conductivity predictions, *Phys. Rev. B.* 81 (2010) 1–10.
- [41] C. Jiang, J. Ouyang, L. Wang, Q. Liu, X. Wang, Transport properties and structure of dense methane fluid in the rough nano-channels using non-equilibrium multiscale molecular dynamics simulation, *Int. J. Heat Mass Transf.* 110 (2017) 80–93.
- [42] X. Liu, D. Surblys, Y. Kawagoe, A.R. Bin Saleman, H. Matsubara, G. Kikugawa, T. Ohara, A molecular dynamics study of thermal boundary resistance over solid interfaces with an extremely thin liquid film, *Int. J. Heat Mass Transf.* 147 (2020) 118949.
- [43] B.H. Kim, A. Beskok, T. Cagin, Molecular dynamics simulations of thermal resistance at the liquid-solid interface, *J. Chem. Phys.* 129 (2008) 174701.
- [44] T.Q. Vo, B. Kim, Transport phenomena of water in molecular fluidic channels, *Sci. Rep.* 6 (2016) 1–8.
- [45] B. Kim, Thermal resistance at a liquid-solid interface dependent on the ratio of thermal oscillation frequencies, *Chem. Phys. Lett.* 554 (2012) 77–81.
- [46] X. Wang, P. Cheng, X. Quan, Molecular dynamics simulations of thermal boundary resistances in a liquid between two solid walls separated by a nano gap, *Int. Commun. Heat Mass Transf.* 77 (2016) 183–189.

- [47] C.U. Gonzalez-Valle, S. Kumar, B. Ramos-Alvarado, Investigation on the Wetting Behavior of 3C-SiC Surfaces: Theory and Modeling, *J. Phys. Chem. C.* 122 (2018) 7179–7186.
- [48] A.T. Pham, M. Barisik, B. Kim, Molecular dynamics simulations of Kapitza length for argon-silicon and water-silicon interfaces, *Int. J. Precis. Eng. Manuf.* 15 (2014) 323–329.
- [49] B. Ramos-Alvarado, S. Kumar, G.P. Peterson, Solid-Liquid Thermal Transport and Its Relationship with Wettability and the Interfacial Liquid Structure, *J. Phys. Chem. Lett.* 7 (2016) 3497–3501.
- [50] G. Nagayama, P. Cheng, Effects of interface wettability on microscale flow by molecular dynamics simulation, *Int. J. Heat Mass Transf.* 47 (2004) 501–513.
- [51] G. Nagayama, M. Kawagoe, A. Tokunaga, T. Tsuruta, On the evaporation rate of ultra-thin liquid film at the nanostructured surface: A molecular dynamics study, *Int. J. Therm. Sci.* 49 (2010) 59–66.
- [52] T. Lin, J. Li, X. Quan, P. Cheng, A molecular dynamics investigation on effects of nanostructures on thermal conductance across a nanochannel, *Int. Commun. Heat Mass Transf.* 97 (2018) 118–124.
- [53] Y. Chen, P. Fu, C. Zhang, M. Shi, Numerical simulation of laminar heat transfer in microchannels with rough surfaces characterized by fractal Cantor structures, *Int. J. Heat Fluid Flow.* 31 (2010) 622–629.
- [54] D. Surblys, Y. Kawagoe, M. Shibahara, T. Ohara, Molecular dynamics investigation of surface roughness scale effect on interfacial thermal conductance at solid-liquid interfaces, *J. Chem. Phys.* 150 (2019) 114705.
- [55] Y. Guo, D. Surblys, H. Matsubara, T. Ohara, A molecular dynamics study of the

- effect of functional groups and side chain on adsorption of alcoholic surfactant and interfacial thermal transport, *J. Mol. Liq.* 335 (2021) 116243.
- [56] Y. Guo, D. Surblys, Y. Kawagoe, H. Matsubara, T. Ohara, A molecular dynamics study of heat transfer over an ultra-thin liquid film with surfactant between solid surfaces, *J. Appl. Phys.* 126 (2019) 1–12.
- [57] Y. Guo, D. Surblys, H. Matsubara, Y. Kawagoe, T. Ohara, Molecular dynamics study on the effect of long-chain surfactant adsorption on interfacial heat transfer between a polymer liquid and silica surface, *J. Phys. Chem. C.* 124 (2020) 27558–27570.
- [58] T. Zhang, A.R. Gans-Forrest, E. Lee, X. Zhang, C. Qu, Y. Pang, F. Sun, T. Luo, Role of Hydrogen Bonds in Thermal Transport across Hard/Soft Material Interfaces, *ACS Appl. Mater. Interfaces.* 8 (2016) 33326–33334.
- [59] X. Wei, T. Zhang, T. Luo, Molecular fin effect from heterogeneous self-assembled monolayer enhances thermal conductance across hard-soft interfaces, *ACS Appl. Mater. Interfaces.* 9 (2017) 33740–33748.
- [60] T. Luo, J.R. Lloyd, Non-equilibrium molecular dynamics study of thermal energy transport in Au-SAM-Au junctions, *Int. J. Heat Mass Transf.* 53 (2010) 1–11.
- [61] M. Barisik, A. Beskok, Temperature dependence of thermal resistance at the water/silicon interface, *Int. J. Therm. Sci.* 77 (2014) 47–54.
- [62] G. Song, C. Min, Temperature dependence of thermal resistance at a solid/liquid interface, *Mol. Phys.* 111 (2013) 903–908.
- [63] L. Xue, P. Keblinski, S.R. Phillpot, S.U.S. Choi, J.A. Eastman, Two regimes of thermal resistance at a liquid-solid interface, *J. Chem. Phys.* 118 (2003) 337–339.
- [64] H. Han, S. Mérabia, F. Müller-Plathe, Thermal Transport at Solid-Liquid

- Interfaces: High Pressure Facilitates Heat Flow through Nonlocal Liquid Structuring, *J. Phys. Chem. Lett.* 8 (2017) 1946–1951.
- [65] A. Pham, M. Barisik, B. Kim, Pressure dependence of Kapitza resistance at gold/water and silicon/water interfaces, *J. Chem. Phys.* 139 (2013) 244702.
- [66] G. Nagayama, T. Matsumoto, K. Fukushima, T. Tsuruta, Scale effect of slip boundary condition at solid-liquid interface, *Sci. Rep.* 7 (2017) 1–8.
- [67] R. Rabani, G. Heidarinejad, J. Harting, E. Shirani, Interplay of confinement and density on the heat transfer characteristics of nanoscale-confined gas, *Int. J. Heat Mass Transf.* 126 (2018) 331–341.
- [68] O. Yenigun, M. Barisik, Effect of nano-film thickness on thermal resistance at water/silicon interface, *Int. J. Heat Mass Transf.* 134 (2019) 634–640.
- [69] Y. Chen, C. Zhang, Role of surface roughness on thermal conductance at liquid-solid interfaces, *Int. J. Heat Mass Transf.* 78 (2014) 624–629.
- [70] M. Shibahara, K. Inoue, K. Kobayashi, A Molecular Dynamics Study on Effects of Nanostructural Clearances at an Interface on Thermal Resistance, *J. Therm. Sci. Technol.* (2009) 485–491.
- [71] L. Xue, P. Keblinski, S.R. Phillpot, S.U.S. Choi, J.A. Eastman, Effect of liquid layering at the liquid-solid interface on thermal transport, *Int. J. Heat Mass Transf.* 47 (2004) 4277–4284.
- [72] M. Frank, D. Drikakis, Solid-like heat transfer in confined liquids, *Microfluid. Nanofluidics.* 21 (2017) 1–6.
- [73] Z. Liang, H.L. Tsai, Thermal conductivity of interfacial layers in nanofluids, *Phys. Rev. E.* 83 (2011) 1–8.
- [74] X. Wang, D. Jing, Determination of thermal conductivity of interfacial layer in

- nanofluids by equilibrium molecular dynamics simulation, *Int. J. Heat Mass Transf.* 128 (2019) 199–207.
- [75] Z. Liang, H.L. Tsai, Effect of molecular film thickness on thermal conduction across solid-film interfaces, *Phys. Rev. E.* 83 (2011) 1–7.
- [76] P.S. Laplace, *A philosophical essay on probabilities*: Pierre Simon, Dover, 1952.
- [77] B.J. Alder, T.E. Wainwright, Phase transition for a hard sphere system, *J. Chem. Phys.* 27 (1957) 1208–1209.
- [78] J.B. Gibson, A.N. Goland, M. Milgram, G. Vineyard, Dynamics of radiation damage, *Phys. Rev.* 120 (1960) 1229.
- [79] A. Rahman, Correlations in the motion of atoms in liquid argon, *Phys. Rev.* 136 (1964) A405.
- [80] D. Landau, K. Binder, *A guide to Monte Carlo simulations in statistical physics*, Cambridge university press, 2021.
- [81] M.P. Allen, D.J. Tildesley, *Computer simulation of liquids*, Oxford university press, 2017.
- [82] B.J. Berne, D. Thirumalai, On the simulation of quantum systems: path integral methods, *Annu. Rev. Phys. Chem.* 37 (1986) 401–424.
- [83] M.J. Gillan, The path-integral simulation of quantum systems. In *Computer Modelling of Fluids Polymers and Solids*, Springer, 1990.
- [84] M.E. Tuckerman, M. Parrinello, Integrating the Car–Parrinello equations. I. Basic integration techniques, *J. Chem. Phys.* 101 (1994) 1302–1315.
- [85] D.K. Remler, P.A. Madden, Molecular dynamics without effective potentials via the Car-Parrinello approach, *Mol. Phys.* 70 (1990) 921–966.
- [86] G.D. Doolen, *Lattice gas methods: theory, applications, and hardware*, MIT press,

- 1991.
- [87] E.M. Yezdimer, A.A. Chialvo, P.T. Cummings, Examination of chain length effects on the solubility of alkanes in near-critical and supercritical aqueous solutions, *J. Phys. Chem. B.* 105 (2001) 841–847.
- [88] J. Delhommelle, P. Millié, Inadequacy of the Lorentz-Berthelot combining rules for accurate predictions of equilibrium properties by molecular simulation, *Mol. Phys.* 99 (2001) 619–625.
- [89] X.D. Din, E.E. Michaelides, Kinetic theory and molecular dynamics simulations of microscopic flows, *Phys. Fluids.* 9 (1997) 3915–3925.
- [90] J. Barrat, Large Slip Effect at a Nonwetting Fluid-Solid Interface Jean-Louis, *Phys. Rev. Lett.* 82 (1999) 4671–4674.
- [91] G. Nagayama, K. Yanai, K. Kurokawa, T. Tsuruta, Microscopic Wetting at Nanostructured Surface: A Molecular Dynamics Study, *Int. Conf. Micro/Nanoscale Heat Transf.* 43918 (2009) 615–621.
- [92] W.C. Swope, H.C. Andersen, P.H. Berens, K.R. Wilson, A computer simulation method for the calculation of equilibrium constants for the formation of physical clusters of molecules: Application to small water clusters, *J. Chem. Phys.* 76 (1982) 637–649.
- [93] A. V Oppenheim, *Signals, Systems and Interference*, 1st Ed., Pearson, Boston, 2016.
- [94] H. Bao, J. Chen, X. Gu, B. Cao, A review of Simulation Methods in Micro/Nanoscale Heat Conduction, *ES Energy Environ.* 1 (2018) 16–55.
- [95] Y. Guo, D. Surblys, Y. Kawagoe, H. Matsubara, X. Liu, T. Ohara, A molecular dynamics study on the effect of surfactant adsorption on heat transfer at a solid-

- liquid interface, *Int. J. Heat Mass Transf.* 135 (2019) 115–123.
- [96] J.H. Irving, J.G. Kirkwood, The statistical mechanical theory of transport processes. IV. The equations of hydrodynamics, *J. Chem. Phys.* 18 (1950) 817–829.
- [97] H.K. Chilukoti, T. Zhou, V.R. Ardham, M.C. Böhm, F. Müller-Plathe, Thermal Energy Transport across the Interface between Phase Change Material n-Heneicosane in Solid and Liquid Phases and Few-Layer Graphene, *J. Phys. Chem. C.* 123 (2019) 29192–29202.
- [98] C.U. Gonzalez-Valle, B. Ramos-Alvarado, Spectral mapping of thermal transport across SiC-water interfaces, *Int. J. Heat Mass Transf.* 131 (2019) 645–653.
- [99] C.U. Gonzalez-Valle, L.E. Paniagua-Guerra, B. Ramos-Alvarado, Implications of the Interface Modeling Approach on the Heat Transfer across Graphite-Water Interfaces, *J. Phys. Chem. C.* 123 (2019) 22311–22323.
- [100] R. Khare, P. Keblinski, A. Yethiraj, Molecular dynamics simulations of heat and momentum transfer at a solid-fluid interface: Relationship between thermal and velocity slip, *Int. J. Heat Mass Transf.* 49 (2006) 3401–3407.
- [101] P. Gao, S. Le Person, M. Favre-Marinet, Scale effects on hydrodynamics and heat transfer in two-dimensional mini and microchannels, *Int. J. Therm. Sci.* 41 (2002) 1017–1027.
- [102] C.U. Gonzalez-Valle, S. Kumar, B. Ramos-Alvarado, Thermal Transport across SiC–Water Interfaces, *ACS Appl. Mater. Interfaces.* 10 (2018) 29179–29186.
- [103] K. Tanaka, S. Ogata, R. Kobayashi, T. Tamura, T. Kouno, A molecular dynamics study on thermal conductivity of thin epoxy polymer sandwiched between alumina fillers in heat-dissipation composite material, *Int. J. Heat Mass Transf.*

- 89 (2015) 714–723.
- [104] B. Ramos-Alvarado, S. Kumar, Spectral Analysis of the Heat Flow Across Crystalline and Amorphous Si-Water Interfaces, *J. Phys. Chem. C.* 121 (2017) 11380–11389.
- [105] R.J. Sadus, *Molecular simulation of fluids*, 2nd Ed., Elsevier, Netherlands, 2002.
- [106] J.W. Arblaster, Crystallographic properties of ruthenium, *Platin. Met. Rev.* 57 (2013) 127–136.
- [107] M. Barisik, A. Beskok, Boundary treatment effects on molecular dynamics simulations of interface thermal resistance, *J. Comput. Phys.* 231 (2012) 7881–7892.
- [108] G. Nagayama, T. Tsuruta, P. Cheng, Molecular dynamics simulation on bubble formation in a nanochannel, *Int. J. Heat Mass Transf.* 49 (2006) 4437–4443.
- [109] Y. Ma, Z. Zhang, J. Chen, K. Sääskilähti, S. Volz, J. Chen, Ordered water layers by interfacial charge decoration leading to an ultra-low Kapitza resistance between graphene and water, *Carbon.* 135 (2018) 263–269.
- [110] M. Masduzzaman, B. Kim, Scale Effects in Nanoscale Heat Transfer for Fourier’s Law in a Dissimilar Molecular Interface, *ACS Omega.* 5 (2020) 26527–26536.
- [111] H. Sun, F. Li, M. Wang, G. Xin, X. Wang, Molecular dynamics study of convective heat transfer mechanism in a nano heat exchanger, *RSC Adv.* 10 (2020) 23097–23107.
- [112] B.B. Wang, Z.M. Xu, X.D. Wang, W.M. Yan, Molecular dynamics investigation on enhancement of heat transfer between electrified solid surface and liquid water, *Int. J. Heat Mass Transf.* 125 (2018) 756–760.

- [113] W. Chen, G. Nagayama, Quasi-Casimir coupling induced phonon heat transfer across a vacuum gap, *Int. J. Heat Mass Transf.* 176 (2021) 121431.
- [114] P.M. Delhommelle, Inadequacy of the Lorentz–Berthelot combining rules for accurate predictions of equilibrium properties by molecular simulation, *Mol. Phys.* 99 (2001) 619–625.



## **Acknowledgments**

First of all, I would like to express my great gratitude to my supervisor Professor Gyoko Nagayama for her endless motivation and support during my research and thesis. I am sincerely thankful for her academic experiences and knowledge. This thesis would not be finished without her patience and attention to my studies. I also would like to thank Professor Takaharu Tsuruta for his suggestion and kind encouragement about my research. Furthermore, I want to thank Professor Hirofumi Tanigawa for his kind help in my study and life.

Additionally, I would like to thank the rest of my thesis committee: Professor Koji Miyazaki, Professor Masato Yamamura, and Professor Tomohide Yabuki, for their insightful comments and encouragement, but also for the question which incited me to widen my research from various perspectives.

I thank my fellow labmates and the friends that I made during these four years. My doctoral course life would have been boring and terrible if I haven't had friends like Dejian Zhang, Xianghua Meng, Jianchen Bao, Yankun Yu, Mengqi Yu, Rehman Muhammad Mohib Ur, MOHD ZAINI Binti Farah Khaleda, Xiangrui Li. We worked together and spent lots of sleepless nights for the deadlines.

Last but not least, I would like to thank my family for encouraging and guiding me on the right path. Moreover, they always support me spiritually throughout writing this thesis and my life in Japan.

Wentao Chen

Kyushu Institute of Technology



# Appendix

## Journals:

1. W. Chen, G. Nagayama, Quasi-Casimir coupling induced phonon heat transfer across a vacuum gap, *Int. J. Heat Mass Transf.* 176 (2021) 121431.
2. W. Chen, G. Nagayama, Quasi-Casimir coupling can induce thermal resonance of adsorbed liquid layers in a nanogap, *Phys. Chem. Chem. Phys.* 24 (2022) 11758–11769.

## Proceedings:

1. W. Chen, G. Nagayama, Contribution of interfacial thermal resonance to phonon heat transfer across a sub-nanometer vacuum gap, 9th International Symposium on Applied Engineering and Sciences, 2021. (Oral presentation)
2. W. Chen, G. Nagayama, Interfacial thermal resonance assisted phonon heat transfer across vacuumed nanogap, International Joint Seminar on Mechanical Engineering 2021. (Oral presentation)
3. W. Chen, G. Nagayama, Non-equilibrium molecular dynamics simulation on thermal resonance in a nanogap, 2nd Asian Conference on Thermal Science, 2021. (Oral presentation)
4. W. Chen, G. Nagayama, Scale effects on thermal transport at solid-liquid interface, 8th International Symposium on Applied Engineering and Sciences, 2020. (Oral presentation)

5. W. Chen, G. Nagayama, A Molecular Dynamics Study on Thermal Transport at Nanostructured Solid-liquid Interface, International Joint Seminar on Mechanical Engineering 2020. (Oral presentation)
6. W. Chen, G. Nagayama, Thermal transport at nanostructured solid-liquid interface, Workshop on Thermal and Charge Transport across Flexible Nano-Interfaces, 2019. (Poster presentation)
7. W. Chen, G. Nagayama, Solid-like Liquid Layers at Nanostructured Surface: A Molecular Dynamic Simulation, International Joint Seminar on Mechanical Engineering 2019. (Poster presentation)
8. W. Chen, G. Nagayama, Molecular Dynamics Study on Solid-liquid Interfacial Boundary Condition in Nanoflow, International Joint Seminar on Thermal Engineering 2019. (Poster presentation)
9. W. Chen, G. Nagayama, Molecular Dynamics Study on Interfacial Heat and Mass Transfer at Nanostructured Surfaces, International Joint Seminar on Mechanical Engineering 2018. (Poster presentation)
10. W. Chen, G. Nagayama, Effects of Nanostructures on Solid-liquid Interfacial heat transfer, International Joint Seminar on Surface Functions Brought by Nano/microstructures 2018. (Poster presentation)

# Quasi-Casimir coupling induced phonon heat transfer across a vacuum gap

Wentao Chen<sup>a</sup>, Gyoko Nagayama<sup>b,\*</sup>

<sup>a</sup> Graduate School of Engineering, Kyushu Institute of Technology, 1-1 Sensui, Tobata, Kitakyushu, Fukuoka 804-8550, Japan

<sup>b</sup> Department of Mechanical Engineering, Kyushu Institute of Technology, 1-1 Sensui, Tobata, Kitakyushu, Fukuoka 804-8550, Japan

## Abstract

In vacuum, thermal energy is transported by photons (thermal radiation) but not phonons. Recent studies, however, indicated that phonon heat transfer across a vacuum gap is mediated by the quantum fluctuation of electromagnetic fields. Specifically, in the heat exchange between two objects separated by a nanoscale vacuum gap, phonons carry thermal energy more efficiently than photons. However, it remains unclear if phonons can propagate without electromagnetic fields. Here, we demonstrate that phonon transmission across a sub-nanometer vacuum gap can be induced by quasi-Casimir force subjected to the Lennard–Jones atoms using classical molecular dynamics simulation. The net heat flux across the vacuum gap increases exponentially as the gap distance decreases, owing to acoustic phonon transmission. The apparent local heat flux, evaluated using the Irving–Kirkwood method, increases singularly at the interfacial layers, while that at the inner layers agrees well with the net heat flux. These findings provide evidence of the strong thermal resonance induced by quasi-Casimir coupling between the interfacial layers. Thus, we conclude that the quasi-Casimir coupling induced by intermolecular interaction is a heat transfer mode for phonon heat transfer across a vacuum gap in nanoscale.

## 1. Introduction

Nanoscale heat transfer has been a challenging research topic since last decade [1–36]. The scale of the gap distance  $D$  dominates the heat transfer between two objects at different temperatures in vacuum, from the conventional heat conduction ( $D = 0$ ) to thermal radiation ( $D > \lambda_T$ , Wien's wavelength  $\lambda_T \cong 10^{-5}$  m at room temperature) [1]. As shown in Fig. 1, when the objects are separated by a gap of  $D < \lambda_T$ , known as the regime of the near-field radiative heat transfer (NFRHT), the amount of heat transfer can be several orders of magnitude greater than Planck's blackbody limit [2–7]. Therefore, the NFRHT has attracted considerable interest in advanced applications of thermal management [8,9], radiative cooling [10,11], nanogap near-field thermophotovoltaics [12], and heat-assisted magnetic recording [13,14].

The thermal energy transported by the coupling between the electromagnetic waves of the heating object and the phonons or plasmons of the cooling object in the regime of NFRHT, has been explored using the fluctuating electrodynamics theory [15] and experiments [16–18]. In the regime of  $D < 10^{-7}$  m, the atomic Coulomb interaction between two polar nanoparticles dominates the NFRHT in the gap distance of 8–100 nm [19], while the phonons serve as effective thermal carriers between two objects separated by a

nanometer vacuum gap [20–28]. In particular, phonon coupling in electric fields becomes significant in the transition regime from NFRHT to heat conduction. The existence of an extra tunnel for thermal energy transfer across a gap of 0–2.8 nm between two NaCl slabs was proposed due to phonon coupling induced by long-range Coulomb forces in the electric fields [29]. The acoustic phonons theoretically dominate the heat transfer across a gap of 1–5 nm between two Au surfaces applied a bias voltage of 0.6 V [30]. Furthermore, acoustic phonon transport has been experimentally observed in gaps ranging from 0–10 nm between a silicon tip and a platinum nano-heater under a bias voltage of 0.8 V [31]. However, clarifying the mechanism of the electric field assisted phonon transmission across a vacuum gap in this transition regime is still a challenging work.

On the other hand, Casimir heat transfer induced by resonance in electromagnetic fields was proposed in the transition regime from NFRHT to heat conduction. The Casimir force was first introduced in 1948 as a force acting between neutral objects based on quantum fluctuations of electromagnetic fields [32]. A local model of the dielectric function was applied to explain the phonon coupling mechanism induced by the Casimir force across a vacuum gap of  $D < 10$  nm between two dielectric solids [33]. The quantum fluctuation has been found to resonantly enhance the heat exchange between two Si<sub>3</sub>N<sub>4</sub> membranes at  $D < 400$  nm in an electromagnetic field [34].

However, the phonon heat transfer due to the thermal resonance induced by quasi-Casimir coupling has never been verified without an electromagnetic field. To this end, in this study, a quasi-Casimir coupling model is proposed for phonon heat transfer between two parallel solid walls separated by a sub-nanometer vacuum gap in the absence of an electromagnetic field. The phonon heat transfer is investigated in systems by performing a classical molecular dynamics (MD) simulation to verify the quasi-Casimir coupling model. Consequently, we evidence the phonon heat transfer induced by the intermolecular interactive force across the vacuum gap with significant interfacial resonance.

## 2. Models and simulation method

### 2.1. Physical model

Consider two solid walls that consist of monoatomic molecules connected by springs, which correspond to the harmonic potential at heating and cooling walls, as illustrated in Fig. 2(a). The two solid walls are bonded with a quasi-Casimir coupling characterized by the spring coupling in a vacuum gap. This quasi-Casimir coupling acts as the channel for phonon transmission in the vacuum gap, which is

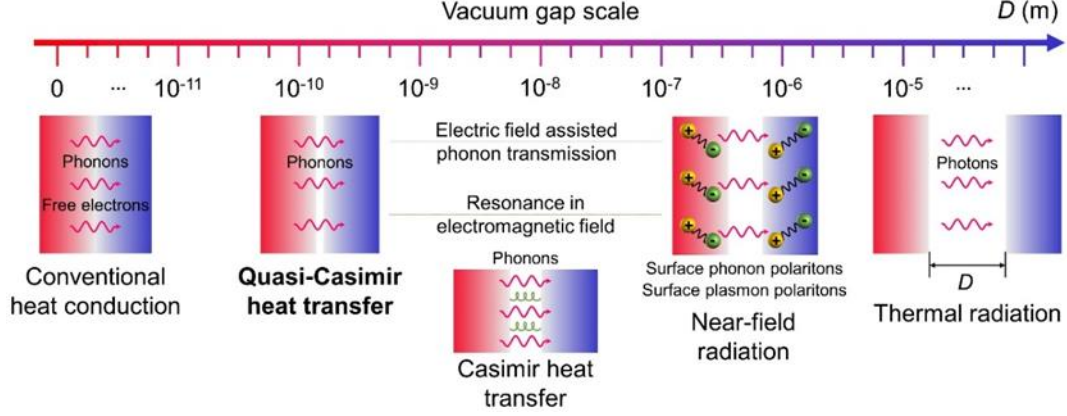


**Fig. 1.** Scale of a vacuum gap dominates the heat transfer mechanism between two objects.

similar to acoustic phonon tunneling in an evanescent electric field, thus providing an additional channel to enhance thermal energy transfer across the vacuum gap [29]. A constant heat flux  $q$  passes through the vacuum gap with thermal conductance  $G$  from the interfacial layer of the heating wall at a high temperature  $T_{\text{Hi}}$  to that of the cooling wall at a low temperature  $T_{\text{Ci}}$ .

## 2.2. MD simulation method

The MD technique [37–40] was applied to simulate thermal energy transport across the sub-nanometer vacuum gap between the heating wall (red wall heated by a thermostat layer of 120–300 K) and the cooling wall (blue wall cooled by a thermostat layer of 100 K). The velocity scaling method was used to maintain the temperatures of the heating and cooling thermostats [41]. The two parallel solid walls were separated by a gap distance  $D$  of 0–0.784 nm (0– $2a$ ), where  $a$  denotes the lattice constant of platinum and is equivalent to 0.392 nm [42], as shown in Fig. 2(b). As  $D$  decreases, the strength of the intermolecular interactions between two solid walls in vacuum increases, which induces the quasi-Casimir coupling with high thermal energy transport, as will be described in Section 3.

The dimensions of the simulation cell are  $L_x = 5.552$  nm,  $L_y = 3.847$  nm, and  $L_z = 1.813$ – $2.597$  nm. Each solid wall consists of four

layers of atoms that are settled as  $\langle 111 \rangle$ -oriented face-centered cubic lattices. The solid walls are presumed to be composed of 2,560 platinum atoms. Periodic boundary conditions are employed along the  $x$ - and  $y$ -directions. The solid–solid interaction is expressed by the Lennard–Jones potential as follows:

$$\phi(r_{ij}) = 4\epsilon \left[ \left( \frac{\sigma}{r_{ij}} \right)^{12} - \left( \frac{\sigma}{r_{ij}} \right)^6 \right], \quad (1)$$

where the length parameter  $\sigma = 2.475$  Å and the energy parameter  $\epsilon = 8.35 \times 10^{-20}$  J for the potential well depth of Pt–Pt to model the atomic vibration at the lattice. All of the simulations are implemented with a time step of 5 fs and a cut-off radius of  $5\sigma$  selected for the spherically truncated and shifted potential. The equations of motion are integrated using the velocity Verlet algorithm.

The equilibrium system at 100 K is simulated after achieving a steady state from the initial state for 5 ns. Subsequently, the non-equilibrium molecular dynamics (NEMD) simulation is performed from the equilibrium state to the steady state for 50 ns. In all of the NEMD simulations, the cumulative input and output energies  $E_{\text{H}}$  and  $E_{\text{C}}$  in the heating (120–300 K) and cooling (100 K) thermostats, respectively, are monitored. After the system achieves a steady state with constant heat flow ( $\Delta E \approx 0$ ), an extra un-steady NEMD simulation is conducted by switching off the cooling thermostat but

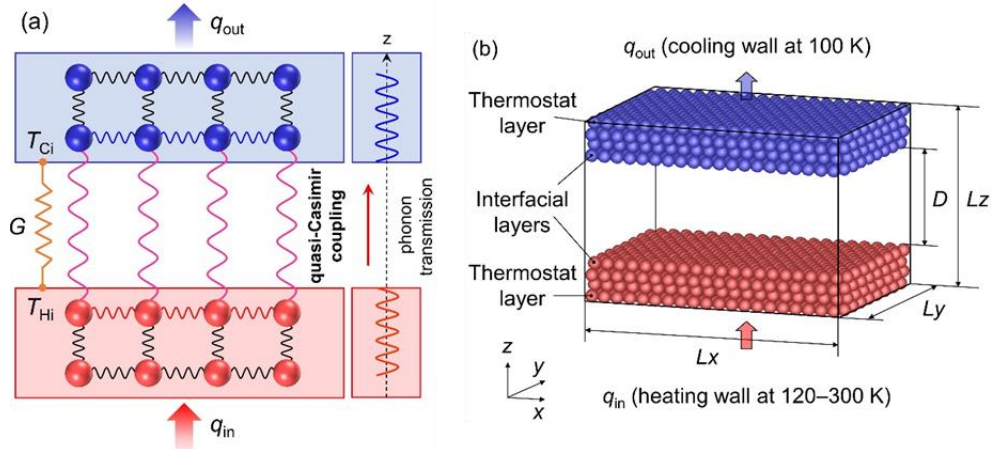


**Fig. 2.** (a) Schematic of acoustic phonon transmission across a vacuum gap by quasi-Casimir coupling. (b) MD simulation system: heat exchange between two parallel solid walls separated by a gap distance  $D$ .

operating the heating thermostat for 5 ns. The transient thermal behaviors are discussed in Section 3.1. Further data analyses for the steady NEMD simulations are described in the next section.

### 2.3. Computational details

The simulation system is divided into eight bins along both the x- and z-directions to obtain the temperature profile in the steady state for 5 ns. The local temperature  $T$  of each bin can be calculated as follows:

$$T = \frac{1}{N} \sum_{n=1}^N \frac{2}{3k_B} \sum_{i=1}^3 \frac{1}{2} m (v_{n,i} - \bar{v}_i)^2, \quad (2)$$

where  $N$  is the particle number in the bin,  $k_B$  is the Boltzmann constant,  $m$  is the mass of the solid atom,  $v_{n,i}$  is the velocity of atom  $n$  in the  $i$  (=x, y, z) direction, and  $\bar{v}_i$  is the mean velocity of the solid atoms in the bin.

The heat flux passing through the system is acquired from the mean value over the last 15 ns within a 50 ns time window. The heat flux is

$$q = \frac{1}{A} \cdot \frac{\partial E}{\partial t}, \quad (3)$$

where  $A$  is the cross-sectional area of the xy-plane,  $\partial E / \partial t$  is the rate of heat transfer in the heating or cooling thermostat, and  $E$  is the cumulative energy of the heating ( $E_H$ ) or cooling ( $E_C$ ) thermostat. The thermal conductance between the two solid walls is calculated as

$$G = \frac{q}{T_{Ht} - T_{Ct}}. \quad (4)$$

The atomic vibrational displacements and frequencies are measured using a wave graph to observe the vibrational properties of the atoms at the positions (A2, A3, A4 and B2, B3, B4) shown in Fig. 3. The wave graphs are obtained by outputting the positions of the atoms from the MD simulation data of 10,000 time steps and conducting signal processing [43]. The equilibrium position of the atoms in the z-direction is calculated by:

$$\bar{z} = \frac{1}{t_f - t_0} \sum_{t_0}^{t_f} z_{i,t}, \quad (5)$$

where  $z_{i,t}$  is the position of atom  $i$  at time  $t$ , and atom  $i$  is located at the center of each solid layer;  $t_0$  is the initial time at which the data output begins, and  $t_f$  is the long finite time for 10,000 time steps. The original vibrational displacements of atom  $i$  are calculated as  $\Delta z_{i,t} = z_{i,t} - \bar{z}$ . Then, we calculate the Fourier transform of the original vibrational displacements to obtain the distribution of signal power in the frequency domain (power spectrum). The dominant frequency band is selected to perform signal filtering on the original vibrational displacements and obtain the regular wave graphs. The peak amplitude and frequency are determined from the wave graphs.

The velocities of all the atoms in the interfacial layers obtained from the MD simulation data of 10,000 time steps, are used to calculate the vibrational density of states (VDOS) [44,45] of the interfacial layers by the Fourier transform of the velocity autocorrelation function

$$VDOS(\omega) = \int_0^\infty \langle \vec{v}(t) \vec{v}(0) \rangle e^{-i\omega t} dt. \quad (6)$$

Here,  $\omega$  is the angular frequency, and  $v(t)$  is the atomic velocity at time  $t$ .

The simulation system is divided into eight bins along both the x- and z-directions to calculate the average local heat flux by Irving–Kirkwood (I–K) method of each layer. The components of thermal energy are calculated to estimate the effective energy of heat transfer across a vacuum gap along the z-direction by using the I–K equation [46, 47],

$$J_q = J_k + J_p + J_i = \frac{1}{V} \sum_i E_i^k v_{z,i} + \frac{1}{V} \sum_i \phi_i v_{z,i} + \frac{1}{2V} \sum_i \sum_j (F_{ij} v_j) r_{z,ij}, \quad (7)$$

where  $J_k$  and  $J_p$  represent the energies transported by the molecules with kinetic and potential energy, respectively, and  $J_i$  represents the intermolecular energy transfer.  $V$  is the volume of the solid layer,  $E_i^k$  is the kinetic energy of molecule  $i$ ,  $\phi_i$  is the potential energy of molecule  $i$ ,  $v_{z,i}$  is the velocity component of molecule  $i$  along the z-direction,  $F_{ij}$  is the intermolecular force between molecules  $i$  and  $j$ ,  $v_j$  is the velocity of molecule  $j$ , and  $r_{z,ij}$  is the distance between molecules  $i$  and  $j$  along the z-direction.

### 3. Results and discussion

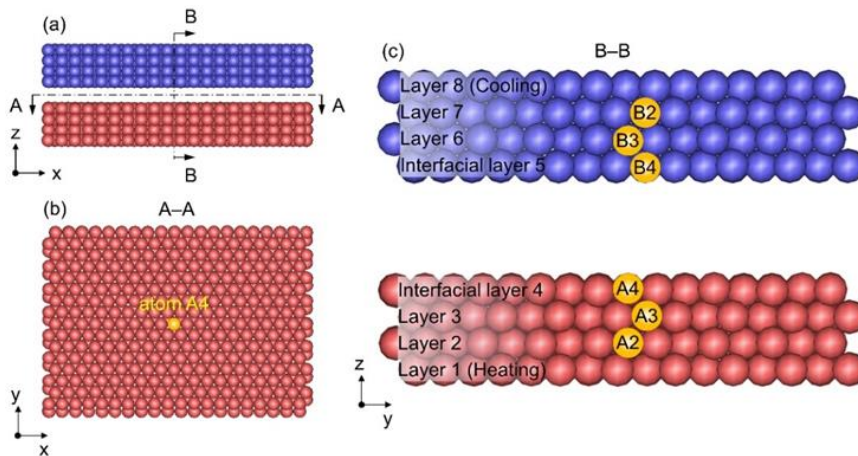


**Fig. 3.** Positions of atoms selected to analyze the atomic vibrational characteristics from different views of the simulation model: (a) front view of the simulation model in the xz-direction; (b) atom A4 at interfacial layer 4 in the A–A directional view of the simulation model; (c) atoms A2, A3, A4 and B2, B3, B4 of the solid layers in the B–B directional enlarged view of the simulation model.

### 3.1. Transient thermal behavior in non-steady state

Since the temperature differences between the heating and cooling walls in the steady NEMD simulations can be maintained if the vacuum gap acts as the thermal insulation, we conducted the non-steady NEMD simulations to confirm if thermal energy can be transported from the heating wall to the cooling wall across the vacuum gap. The transient thermal behavior of the system is investigated based on the time history of the temperatures at the interfacial layers. The temperatures shown in Fig. 4 are obtained in the non-steady NEMD simulations by operating the heating thermostat but switching off the cooling thermostat. The temperature difference between the interfacial layers of the heating and cooling walls separated by  $D = 0.5a$  is eliminated after a certain period of time within 5 ns, thus demonstrating the occurrence of thermalization between the two solid walls. This phenomenon indicates that energy must be transferred from the heating wall to the cooling wall across a

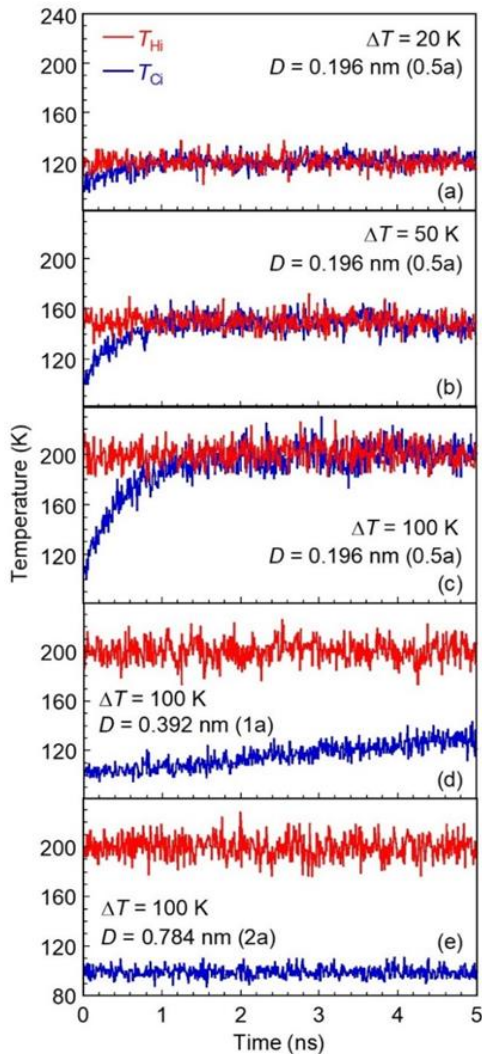


**Fig. 4.** Thermal energy transport across a vacuum gap in non-steady NEMD simulations: (a–c) effects of  $\Delta T$  on the transient temperature of the interfacial layers at constant  $D = 0.5a$ ; (c–e) effects of  $D$  on the transient temperature of the interfacial layers at constant  $\Delta T = 100$  K.

vacuum gap, even for the Lennard–Jones atoms, in the absence of an electromagnetic field. The heat transfer between the two walls is enhanced with an increment in the temperature difference between thermostats  $\Delta T$  at  $D = 0.5a$ , as shown in Figs. 4(a)–(c); while diminishes with an increase in  $D$  at  $\Delta T = 100$  K as shown in Figs. 4(c)–(e), owing to the weakened interaction between the two interfacial layers.

### 3.2. Temperature profiles in steady state

The temperature profiles shown in Fig. 5 are obtained under the operation of the simultaneous heating and cooling thermostats after the NEMD system achieves a steady state, where the solid lines are guide for the eye. Figs. 5(a)–(e) are results under the constant temperature difference between the two thermostats ( $\Delta T = 20$  K). In the case of  $D = 0$ , as shown in Fig. 5(a), a continuum temperature distribution is obtained from the cooling thermostat to the thermostat free layers, while a temperature jump is found between the heating thermostat and the neighboring thermostat free layer. This temperature jump is caused by the phonon mismatch between the thermostat and thermostat free layer owing to the dynamic rescaling of the thermostat [48,49]. Increasing  $D$  from  $0.5a$  to  $2a$  ( $\Delta T = 20$  K), as shown in Figs. 5(b)–(e), the temperature distributes continuously in the inner layers, while discontinuously at the interfacial layers. The temperature jump at the interfacial layers ( $T_{Hi} - T_{Ci}$ ) is nearly identical to  $\Delta T$  and independent of the gap distance  $D$ . In the case of  $D = 0.5a$ , as shown in Fig. 5(f), the temperature gradient of heating wall is nearly same as that of cooling wall, and  $T_{Hi} - T_{Ci}$  gets larger with an increment in  $\Delta T$ , showing the enhanced thermal energy exchange between the two solid walls.

### 3.3. Net heat flux and thermal conductance

In the steady state of the NEMD simulation, the net heat flux and thermal conductance are obtained by conducting data sampling over a period of 15 ns. The net heat flux and thermal conductance in the sub-nanometer gap are approximately three to six orders of magnitude larger than that of blackbody radiation as a function of  $D$ , as shown in Figs. 6(a) and (b). These results give evidence of the existence of another heat transfer mode between the regimes of thermal radiation and heat conduction. This exponential heat transfer enhancement occurs owing to the strengthened intermolecular interaction between the two solid walls as  $D$  decreases. The heat flux and thermal conductance in the case of  $D = 0$  are larger than those for other cases of  $D$  due to the heat conduction in solid objects. Furthermore, the heat flux enhances with an increment in  $\Delta T$ , while  $\Delta T$  does not notably influence the thermal conductance, as shown in Figs. 6(c) and (d).

### 3.4. Thermal resonance induced by quasi-Casimir coupling

To understand the mechanism of heat transfer enhancement with decreasing  $D$ , as shown in Fig. 6, we analyzed the atomic vibrational characteristics in a steady NEMD state under a constant  $\Delta T$  of 20 K. For  $D = 0.5a$ , the peak amplitudes of the interfacial atoms (A4 at the heating wall, B4 at the cooling wall) are significantly larger than those of the atoms (A2, A3, B2, B3) in the inner layers, as shown in Figs. 7

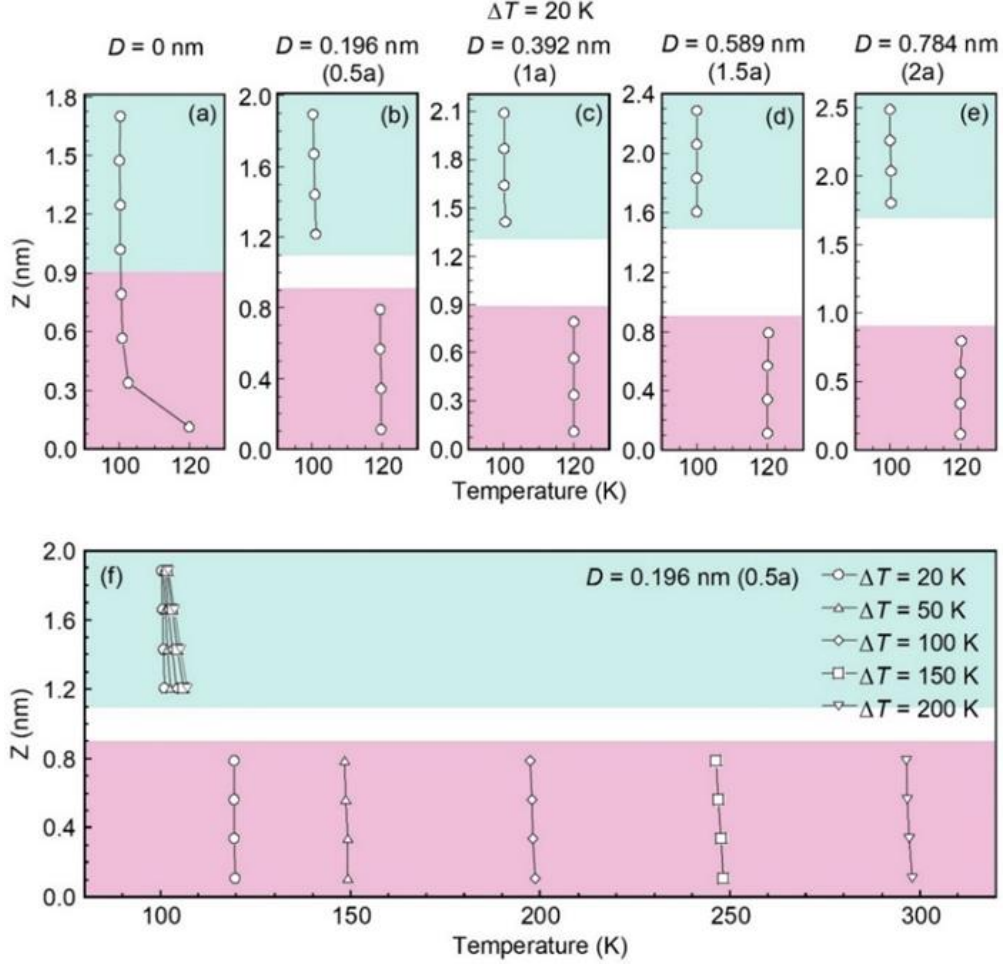


**Fig. 5.** Temperature profiles of the solid walls in steady NEMD simulations: (a–e) varying  $D$  at constant  $\Delta T = 20$  K; (f) varying  $\Delta T$  at constant  $D = 0.196$  nm (0.5a).

(b) and (e) and summarized in Table 1. Meanwhile, the vibrational frequencies of the interfacial atoms (A4, B4) are smaller than those of the inner layer atoms, as listed in Table 1. These deviations are unremarkable when  $D = 2a$ , as shown in Figs. 7(c) and (f), while the peak amplitudes and frequencies of the inner layer atoms at  $D = 0$  are similar, as shown in Figs. 7(a) and (d). That is, when  $D$  is sufficiently small (several atomic diameters), the interfacial atoms are subjected to strong molecular interactions across the vacuum gap, which results in the thermal resonance induced by quasi-Casimir coupling. This aspect can be proved by the perfectly overlapped vibrational displacements of the interfacial atoms A4 and B4 separated by the vacuum gap in Figs. 8(b) and (c), which show vibration behaviors similar to those of the inner layer atoms in the solid wall shown in Fig. 8(a). Therefore, the VDOSs based on the Fourier transform of the atomic velocity autocorrelation function [44,45] of solid layer 4 are consistent with those of layer 5, as shown in Figs. 8(d)–(f). Compared to the peaks of the VDOSs of the inner layers in the solid ( $D = 0$ ), those of the interfacial layers ( $D = 0.5a$  or  $2a$ ) are shifted toward the left of the low-frequency band. That is, the heat transfer across the sub-nanometer vacuum gap between the solid walls exhibits a trend similar to that of the solid walls without a gap, conducted through the acoustic phonons in the low-frequency band of 3–4 THz. The strong phonon coupling at the interfacial layers leads to the resonant

excitation peaks of the VDOSs in the frequency band coinciding with the vibrational frequencies of the interfacial atoms A4 and B4, as summarized in Table 1. These results indicate that the gap distance  $D$  is the dominant factor governing the near-field heat transfer induced by the quasi-Casimir coupling.

**Table 1**

Effects of  $D$  on the peak amplitudes and frequencies of atoms in the interfacial and inner layers at constant  $\Delta T = 20$  K.

Cases $D$ (nm)	A2	B2	A3	B3	A4	B4
Peak amplitude (pm)						
0	1.909	1.244	1.722	1.246	1.471	1.468
0.196	1.646	1.583	1.570	1.559	2.775	2.526
0.784	1.733	1.302	1.335	1.235	1.734	1.693
Frequency $f$ (THz)						
0	4.041	3.699	3.790	3.701	3.736	3.727
0.196	4.578	4.452	4.207	4.207	3.277	3.257
0.784	4.483	4.359	4.017	3.949	3.180	3.149

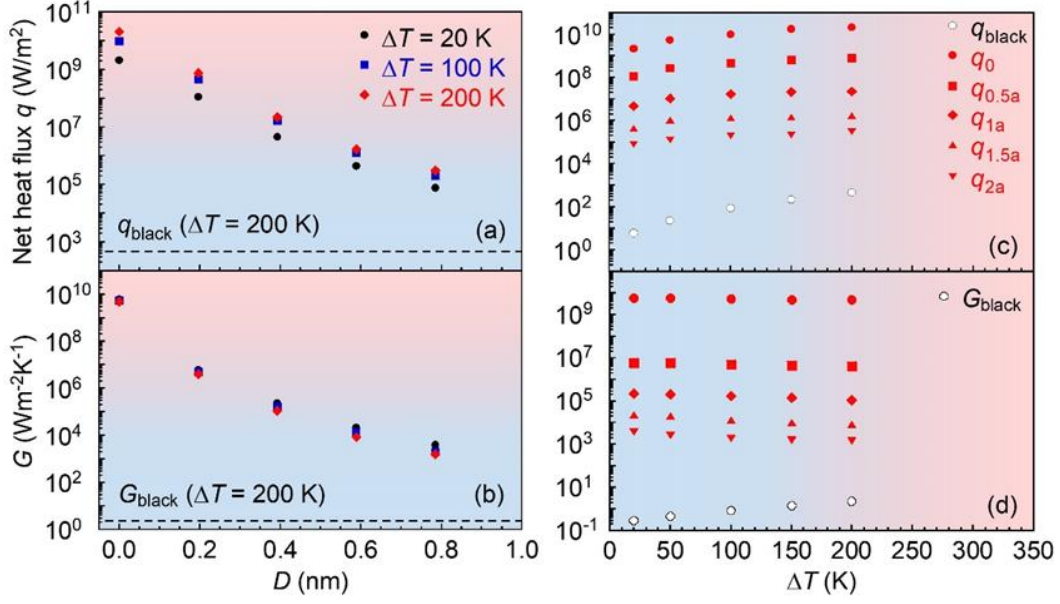


**Fig. 6.** Effects of  $D$  on (a) net heat flux and (b) thermal conductance. Effects of  $\Delta T$  on (c) net heat flux and (d) thermal conductance.

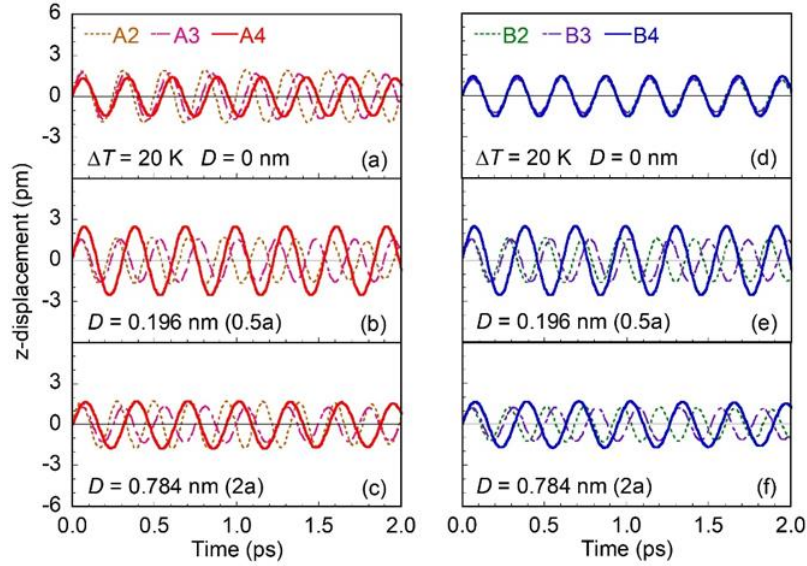


**Fig. 7.** Effects of  $D$  on atomic vibrational displacements of layers in the heating and cooling walls at constant  $\Delta T = 20$  K: (a–c) vibrational displacements of atoms A2, A3, and A4 in the heating wall; (d–f) vibrational displacements of atoms B2, B3, and B4 in the cooling wall.

### 3.5. Local heat flux by Irving–Kirkwood method

For the estimation of the local thermal properties in the heat exchange between two solid walls from an atomic perspective, a stable local heat flux distribution is established through data sampling for more than 50 ns by using the I-K method [46,47], as shown in Fig. 9. The blue dashed lines represent the net heat flux of the system obtained from the energy balance of the two thermostats, the open circles are the local heat flux of each layer, and the black solid lines are guide for the eye. The component contributions of the heat transfer enhancement induced by the quasi-Casimir coupling are analyzed, as shown in Fig. 10. The local heat flux  $J_q$  of each solid layer is

composed of four components, namely  $J_k$ ,  $J_p$ ,  $J_{is}$ , and  $J_{io}$  corresponding to the kinetic energy, potential energy, self-wall molecular interaction, and other wall molecular interaction, respectively.

When  $D = 0$ ,  $J_q$  is distributed uniformly and gets larger as  $\Delta T$  increases, as shown in Figs. 9(a)–(e).  $J_q$  satisfies the energy conservation law, which is equivalent to the net heat flux  $q$  obtained from the energy balance of the two thermostats. Clearly, the local heat flux components  $J_{is}$  and  $J_{io}$  dominate the thermal energy transport in the solid, and  $J_k$  and  $J_p$  are negligible, as shown in Figs. 10(a)–(c). Here,  $J_{is}$  and  $J_{io}$  contribute equally at inner layers 4 and 5. When  $D = 0.5a$  (i.e., interfacial quasi-Casimir coupling), the apparent local heat flux increases singularly at the interfacial layers, whereas it is

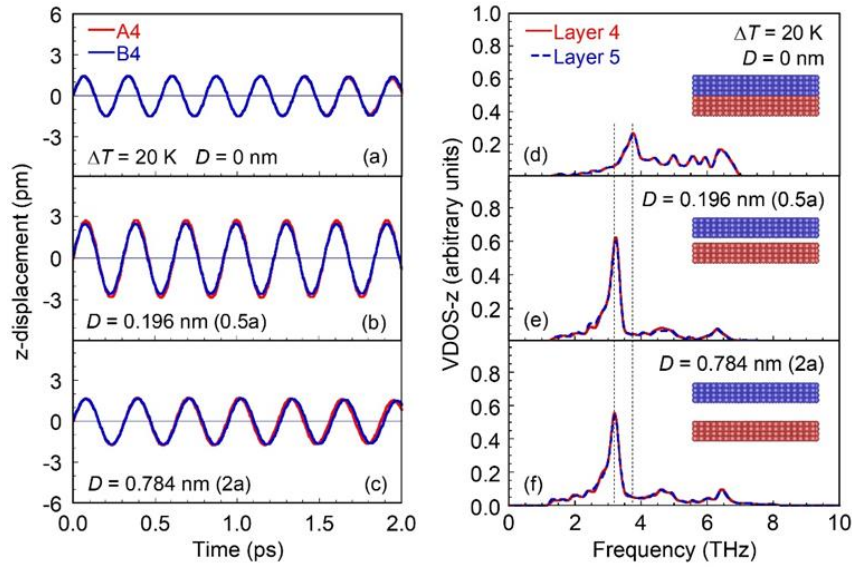


**Fig. 8.** Effects of  $D$  on (a–c) the vibrational displacements of atoms A4 and B4 in the interfacial layers as well as (d–f) the VDOSs of layers 4 and 5.

distributed uniformly at the inner layers, corresponding to  $q$ , as shown in Figs. 9(f)–(j). The apparent local heat flux at the interfacial layers enhances singularly, accompanied by considerable thermal resonance induced by quasi-Casimir coupling (see Figs. 7(b) and (e)). In Fig. 10(d)–(f), the singular increments of the apparent local heat flux at the interfacial layers are contributed to the increments of  $J_{io}$  (orange) and  $J_p$  (blue). Although  $J_{is}$  (green) is almost same to the half of  $q$ ,  $J_{io}$  exceeds the half of  $q$ , owing to the thermal resonance induced by the quasi-Casimir coupling. Additionally, the interfacial vibration energy increases under the thermal resonance, resulting in the increment of  $J_p$  at the interface. In other words, the singular increments of the apparent local heat flux at the interfacial layers can be regarded as the evidence of the quasi-Casimir coupling.

#### 4. Conclusion

MD simulations were performed to investigate the phonon heat transfer across a vacuum gap induced by the quasi-Casimir force subjected to the Lennard–Jones atoms. We demonstrated that the heat exchange between two solid walls separated by a sub-nanometer vacuum gap increases exponentially as the gap distance decreases, following the law of energy conservation. The heat transfer enhancement is caused by the acoustic phonon transport across a vacuum gap, as a result of the strong thermal resonance induced by the quasi-Casimir coupling. This aspect is explained by the perfect overlap of the atomic vibrational displacements and VDOSs of the interfacial layers. Moreover, the apparent local heat flux, evaluated using the I–K method, increases singularly at the interfacial layers, while that at the inner layers is consistent with the net heat flux. This finding provides evidence of the strong thermal resonance at the two interfacial layers, induced by quasi-Casimir coupling.

The phonon transport across a vacuum gap induced by quasi-Casimir coupling, is a phenomenon independent of electrostatic interaction, electron cloud overlap, surface phonon polaritons and surface plasmon polaritons. This phenomenon is noticeably distinct from conventional heat conduction and thermal radiation, or the known NFRHT and Casimir heat transfer. The proposed quasi-

Casimir coupling model of heat transfer provides fundamental insights into nanoscale energy transport between the regimes of NFRHT and heat conduction.

#### Declaration of Competing Interest

The authors declare that they have no known competing financial interests or personal relationships that could have appeared to influence the work reported in this paper.

#### CRediT authorship contribution statement

**Wentao Chen:** Investigation, Methodology, Data curation, Formal analysis, Writing - original draft. **Gyoko Nagayama:** Conceptualization, Methodology, Supervision, Writing - review & editing, Funding acquisition.

#### Acknowledgments

This work was supported by the Ministry of Education, Science and Culture of the Japanese Government through the Grant-in Aid for Scientific Research, Project No. 18H01385, the research supercomputing services by the Research Institute for Information Technology, Kyushu University, and the Initiative for Realizing Diversity in the Research Environment by Ministry of Education, Culture, Sports, Science and Technology, Japan.

#### References

- [1] A.I. Volokitin, Contribution of the acoustic waves to near-field heat transfer, *J. Phys. Condens. Matter.* 32 (2020) 215001.
- [2] M. Nomura, Near-field radiative heat transfer: The heat through the gap, *Nat. Nanotechnol.* 11 (2016) 496–497.
- [3] B. Song, Y. Ganjeh, S. Sadat, D. Thompson, A. Fiorino, V. Fernández-Hurtado, J. Feist, F.J. Garcia-Vidal, J.C. Cuevas, P. Reddy, E. Meyhofer, Enhancement of near-field radiative heat transfer using polar dielectric thin films, *Nat. Nanotechnol.* 10 (2015) 253–258.

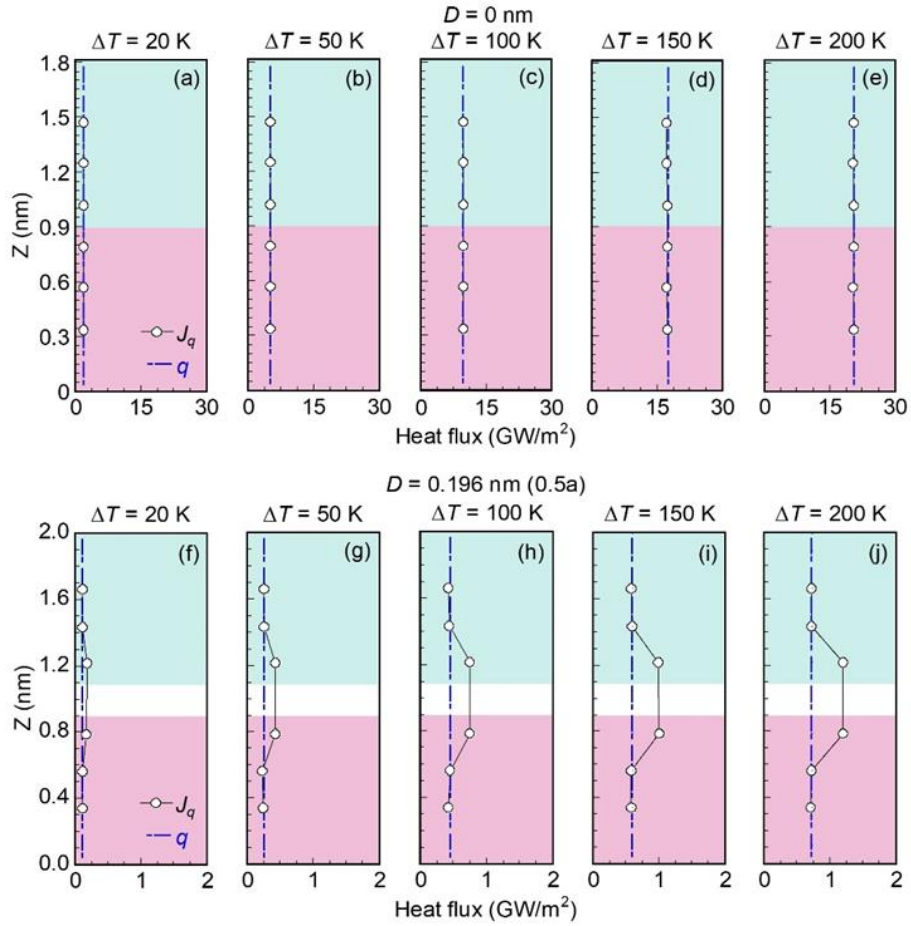


**Fig. 9.** Effects of  $\Delta T$  on the local heat flux by I-K method of the interfacial and inner layers along the  $z$ -direction at (a–e)  $D = 0$  and (f–j)  $D = 0.5a$ .

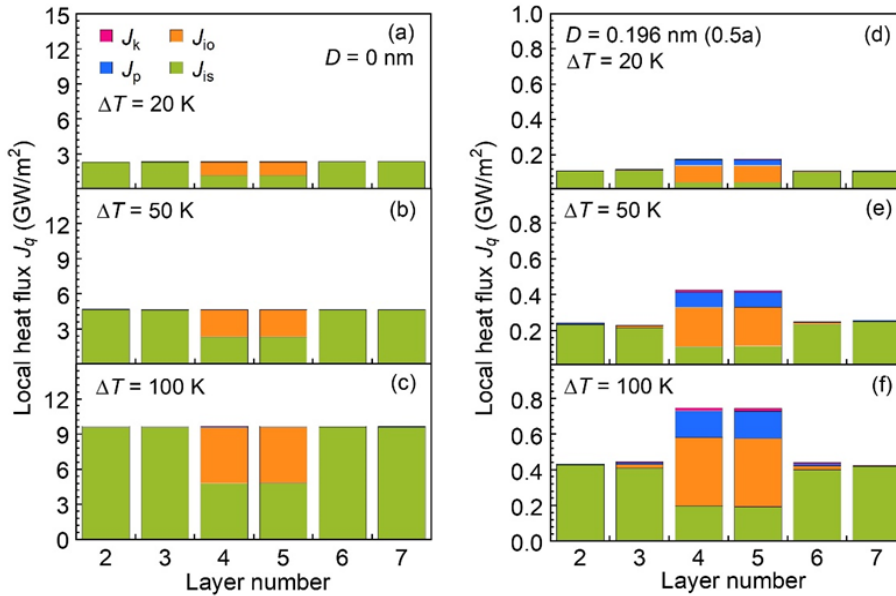


**Fig. 10.** Effects of  $\Delta T$  on the contributions of the thermal energy components to the local heat flux by I-K method at the interfacial and inner layers at (a–c)  $D = 0$  and (d–f)  $D = 0.5a$ .

- [5] K. Kim, B. Song, V. Fernández-Hurtado, W. Lee, W. Jeong, L. Cui, D. Thompson, J. Feist, M.T.H. Reid, F.J. García-Vidal, J.C. Cuevas, E. Meyhofer, P. Reddy, Radiative heat transfer in the extreme near field, *Nature* 528 (2015) 387–391.
- [6] M.P. Bernardi, D. Milovich, M. Francoeur, Radiative heat transfer exceeding the blackbody limit between macroscale planar surfaces separated by a nanosize vacuum gap, *Nat. Commun.* 7 (2016) 1–7.
- [7] A. Fiorino, D. Thompson, L. Zhu, B. Song, P. Reddy, E. Meyhofer, Giant Enhancement in Radiative Heat Transfer in Sub-30 nm Gaps of Plane Parallel Surfaces, *Nano Lett.* 18 (2018) 3711–3715.
- [8] A. Fiorino, D. Thompson, L. Zhu, R. Mittapally, S.A. Biehs, O. Bezenecet, N. El-Bondry, S. Bansropun, P. Ben-Abdallah, E. Meyhofer, P. Reddy, A Thermal Diode Based on Nanoscale Thermal Radiation, *ACS Nano* 12 (2018) 5174–5179.
- [9] L. Zhu, A. Fiorino, D. Thompson, R. Mittapally, E. Meyhofer, P. Reddy, Near-field photonic cooling through control of the chemical potential of photons, *Nature*. 566 (2019) 239–244.
- [10] B. Guha, C. Otey, C.B. Poitras, S. Fan, M. Lipson, Near-field radiative cooling of nanostructures, *Nano Lett.* 12 (2012) 4546–4550.
- [11] J. Cho, K.E. Goodson, Thermal transport: Cool electronics, *Nat. Mater.* 14 (2015) 136–137.
- [12] A. Fiorino, L. Zhu, D. Thompson, R. Mittapally, P. Reddy, E. Meyhofer, Nanogap near-field thermophotovoltaics, *Nat. Nanotechnol.* 13 (2018) 806–811.
- [13] H. Li, B. Liu, T.C. Chong, Thermal study of nanometer-spaced head-disk systems, *Jpn. J. Appl. Phys.* 44 (2005) 7445–7447.
- [14] E. Albisetti, D. Petti, M. Pancaldi, M. Madami, S. Tacchi, J. Curtis, W.P. King, A. Papp, G. Csaba, W. Porod, Nanopatterning reconfigurable magnetic landscapes via thermally assisted scanning probe lithography, *Nat. Nanotechnol.* 11 (2016) 545–551.
- [15] B. V. Budaev, D.B. Bogy, Computation of radiative heat transport across a nanoscale vacuum gap, *Appl. Phys. Lett.* 104 (2014) 061109.
- [16] L. Tranchant, S. Hamamura, J. Ordonez-Miranda, T. Yabuki, A. Vega-Flick, F. Cervantes-Alvarez, J.J. Alvarado-Gil, S. Volz, K. Miyazaki, Two-Dimensional Phonon Polariton Heat Transport, *Nano Lett.* 19 (2019) 6924–6930.
- [17] S. Shen, A. Narayanaswamy, G. Chen, Surface phonon polaritons mediated energy transfer between nanoscale gaps, *Nano Lett.* 9 (2009) 2909–2913.
- [18] K. Kloppstech, N. Könné, S.A. Biehs, A.W. Rodriguez, L. Worbes, D. Hellmann, A. Kittel, Giant heat transfer in the crossover regime between conduction and radiation, *Nat. Commun.* 8 (2017) 14475.
- [19] G. Domingues, S. Volz, K. Joulain, J.J. Greffet, Heat transfer between two nanoparticles through near field interaction, *Phys. Rev. Lett.* 94 (2005) 085901.
- [20] I. Altfeder, A.A. Voevodin, A.K. Roy, Vacuum phonon tunneling, *Phys. Rev. Lett.* 105 (2010) 166101.
- [21] C. Yang, X. Wei, J. Sheng, H. Wu, Phonon heat transport in cavity-mediated optomechanical nanoresonators, *Nat. Commun.* 11 (2020) 1–6.
- [22] M. Prunnila, J. Meltaus, Acoustic phonon tunneling and heat transport due to evanescent electric fields, *Phys. Rev. Lett.* 105 (2010) 125501.
- [23] J.B. Pendry, K. Sasihithlu, R. V. Craster, Phonon-assisted heat transfer between vacuum-separated surfaces, *Phys. Rev. B* 94 (2016) 075414.
- [24] B. V. Budaev, D.B. Bogy, On the role of acoustic waves (phonons) in equilibrium heat exchange across a vacuum gap, *Appl. Phys. Lett.* 99 (2011) 053109.
- [25] A. Alkurdi, C. Adessi, F. Tabatabaie, S. Li, K. Termentzidis, S. Merabia, Thermal transport across nanometre gaps: Phonon transmission vs. air conduction, *Int. J. Heat Mass Transf.* 158 (2020) 119963.
- [26] D.P. Sellan, E.S. Landry, K. Sasihithlu, A. Narayanaswamy, A.J.H. McGaughey, C.H. Amon, Phonon transport across a vacuum gap, *Phys. Rev. B.* 85 (2012) 024118.
- [27] A.I. Volokitin, Effect of an Electric Field in the Heat Transfer between Metals in the Extreme Near Field, *JETP Lett.* 109 (2019) 749–754.
- [28] S. Xiong, K. Yang, Y.A. Kosevich, Y. Chalopin, R. D’Agosta, P. Cortona, S. Volz, Classical to Quantum Transition of Heat Transfer between Two Silica Clusters, *Phys. Rev. Lett.* 112 (2014) 114301.
- [29] V. Chiloyan, J. Garg, K. Esfarjani, G. Chen, Transition from near-field thermal radiation to phonon heat conduction at sub-nanometre gaps, *Nat. Commun.* 6 (2015) 6755.
- [30] T. Tokunaga, A. Jarzembki, T. Shiga, K. Park, M. Francoeur, Extreme Near-Field Heat Transfer Between Gold Surfaces, arXiv: 2102.04575.
- [31] A. Jarzembki, T. Tokunaga, J. Crossley, J. Yun, C. Shaskey, R.A. Murdick, I. Park, M. Francoeur, K. Park, Force-induced acoustic phonon transport across single-digit nanometre vacuum gaps, arXiv: 1904.09383.
- [32] H.B.G. Casimir, On the attraction between two perfectly conducting plates, *Proc. K. Ned. Akad.* 51 (1948) 793–795.
- [33] Y. Ezzahri, K. Joulain, Vacuum-induced phonon transfer between two solid dielectric materials: Illustrating the case of Casimir force coupling, *Phys. Rev. B* 90 (2014) 115433.
- [34] K.Y. Fong, H.-K. Li, R. Zhao, S. Yang, Y. Wang, X. Zhang, Phonon heat transfer across a vacuum through quantum fluctuations, *Nature* 576 (2019) 243–247.
- [35] M. Morita, T. Shiga, Surface phonons limit heat conduction in ultra-thin films, arXiv: 2008.11078.
- [36] R. Anufriev, A. Ramiere, J. Maire, M. Nomura, Heat guiding and focusing using ballistic phonon transport in phononic nanostructures, *Nat. Commun.* 8 (2017) 15505.
- [37] G. Nagayama, P. Cheng, Effects of interface wettability on microscale flow by molecular dynamics simulation, *Int. J. Heat Mass Transf.* 47 (2004) 501–513.
- [38] G. Nagayama, M. Kawagoe, A. Tokunaga, T. Tsuruta, On the evaporation rate of ultra-thin liquid film at the nanostructured surface: A molecular dynamics study, *Int. J. Therm. Sci.* 49 (2010) 59–66.
- [39] G. Nagayama, T. Tsuruta, P. Cheng, Molecular dynamics simulation on bubble formation in a nanochannel, *Int. J. Heat Mass Transf.* 49 (2006) 4437–4443.

- [40] H. Matsubara, G. Kikugawa, T. Ohara, Comparison of molecular heat transfer mechanisms between water and ammonia in the liquid states, *Int. J. Therm. Sci.* 161 (2021) 106762.
- [41] R.J. Sadus, *Molecular Simulation of Fluids*, first ed., Elsevier, Netherlands, 1999, pp. 305–307.
- [42] J.W. Arblaster, Crystallographic properties of platinum, *Platin. Met. Rev.* 41 (1997) 12–21.
- [43] A.V. Oppenheim, G.C. Verghese, *Signals, Systems and Interference*, first ed., Pearson, Boston, 2016, pp. 5–28.
- [44] H. Bao, J. Chen, X. Gu, B. Cao, A review of Simulation Methods in Micro/Nanoscale Heat Conduction, *ES Energy Environ.* 1 (2018) 16–55.
- [45] X. Liu, D. Surblys, Y. Kawagoe, A.R. Bin Saleman, H. Matsubara, G. Kikugawa, T. Ohara, A molecular dynamics study of thermal boundary resistance over solid interfaces with an extremely thin liquid film, *Int. J. Heat Mass Transf.* 147 (2020) 118949.
- [46] J.H. Irving, J.G. Kirkwood, The statistical mechanical theory of transport processes. IV. The equations of hydrodynamics, *J. Chem. Phys.* 18 (1950) 817–829.
- [47] Y. Guo, D. Surblys, Y. Kawagoe, H. Matsubara, X. Liu, T. Ohara, A molecular dynamics study on the effect of surfactant adsorption on heat transfer at a solid-liquid interface, *Int. J. Heat Mass Transf.* 135 (2019) 115–123.
- [48] M. Barisik, A. Beskok, Boundary treatment effects on molecular dynamics simulations of interface thermal resistance, *J. Comput. Phys.* 231 (2012) 7881–7892.
- [49] O. Yenigun, M. Barisik, Effect of nano-film thickness on thermal resistance at water/silicon interface, *Int. J. Heat Mass Transf.* 134 (2019) 634–640.

# Quasi-Casimir coupling can induce thermal resonance of adsorbed liquid layers in a nanogap

Wentao Chen<sup>a</sup>, Gyoko Nagayama<sup>b,\*</sup>

<sup>a</sup> Graduate School of Engineering, Kyushu Institute of Technology, 1-1 Sensui, Tobata, Kitakyushu, Fukuoka 804-8550, Japan

<sup>b</sup> Department of Mechanical Engineering, Kyushu Institute of Technology, 1-1 Sensui, Tobata, Kitakyushu, Fukuoka 804-8550, Japan

## Abstract

In a vacuum nanogap, phonon heat transfer can be induced by quasi-Casimir coupling without electromagnetic fields. However, it is unknown whether phonons can be transmitted across a nanogap via solid-like liquid layers adsorbed on the superhydrophilic solid surfaces. Here, we elucidate that the phonon transmission across a nanogap can be induced by quasi-Casimir coupling via liquid layers using classical non-equilibrium molecular dynamics simulation. We firstly show that the quasi-Casimir coupling exists between interfacial solid–liquid or liquid–liquid layers. The thermal resonance between two liquid layers can be induced by the quasi-Casimir coupling, agitating the co-occurrence of the thermal resonance between interfacial solid layers, while liquid monolayer disturbs the resonance. On the occurrence of thermal resonance between liquid layers, larger heat flux and thermal gap conductance can be achieved, while the interfacial liquid layer limits the acoustic phonon transmission in the interfacial solid layers. The fundamental understanding of quasi-Casimir heat transfer at the solid–liquid interface could pave the way for future nanoscale energy transport and thermal management.

## 1 Introduction

Near-field heat transfer (NFHT) has attracted considerable interest in modern nanoscale heat transfer. In the transition regime from heat conduction to NFHT, phonon transmission dominates the heat transfer mechanism between two objects and thus the scale of nanogap plays an important role in the NFHT. Thermal energy transport between two objects separated by a vacuum nanogap is several orders of magnitude larger than Planck's blackbody limit,<sup>1–12</sup> where phonons act as efficient thermal carriers.<sup>13–15</sup> The phonon coupling in electric fields contributes to phonon transmission between two solids as gap distance  $D < 5$  nm,<sup>16,17</sup> while the quantum fluctuation in electromagnetic fields induces Casimir heat transfer between two Si<sub>3</sub>N<sub>4</sub> membranes as  $D < 400$  nm.<sup>18</sup>

In our previous study, a new heat transfer mechanism named quasi-Casimir coupling induced phonon heat transfer has been proposed across a vacuum gap of  $D < 1$  nm with the aid of molecular interactions between two solid walls.<sup>19</sup> As thermal agitation of the wall atoms gives rise to phonons (atomic vibration), the wall surface undulates over time. When the two wall surfaces are in close proximity, both surfaces are subjected to a time-varying force owing to their interactions with the undulations of the surfaces. Thus, phonons are transmitted across the vacuum gap between the two walls. As a result, significant heat transfer enhancement between two

parallel walls has been verified by narrowing the gap distance, achieving extremely high heat flux up to a magnitude of  $10^{10}$  W/m<sup>2</sup> level. Our results revealed that thermal resonance can be induced by quasi-Casimir coupling between the interfacial solid layers, providing a phonon transmission channel across a vacuum gap in the transition regime from heat conduction to NFHT.

Fig. 1 illustrates a schematic of quasi-Casimir heat transfer in a nanogap between two objects with liquid layers in the transition regime. Casimir heat transfer, as well as the quasi-Casimir heat transfer have been verified in a vacuum nanogap.<sup>18,19</sup> Meanwhile, the presence of liquid in the nanogap is of certain importance to get a better understanding of the nanoscale heat transfer at the solid–liquid interface.

The nanoscale heat transfer at the solid–liquid interface can be manipulated by the surface wettability,<sup>20–23</sup> nanostructure,<sup>24–28</sup> surfactant adsorption,<sup>29–31</sup> self-assembled monolayer,<sup>32–34</sup> atomic surface terminations,<sup>35</sup> nanoparticle,<sup>36</sup> temperature,<sup>37,38</sup> and liquid pressure.<sup>39,40</sup> The ordered liquid layer adjacent to the solid surface can increase the thermal conductivity of interfacial liquid layers.<sup>24,41</sup> In the case of a liquid monolayer firmly sandwiched by two solid walls, the thermal resistance becomes extremely low at the solid–liquid interface in comparison with the cases of multiple layers.<sup>42–44</sup> Furthermore, the thermal resistance of liquid confined in parallel-aligned walls is lower than that in cross-aligned walls.<sup>44</sup> Additionally, the gap distance can be the critical factor to determine the heat transfer in a nanogap between two objects in contact with liquid. As shown in Fig. 1, the molecular interactions between the adsorbed liquid layers on the superhydrophilic solid surfaces may contribute to the phonon heat transfer from heat conduction to quasi-Casimir heat transfer.

However, whether the quasi-Casimir coupling can induce the phonon transmission across a nanogap via liquid layers, is still an open question. In this study, the classical non-equilibrium molecular dynamics (NEMD) simulations were carried out to examine the phonon heat transfer across a nanogap with liquid layer, with a focus on the quasi-Casimir coupling and thermal resonance. The liquid monolayer adsorbed on the cooling/heating surfaces, and two liquid layers adsorbed on both the cooling and heating surfaces were simulated to verify the possible quasi-Casimir coupling or thermal resonance. Consequently, we confirmed the existence of the quasi-Casimir coupling between both the interfacial solid–liquid and liquid–liquid layers. In spite of the thermal resonance at the interfacial solid layers, we also found that the interfacial liquid layers were subjected to the thermal resonance based on the wave analysis. In addition, the effects of the liquid layer on the vibrational density of state (VDOS),

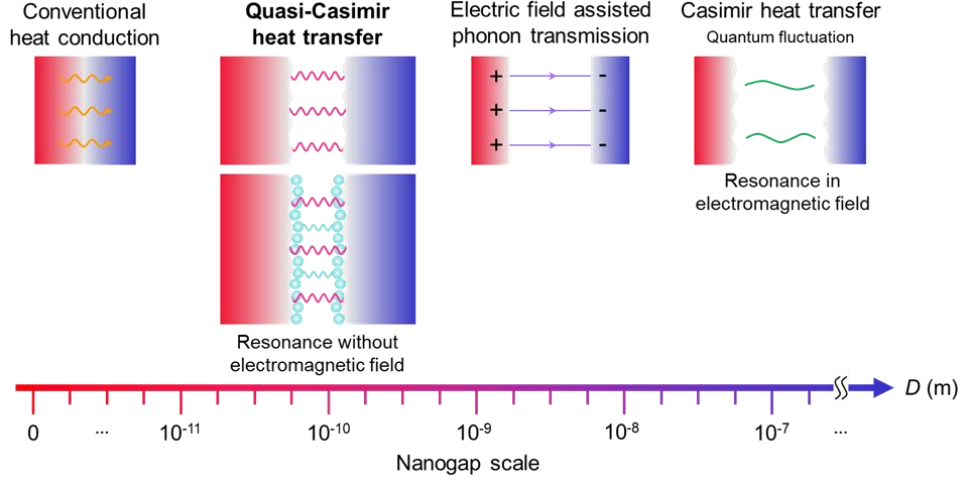


**Fig. 1** A schematic of quasi-Casimir heat transfer in a nanogap between two objects with liquid layer in the transition regime from heat conduction to NFHT.

thermal gap conductance and heat flux were clarified. Our results reveal that quasi-Casimir coupling at solid–liquid interface can induce thermal resonance of liquid layers in a nanogap.

## 2 Simulation methods

The NEMD method<sup>45–51</sup> was utilized to simulate the phonon heat transfer across a nanogap including the liquid layers between the heating wall (red) and the cooling wall (blue), as shown in Fig. 2. The dimensions of the computational domain were  $L_x = 5.552$  nm,  $L_y = 3.847$  nm, and  $L_z = 2.206–4.165$  nm. The two parallel solid walls were separated by a distance  $D$  of  $0.392–2.352$  nm ( $1a–6a$ , where  $a$  is the lattice constant of platinum  $0.392$  nm<sup>52</sup>). Each solid wall was composed of four layers of 1280 platinum atoms in face-centered cubic lattices and its  $\langle 111 \rangle$  crystal plane faced to the nanogap. The Lennard-Jones (LJ) liquid of 190–380 argon atoms was confined in the nanogap between the two solid walls, resulting in a smaller distance  $d$  of  $0–2.057$  nm than  $D$ . The maximum atom number for the liquid monolayer adsorbed on the solid surface was approximate to 190, as shown in Fig. 2(b) and (d). The outermost layers of the heating and cooling walls were maintained at the constant temperature of 120 K and 100 K, respectively, using the velocity scaling method.<sup>53</sup> Periodic boundary conditions were utilized along the  $x$ - and  $y$ -directions.

The molecular interactions were modeled by the LJ potential as follows:

$$\phi(r_{ij}) = 4\varepsilon \left[ \left( \frac{\sigma}{r_{ij}} \right)^{12} - \left( \frac{\sigma}{r_{ij}} \right)^6 \right], \quad (1)$$

where  $r_{ij}$  is the distance between two atoms  $i$  and  $j$ ,  $\sigma$  is the length parameter, and  $\varepsilon$  is the energy parameter. The parameters are  $\sigma_1 = 3.405$  Å,  $\varepsilon_1 = 1.67 \times 10^{-21}$  J for the liquid–liquid interaction of argon, and  $\sigma_s = 2.475$  Å,  $\varepsilon_s = 8.35 \times 10^{-20}$  J ( $\approx 50\varepsilon_1$ ) for the solid–solid interaction of platinum. For the solid–liquid interaction between argon and platinum, the empirical approximations  $\sigma_{sl} = (\sigma_1 + \sigma_s)/2$ , and  $\varepsilon_{sl} = \sqrt{\varepsilon_1 \varepsilon_s} \approx 7\varepsilon_1$  were utilized based on the Lorentz-Berthelot combining rule<sup>54,55</sup> to form the adsorbed liquid

layer on the solid surface. The adsorbed layer of liquid differs from the bulk liquid, showing solid-like behavior. The contact angle of an argon droplet on a platinum surface has been found to be zero, representing a superhydrophilic solid surface.<sup>23,47</sup> Additional simulations with  $\varepsilon_{sl} \approx 5.6\varepsilon_1$  and  $3.5\varepsilon_1$  were conducted to confirm the quasi-Casimir coupling between the adsorbed liquid layers at solid–liquid interfaces in section 3.2.

All the simulations were carried out with a cut-off radius of  $1.703$  nm ( $5\sigma_1$ ) chosen for the spherically truncated and shifted potential. The velocity Verlet algorithm was utilized to integrate the equations of motion with a time step of 5 fs. The systems were initially equilibrated at 100 K after achieving a steady state for 5 ns. Subsequently, all NEMD simulations were conducted to reach the steady state for 50 ns with constant heat flow ( $\Delta E = E_H - E_C \cong 0$ ) by monitoring the cumulative input and output energies  $E_H$  and  $E_C$  in the heating (120 K) and cooling (100 K) thermostats.

The data sampling was carried out for 5 ns to calculate the temperature of each solid and liquid layer in the steady state. The heat flux passing through the system was acquired using the mean value for the last 15 ns within a 50 ns time window. The heat flux is

$$q = \frac{1}{A} \cdot \frac{\partial E}{\partial t}, \quad (2)$$

where  $A$  is the cross-sectional area of the  $x$ - $y$  plane,  $\partial E / \partial t$  is the heat transfer rate in the heating or cooling thermostat, and  $E$  is the cumulative energy of the heating ( $E_H$ ) or cooling ( $E_C$ ) thermostat. The thermal gap conductance between the interfacial layers can be calculated as

$$G = \frac{q}{T_{Hi} - T_{Ci}}, \quad (3)$$

where  $T_{Hi}$  is the temperature of the heating interfacial solid layer ( $T_{His}$ ) or liquid layer ( $T_{Hil}$ ), and  $T_{Ci}$  is the temperature of the cooling interfacial solid layer ( $T_{Cis}$ ) or liquid layer ( $T_{Cil}$ ), as shown in Fig. 2(e).

To evaluate the atomic vibrational characteristics, the atomic vibrational displacements and frequencies were analyzed using the wave graph. The signal analysis of the atomic positions from the NEMD simulation data for 20,000 time steps was conducted to obtain the wave graphs.<sup>56</sup> The equilibrium position of the atoms in the  $z$ -direction is

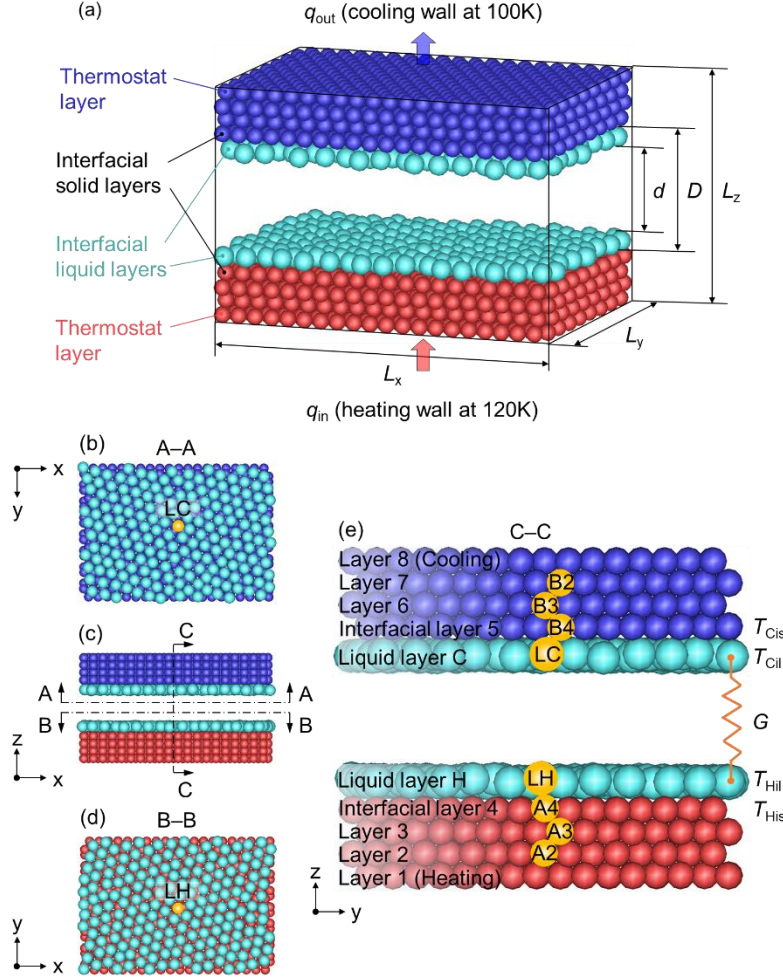


**Fig. 2** NEMD simulation system and atomic positions located at the center of interfacial and inner layers for analyzing the atomic vibrational characteristics. (a) Thermal energy transport between two parallel solid walls separated by a nanogap including solid-like liquid layers; (b) atom LC at interfacial liquid layer C in the A–A directional view; (c) front view ( $x$ - $z$  plane); (d) atom LH at liquid layer H in the B–B directional view; (e) atoms A2, A3, A4 and B2, B3, B4 at the solid layers as well as atoms LH and LC at the liquid layers in the C–C directional enlarged view.

$$\bar{z} = \frac{1}{t_f - t_0} \sum_{t_0}^{t_f} z_{i,t}, \quad (4)$$

where  $z_{i,t}$  is the position of atom  $i$  at time  $t$  in the  $z$ -direction, and atom  $i$  is located at the center of each solid and liquid layer;  $t_0$  is the initial time at which the data output begins, and  $t_f$  is the long finite time for 20,000 time steps. The original vibrational displacements of atom  $i$  can be obtained from  $\Delta z_{i,t} = z_{i,t} - \bar{z}$ . Then, the Fourier transform of the original vibrational displacements was used to analyze the distribution of signal power in the frequency domain (power spectrum). To reduce the noise from the original vibrational displacements, the dominant frequency band was selected to conduct signal filtering. Therefore, the regular wave graphs can be plotted as the time history of the displacement for the specific atoms. The peak amplitude and frequency were determined from the wave graphs. The locations of the specific atoms for signal analysis are illustrated in Fig. 2, where A2, A3 and A4 are the center atoms in the solid layers of the heating wall, B2, B3 and B4 are the center atoms in the solid layers of the cooling wall, LH and LC are the center atoms in the interfacial liquid layers neighboring to A4 and B4, respectively.

The VDOS<sup>57–59</sup> of the interfacial layer was calculated using the velocities of all the atoms at the interfacial solid and liquid layers by the Fourier transform of the velocity autocorrelation function during a period of 20,000 time steps:

$$VDOS(\omega) = \int_0^\infty \langle \vec{v}(t) \vec{v}(0) \rangle e^{-i\omega t} dt, \quad (5)$$

where  $\omega$  is the angular frequency, and  $v(t)$  is the atomic velocity at time  $t$ .

### 3 Results and discussion

#### 3.1 Quasi-Casimir coupling via a liquid monolayer

We have demonstrated that the thermal resonance was induced by the quasi-Casimir coupling across a vacuum gap between the two interfacial solid layers.<sup>19</sup> In this section, we discuss the atomic vibrational characteristics when two solid walls are separated by a nanogap with a liquid monolayer.

To begin with, a firmly connected solid–liquid–solid system is compared with a system of a vacuum gap between two solids at  $D = 1a$ . The left side of Fig. 3 shows the snapshots of the simulated systems. For the solid–liquid–solid system, as shown in Fig. 3(a) and (b), the peak amplitudes of the atom LC/LH in the liquid monolayer (green) are larger than those of the solid atoms, while the interfacial solid atoms A4 (red) and B4 (blue) are in harmony with the liquid atom LC/LH. Comparing with the inner solid atoms (A2, A3, B2, B3), the interfacial solid atom vibrates with a larger amplitude but a lower frequency. This phenomenon is more significant in the case of the liquid monolayer than that of a vacuum gap (without liquid monolayer) as shown in Fig. 3(c) and (d). As demonstrated in our previous study,<sup>19</sup> owing to the presence of two interfaces separated by a vacuum gap, the quasi-Casimir coupling stimulated the interfacial undulations and thus induced the thermal resonance through molecular interaction (see Fig. 3(g)). Similarly, in Fig. 3(e), the thermal resonance can be confirmed by the perfect overlapped vibrational displacements of the atoms A4, B4. However, this thermal resonance is induced by quasi-Casimir coupling between two interfacial solid layers across a liquid monolayer instead of the vacuum gap. Accordingly, the VDOSs of solid layer 4 completely match those of layer 5 in Fig. 3(f) and (h), where the peaks correspond to the vibrational frequencies of A4, B4 (see Table 1). Nevertheless,

the VDOSs of the liquid monolayer (layer C/H) mismatch with those of the solid layers, and the vibrational frequency of LC/LH is much smaller than that of the solid atoms. Although the thermal resonance occurs in the simulation systems with liquid monolayer, the interfacial solid layers with the liquid monolayer are subjected to a stronger surface undulation. That is, the liquid monolayer enhances the thermal resonance between the interfacial solid layers.

### 3.1.1 Liquid monolayer adsorbed on the cooling solid surface

To verify the quasi-Casimir coupling between the interfacial solid and liquid layers separated by a nanogap, we analyzed the atomic vibrational characteristics when the liquid monolayer was adsorbed on the cooling solid surface. The snapshots of the simulated systems with different gap distances  $D$  are shown on the left side of Fig. 4. In the case of  $D = 1.5a$ , the interfacial liquid atom LC vibrates with a higher peak amplitude than the solid atoms, as shown in Fig. 4(a) and (b). This difference diminishes at  $D = 2a$  and almost disappears at  $D = 6a$ , owing to the weaker molecular interactions between the interfacial solid and liquid atoms (see Fig. 4(c)–(f)). Meanwhile, the peak amplitudes of the interfacial solid atoms A4, B4 are larger than those of the inner solid atoms at  $D = 1.5a$  and  $2a$ , but nearly identical at  $D = 6a$ . From Fig. 4(g), (i) and (k), the liquid monolayer disturbs the thermal resonance on account of the completely different atomic

**Table 1** The peak amplitudes and frequencies of atoms in the inner solid layers as well as interfacial solid and liquid layers.

$D/d$ (nm)	Ar atoms	A2	A3	A4	B2	B3	B4	LH	LC
Peak amplitude (pm)									
0.392 / 0.392	0	1.006	1.077	1.380	0.844	0.812	1.363	–	–
0.392 / 0.000	190	1.100	0.955	2.031	0.944	0.890	1.930	2.474	–
0.588 / 0.293	190 (C)	0.925	0.992	1.562	0.932	1.064	1.267	–	3.152
0.588 / 0.293	190 (H)	1.093	0.924	1.756	1.093	0.956	1.738	3.802	–
0.588 / 0.000	380	1.012	0.909	1.818	0.996	0.975	1.806	3.122	3.033
0.784 / 0.489	190 (C)	1.071	0.921	1.328	1.006	0.969	1.015	–	2.032
0.784 / 0.489	190 (H)	1.065	0.943	1.555	1.058	1.031	1.356	2.050	–
0.784 / 0.193	380	0.985	0.959	1.576	0.938	0.986	1.595	4.249	4.077
2.352 / 2.057	190 (C)	0.977	1.015	1.061	0.961	0.970	1.085	–	1.185
2.352 / 2.057	190 (H)	0.983	1.067	1.070	0.955	0.963	1.032	1.250	–
2.352 / 1.761	380	0.971	0.923	1.070	1.066	1.029	0.932	1.285	1.131
Frequency $f$ (THz)									
0.392 / 0.392	0	4.673	4.157	3.242	3.982	4.159	3.236	–	–
0.392 / 0.000	190	4.607	4.247	3.325	3.976	4.236	3.322	1.345	–
0.588 / 0.293	190 (C)	4.547	4.171	3.310	4.061	3.832	3.474	–	2.358
0.588 / 0.293	190 (H)	4.597	4.236	3.525	4.375	4.160	3.394	2.424	–
0.588 / 0.000	380	4.618	4.304	3.261	4.270	4.136	3.250	2.768	2.769
0.784 / 0.489	190 (C)	4.376	4.246	3.302	4.077	4.281	3.462	–	2.313
0.784 / 0.489	190 (H)	4.388	4.284	3.539	4.248	4.154	3.348	2.384	–
0.784 / 0.193	380	4.587	4.254	3.515	4.037	4.221	3.510	2.668	2.668
2.352 / 2.057	190 (C)	4.379	4.173	3.178	4.002	4.280	3.442	–	2.163
2.352 / 2.057	190 (H)	4.323	4.058	3.215	4.233	4.149	3.149	2.168	–
2.352 / 1.761	380	4.134	4.220	3.165	4.079	4.181	2.765	2.374	2.125

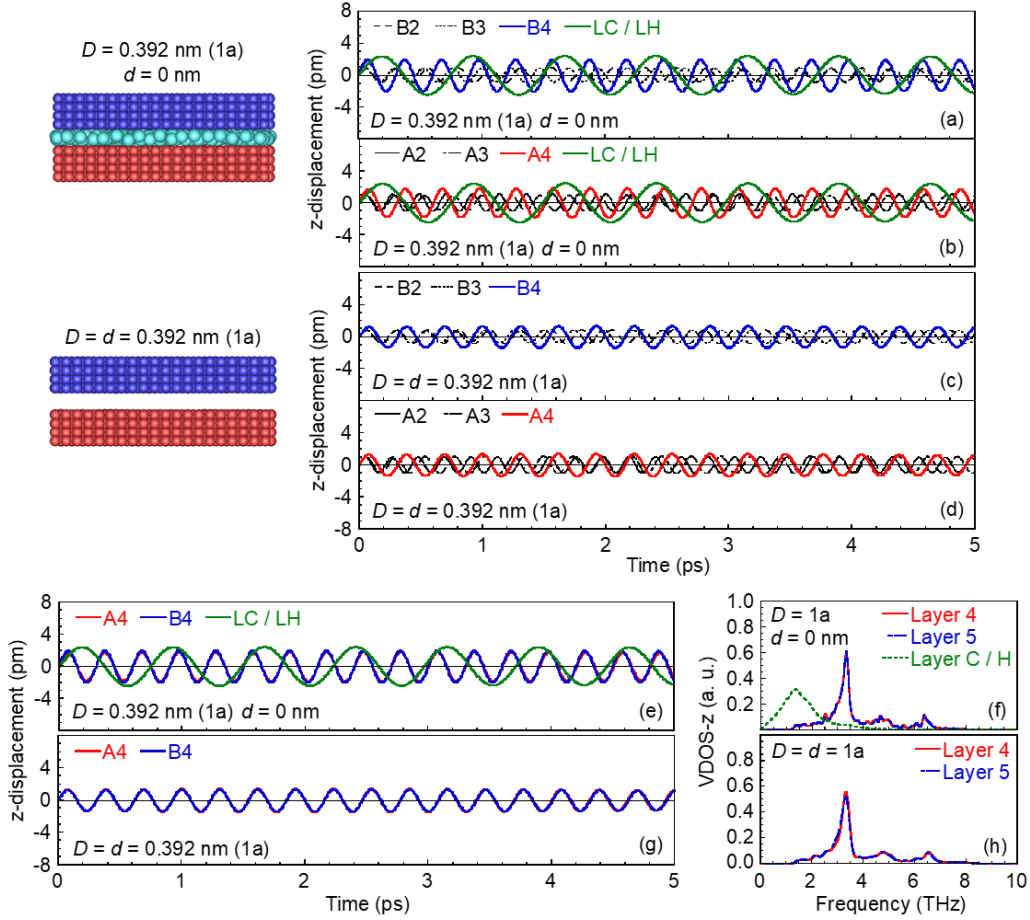


**Fig. 3** Atomic vibrational displacements of specific atoms at (a) solid layers in cooling wall and liquid monolayer, (b) solid layers in heating wall and liquid monolayer, for a firmly connected solid–liquid–solid system; (c) solid layers in cooling wall, (d) solid layers in heating wall, for a solid–vacuum–solid system. Atomic vibrational displacement of specific atoms and VDOSs at interfacial solid layers and liquid monolayer for (e–f) a firmly connected solid–liquid–solid system, (g–h) a solid–vacuum–solid system.

vibrational displacements. The vibrational frequency of the atom LC is lower than that of the solid atoms as listed in Table 1. Therefore, the obvious phonon mismatches were observed in the VDOSs of solid layers 4, 5 and liquid layer C, as depicted in Fig. 4(h), (j) and (l). Although the peaks of the VDOSs for the interfacial solid layers separated by the vacuum gap overlap well (see Fig. 3(h)), those for the cooling interfacial solid layer 5 decrease significantly due to the presence of the adsorbed liquid layer. That is, the liquid layer limits the peak of the VDOS at the cooling interfacial solid layer and thus suppresses the acoustic phonon transmission. Nevertheless, these results verify the existence of the quasi-Casimir coupling between the liquid monolayer adsorbed on the cooling surface and the interfacial solid layer.

### 3.1.2 Liquid monolayer adsorbed on the heating solid surface

The snapshots of the simulated systems for the liquid monolayer adsorbed on the heating solid surface are shown on the left side of Fig. 5. Coinciding with section 3.1.1, the vibrational displacements of the interfacial solid and liquid atoms increase with a decrease of the gap distance, owing to the enhanced quasi-Casimir coupling. Interestingly, the peak amplitudes and vibrational frequencies of the interfacial solid

and liquid atoms in the cases of  $D = 1.5a$  are larger than those shown in Fig. 4. Several liquid atoms are excluded from the adsorbed liquid layer on the heating solid surface in the case of  $D = 1.5a$ . Unlike the interfacial solid layers 4 and 5 separated by the vacuum gap (see Fig. 3(h)), the peaks of the VDOSs for the heating interfacial solid layer 4 decrease significantly due to the presence of the adsorbed liquid layer. Similar to section 3.1.1, the liquid layer limits the peak of the VDOS at the adjacent interfacial solid layer and thus reduces the acoustic phonon transmission through the adjacent solid layer.

### 3.2 Thermal resonance induced by quasi-Casimir coupling between two liquid layers

The effect of the liquid monolayer on the phonon transmission has been clarified in section 3.1, subsequently, those of two liquid layers adsorbed on both the heating and cooling solid surfaces are discussed hereafter. The snapshots of the simulated systems including two liquid layers are shown on the left side of Fig. 6. In the case of  $D = 2a$ , the peak amplitudes of interfacial liquid atoms LH (yellow) and LC (green) are significantly larger than those of the solid atoms, while this difference decreases at  $D = 1.5a$  and becomes insignificant at  $D = 6a$ , as shown in Fig. 6(a)–(f). In accord with section 3.1, the undulations of the interfacial liquid layers are strengthened as a result

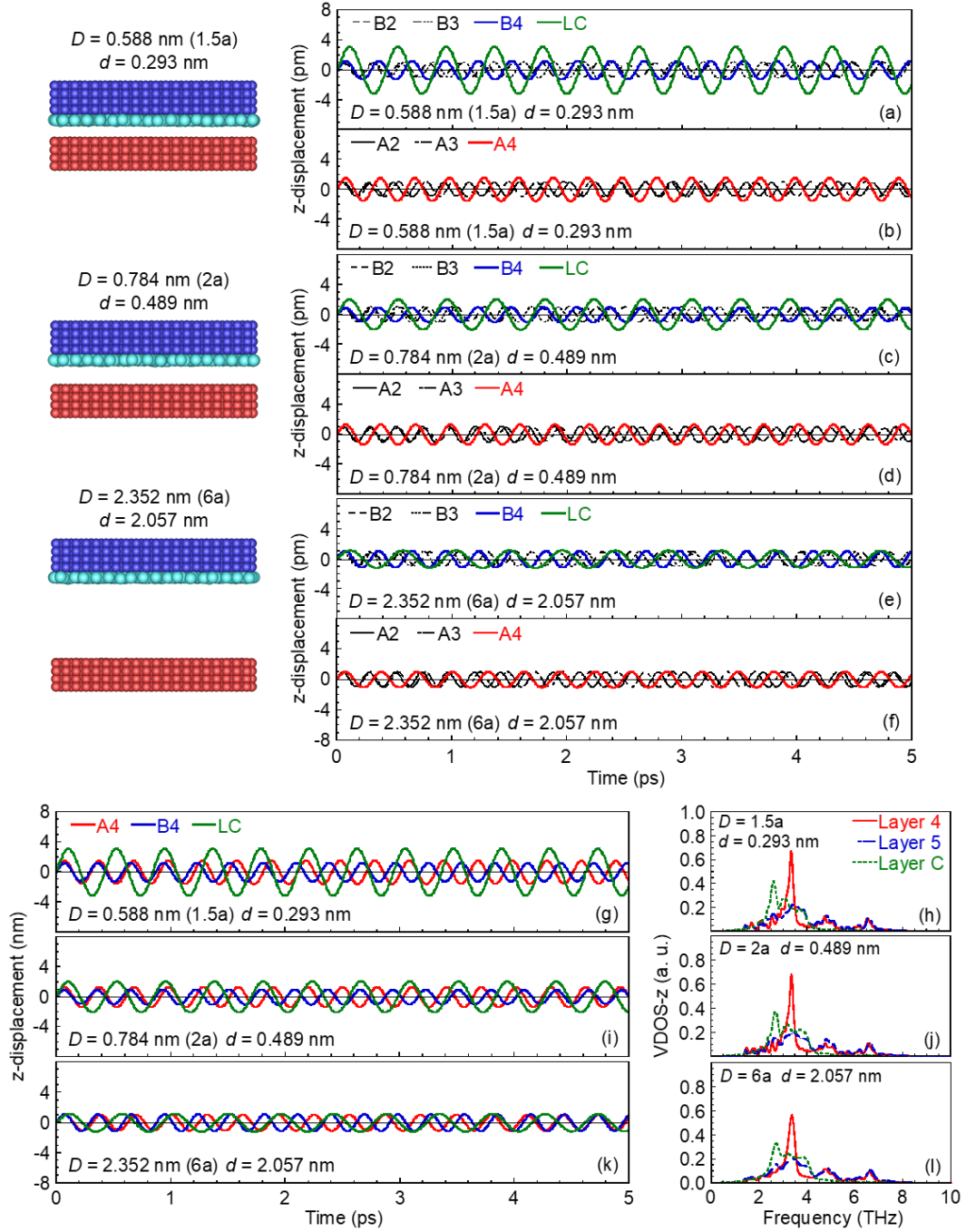


**Fig. 4** Atomic vibrational displacements of specific atoms in the heating and cooling walls as well as the liquid monolayer adsorbed on the cooling solid surface at varying gap distance (a–b)  $D = 1.5a$ , (c–d)  $D = 2a$  and (e–f)  $D = 6a$ . Atomic vibrational displacement of specific atoms and VDOSs at interfacial solid layers and liquid monolayer adsorbed on the cooling solid surface at (g–h)  $D = 1.5a$ , (i–j)  $D = 2a$  and (k–l)  $D = 6a$ .

of the increased molecular interactions with decreasing  $D$ . Thus, the quasi-Casimir coupling can exist between two interfacial liquid layers H and C. Meanwhile, the interfacial solid atoms A4 (red) and B4 (blue) vibrate with larger peak amplitude at  $D = 1.5a$  and  $2a$  than  $D = 6a$ . Additionally, in the cases of  $D = 1.5a$  and  $2a$ , the thermal resonance occurs between the interfacial solid layers 4 and 5 as well as liquid layers H and C, respectively, which is evidenced by the perfect overlapped vibrational displacements of the atoms A4–B4 and

LH–LC (see Fig. 6(g) and (i)). Similar to the interfacial solid layers, the VDOSs of liquid layers completely match each other, even though the adsorbed liquid layers limit the peaks of the VDOSs in the interfacial solid layers and suppress the acoustic phonon transmission (see Fig. 6(h) and (j)). However, the thermal resonance disappears in the case of  $D = 6a$  shown in Fig. 6(k) and (l). It is worth noting that the thermal resonance between two liquid layers agitates the co-occurrence of the thermal resonance between interfacial solid layers.

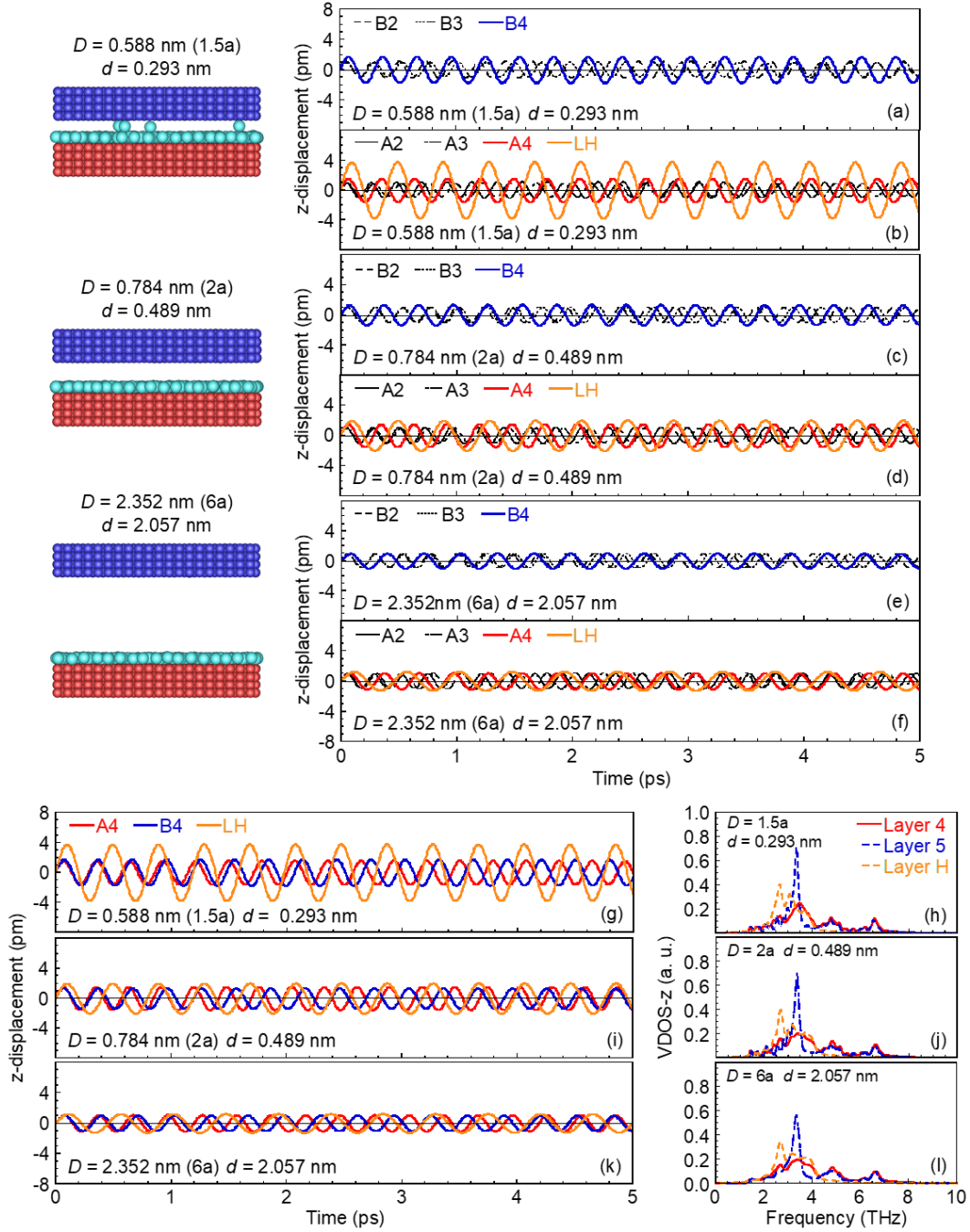


**Fig. 5** Atomic vibrational displacements of specific atoms in the heating and cooling walls as well as the liquid monolayer adsorbed on the heating solid surface at varying gap distance (a–b)  $D = 1.5a$ , (c–d)  $D = 2a$  and (e–f)  $D = 6a$ . Atomic vibrational displacement of specific atoms and VDOSs at interfacial solid layers and liquid monolayer adsorbed on the heating solid surface at (g–h)  $D = 1.5a$ , (i–j)  $D = 2a$  and (k–l)  $D = 6a$ .

These results demonstrate that the quasi-Casimir coupling at the solid–liquid interface can induce the thermal resonance between liquid layers in a nanogap.

Similar results can be found in Fig. 7, where  $\varepsilon_{sl} / \varepsilon_1 \approx 5.6$  and  $3.5$  at  $D = 2a$ . Coinciding with the case of  $\varepsilon_{sl} / \varepsilon_1 \approx 7$ , the quasi-Casimir coupling are verified between two interfacial liquid layers H and C (Fig. 7(a)–(d)). In Fig. 7(e)–(h), thermal resonance between the interfacial solid layers 4 and 5 occurs as well as that between liquid layers H and C, while decreasing  $\varepsilon_{sl}$  results in an increasing in the

atomic vibrational displacements. That is, when the stable liquid layers are adsorbed on the solid surfaces,  $\varepsilon_{sl}$  is not the key factor for the quasi-Casimir heat transfer and thermal resonance via adsorbed liquid layers.

### 3.3 Thermal energy transport across a nanogap

For the reason that both heating and cooling surfaces are subjected to the quasi-Casimir coupling induced by molecular interactions, the

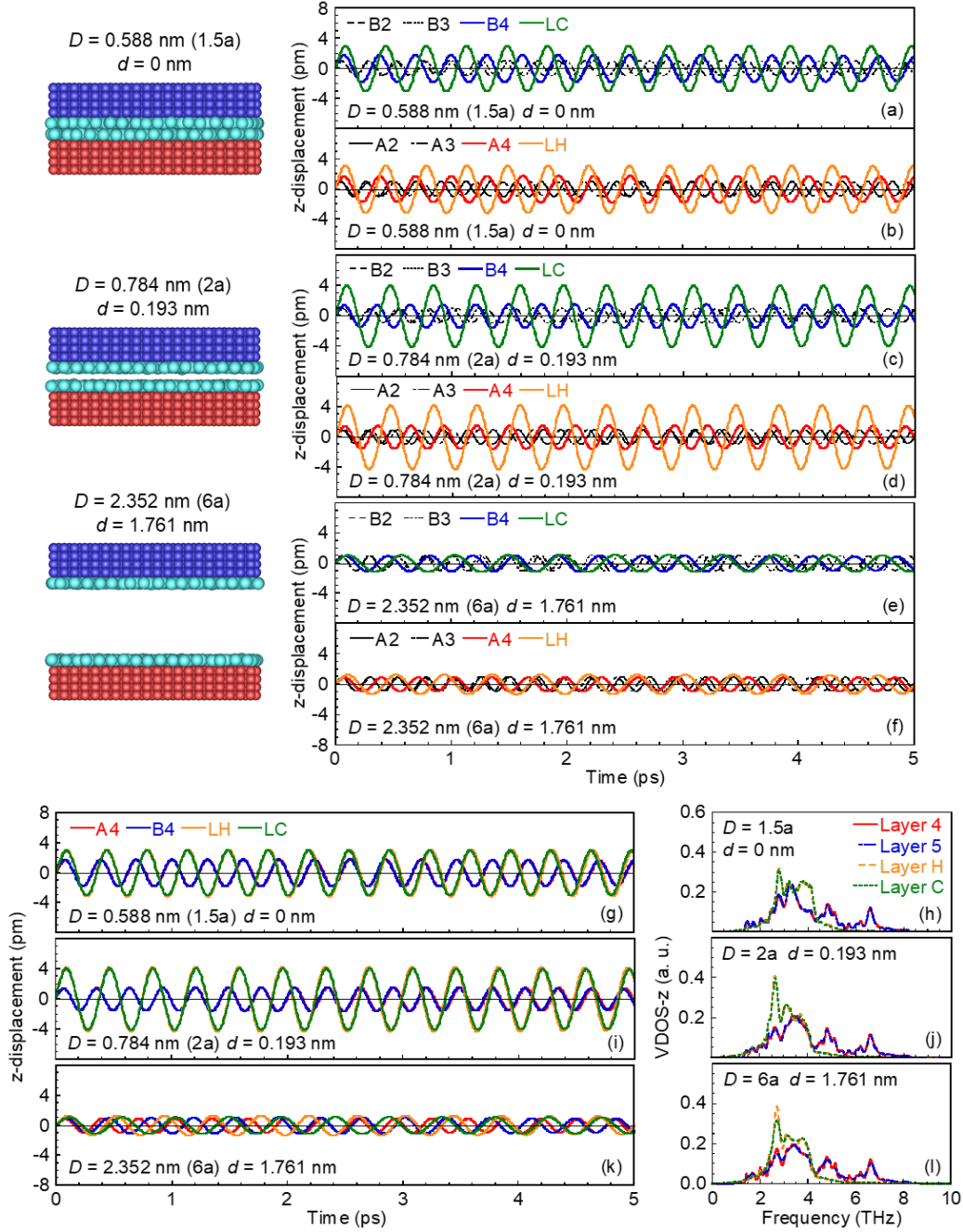


**Fig. 6** Atomic vibrational displacements of specific atoms in the heating and cooling walls as well as the liquid layers adsorbed on the cooling and heating solid surfaces at varying gap distance (a–b)  $D = 1.5a$ , (c–d)  $D = 2a$  and (e–f)  $D = 6a$ . Atomic vibrational displacements of specific atoms and VDOSs at interfacial solid layers and liquid monolayer adsorbed on the cooling and heating solid surfaces at (g–h)  $D = 1.5a$ , (i–j)  $D = 2a$  and (k–l)  $D = 6a$ .

thermal energy transports from the heating object to the cooling one with the surface undulations. Accordingly, the net heat flux  $q$  of the system and thermal gap conductance  $G$  between the interfacial layers (see Fig. 2(e)) were obtained by performing the data sampling over 15 ns to investigate the gap-dependent thermal energy transport.

Due to the strengthened molecular interactions between the interfacial solid and liquid atoms,  $q$  and  $G$  exponentially increase with decreasing  $D$  (see Fig. 8(a), (b) and Table 2). Larger  $q$  and  $G$  acquired in the cases of the liquid layers adsorbed onto the solid surfaces, comparing with the cases of the vacuum gap (circle dots). Surprisingly, one to three

orders of magnitude enhancement in  $q$  and  $G$  (red dots) is achieved under the thermal resonance between the two liquid layers. Additionally,  $q$  and  $G$  for the liquid monolayer adsorbed on the heating solid surface (blue dots) are larger than those on the cooling solid surface (green dots) at  $D = 0.588$  nm. The root reason for this deviation attributes to the stronger vibration of the interfacial atoms at the heating surface than that at the cooling surface. For reference, on the basis of an alternative gap distance  $d$  between the interfacial solid–liquid or liquid–liquid layers for  $x$ -axis,  $q$  and  $G$  are lower than those in the cases of the vacuum gap shown in Fig. 7(c) and (d). This is

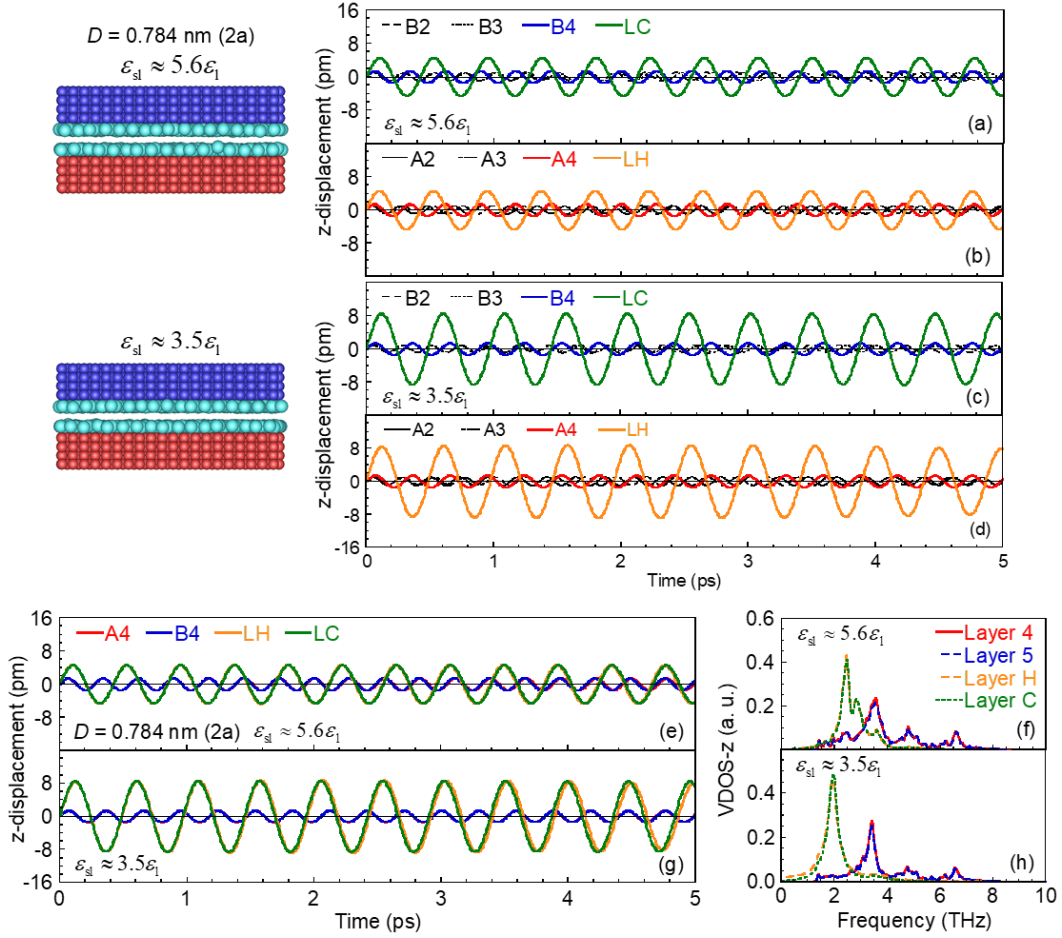


**Fig. 7** Atomic vibrational displacements of specific atoms in the heating and cooling walls as well as the liquid layers adsorbed on the cooling and heating solid surfaces at varying energy parameters  $\varepsilon_{sl}$ : (a–b)  $\varepsilon_{sl} \approx 5.6\varepsilon_1$ ; (c–d)  $\varepsilon_{sl} \approx 3.5\varepsilon_1$ . Atomic vibrational displacements of specific atoms and VDOSs at interfacial solid layers and liquid monolayers adsorbed on the cooling and heating solid surfaces at varying energy parameters  $\varepsilon_{sl}$ : (e–f)  $\varepsilon_{sl} \approx 5.6\varepsilon_1$ ; (g–h)  $\varepsilon_{sl} \approx 3.5\varepsilon_1$ .

because that the quasi-Casimir coupling between the interfacial liquid–liquid or solid–liquid layers is weaker than that between the interfacial solid–solid layers at the same  $d$ . It is notable that  $q$  and  $G$  with two liquid layers (red dots at  $D = 0.588$  nm,  $d = 0$ ) is greater than those with liquid monolayer (green/blue dots at  $D = 0.392$  nm,  $d = 0$ ). Due to the simultaneous existence of quasi-Casimir coupling and thermal resonance in nanoscale heat conduction,  $q$  and  $G$  at  $d = 0$  raise considerably compared with those at  $d > 0$ . Nevertheless, for a given  $D$  in molecular scale, the liquid layer still can contribute to the thermal energy transport in the absence of thermal resonance and thus enhances NFHT. Consequently, the quasi-Casimir coupling at the solid–liquid interface is verified as an additional channel for phonon heat transfer across a nanogap.

## Conclusions

NEMD simulations were carried out to study the phonon heat transfer across a nanogap induced by the quasi-Casimir coupling between interfacial layers of solid–liquid or liquid–liquid. The

liquid monolayer adsorbed over the cooling/heating surface, and two liquid layers adsorbed over both the cooling and heating surfaces were focused on to clarify the effect of liquid layer on phonon transmission across a nanogap. The following conclusions have been drawn.

- (1) The quasi-Casimir coupling exists at the solid–liquid interface, not only between solid–liquid but also between liquid–liquid layers.
- (2) The thermal resonance between the two liquid layers can be induced by the quasi-Casimir coupling, agitating the co-occurrence of the thermal resonance between the interfacial solid layers. In contrast, liquid monolayer disturbs the thermal resonance between the interfacial solid layers.
- (3) Owing to the thermal resonance between two liquid layers, heat flux and thermal conductance across the nanogap increase one to three orders of magnitude compared with those across the vacuum gap. Meanwhile, the liquid layer limits the acoustic phonon transmission in the interfacial solid layers.

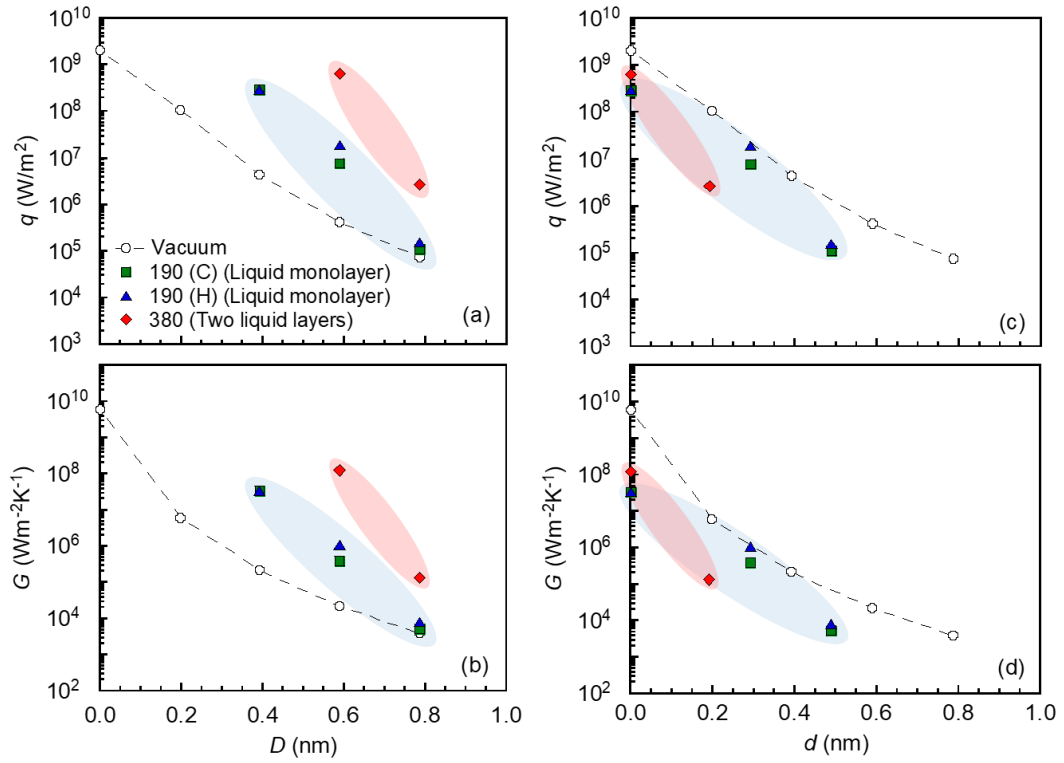


**Fig. 8** Heat flux and thermal gap conductance versus gap distance (a–b)  $D$  between the interfacial solid layers, (c–d)  $d$  between the interfacial solid–liquid or liquid–liquid layers. The dashed line is a guide for the eyes.

**Table 2** Simulation results obtained at different gap distances in the steady non-equilibrium systems.

$D / d$ (nm)	Ar atoms	$T_{\text{His}}$ (K)	$T_{\text{Cis}}$ (K)	$T_{\text{Hil}}$ (K)	$T_{\text{Cil}}$ (K)	$\Delta T$ (K)	$q$ ( $\times 10^6$ Wm $^{-2}$ )	$G$ ( $\times 10^3$ Wm $^{-2}$ K $^{-1}$ )
0.392 / 0.000	190	118.73	101.36	108.74	108.74	8.69	295.66	34042.55
0.588 / 0.293	190 (C)	119.85	100.24	–	100.88	18.97	7.69	405.31
0.588 / 0.293	190 (H)	119.86	100.72	117.86	–	17.14	18.64	1087.76
0.588 / 0.000	380	117.97	102.27	111.62	106.39	5.23	655.48	125331.51
0.784 / 0.489	190 (C)	120.10	100.14	–	99.13	20.97	0.11	5.36
0.784 / 0.489	190 (H)	120.21	100.25	118.90	–	18.65	0.15	8.16
0.784 / 0.193	380	120.20	100.03	120.75	100.36	20.39	2.73	133.85

(4) The heat flux and thermal gap conductance exponentially increase with decreasing gap distance with the aid of liquid layer, evidencing the significance of quasi-Casimir heat transfer in NFHT.

In the present study, we verified that the acoustic phonons can be transmitted across a nanogap via adsorbed liquid layer, attributing to the quasi-Casimir coupling and thermal resonance under strong molecular interaction between liquid and solid. However, no guarantee can be provided to the same phenomena

under the weak molecular interaction between liquid and solid, in particular, where the stable adsorbed liquid layer is not available. Therefore, future work is expected to explore the effects of the weak molecular interaction (e.g. surface hydrophobicity) on the quasi-Casimir phonon heat transfer across a nanogap. The understanding of the quasi-Casimir heat transfer mechanism shall open a new window to optimize NFHT for nanoscale thermal management.

## Author Contributions

W. C.: Investigation, Methodology, Data curation, Formal analysis, Writing - original draft. G. N.: Conceptualization, Methodology, Supervision, Writing - review & editing, Funding acquisition.

## Conflicts of interest

There are no conflicts to declare.

## Acknowledgements

This work was supported by the Ministry of Education, Science and Culture of the Japanese Government through the Grant-in-Aid for Scientific Research, Project No. 18H01385, the research supercomputing services by the Research Institute for Information Technology, Kyushu University, and the Initiative for Realizing Diversity in the Research Environment by Ministry of Education, Culture, Sports, Science and Technology, Japan.

## References

- 1 M. P. Bernardi, D. Milovich and M. Francoeur, *Nat. Commun.*, 2016, **7**, 1–7.
- 2 A. Fiorino, D. Thompson, L. Zhu, R. Mittapally, S. A. Biehs, O. Bezencenet, N. El-Bondry, S. Bansropun, P. Ben-Abdallah, E. Meyhofer and P. Reddy, *ACS Nano*, 2018, **12**, 5174–5179.
- 3 B. Song, Y. Ganjeh, S. Sadat, D. Thompson, A. Fiorino, V. Fernández-Hurtado, J. Feist, F. J. Garcia-Vidal, J. C. Cuevas, P. Reddy and E. Meyhofer, *Nat. Nanotechnol.*, 2015, **10**, 253–258.
- 4 B. Song, D. Thompson, A. Fiorino, Y. Ganjeh, P. Reddy and E. Meyhofer, *Nat. Nanotechnol.*, 2016, **11**, 509–514.
- 5 R. St-Gelais, G. R. Bhatt, L. Zhu, S. Fan and M. Lipson, *ACS Nano*, 2017, **11**, 3001–3009.
- 6 L. Tranchant, S. Hamamura, J. Ordonez-Miranda, T. Yabuki, A. Vega-Flick, F. Cervantes-Alvarez, J. J. Alvarado-Gil, S. Volz and K. Miyazaki, *Nano Lett.*, 2019, **19**, 6924–6930.
- 7 A. Fiorino, D. Thompson, L. Zhu, B. Song, P. Reddy and E. Meyhofer, *Nano Lett.*, 2018, **18**, 3711–3715.
- 8 O. Ilic, N. H. Thomas, T. Christensen, M. C. Sherrott, M. Soljačić, A. J. Minnich, O. D. Miller and H. A. Atwater, *ACS Nano*, 2018, **12**, 2474–2481.
- 9 K. Kim, B. Song, V. Fernández-Hurtado, W. Lee, W. Jeong, L. Cui, D. Thompson, J. Feist, M. T. H. Reid, F. J. García-Vidal, J. C. Cuevas, E. Meyhofer and P. Reddy, *Nature*, 2015, **528**, 387–391.
- 10 K. Kloppstech, N. Köhne, S. A. Biehs, A. W. Rodriguez, L. Worbes, D. Hellmann and A. Kittel, *Nat. Commun.*, 2017, **8**, 1–6.
- 11 M. Nomura, *Nat. Nanotechnol.*, 2016, **11**, 496–497.
- 12 S. Shen, A. Narayanaswamy and G. Chen, *Nano Lett.*, 2009, **9**, 2909–2913.
- 13 A. Alkurdi, C. Adessi, F. Tabatabaei, S. Li, K. Termentzidis and S. Merabia, *Int. J. Heat Mass Transf.*, 2020, **158**, 119963.
- 14 B. V. Budaev and D. B. Bogy, *J. Appl. Phys.*, 2020, **128**, 094305.
- 15 D. P. Sellan, E. S. Landry, K. Sasihithlu, A. Narayanaswamy, A. J. H. McGaughey and C. H. Amon, *Phys. Rev. B*, 2012, **85**, 1–6.
- 16 V. Chiloyan, J. Garg, K. Esfarjani and G. Chen, *Nat. Commun.*, 2015, **6**, 6755.
- 17 T. Tokunaga, A. Jarzembski, T. Shiga, K. Park and M. Francoeur, *Phys. Rev. B*, 2021, **104**, 25–30.
- 18 K. Y. Fong, H.-K. Li, R. Zhao, S. Yang, Y. Wang and X. Zhang, *Nature*, 2019, **576**, 243–247.
- 19 W. Chen and G. Nagayama, *Int. J. Heat Mass Transf.*, 2021, **176**, 121431.
- 20 C. U. Gonzalez-Valle, S. Kumar and B. Ramos-Alvarado, *J. Phys. Chem. C*, 2018, **122**, 7179–7186.
- 21 C. U. Gonzalez-Valle and B. Ramos-Alvarado, *ACS Appl. Nano Mater.*, 2021, **4**, 3821–3832.
- 22 B. Ramos-Alvarado, S. Kumar and G. P. Peterson, *J. Phys. Chem. Lett.*, 2016, **7**, 3497–3501.
- 23 G. Nagayama and P. Cheng, *Int. J. Heat Mass Transf.*, 2004, **47**, 501–513.
- 24 G. Nagayama, M. Kawagoe, A. Tokunaga and T. Tsuruta, *Int. J. Therm. Sci.*, 2010, **49**, 59–66.
- 25 T. Lin, J. Li, X. Quan and P. Cheng, *Int. Commun. Heat Mass Transf.*, 2018, **97**, 118–124.
- 26 Y. Chen, P. Fu, C. Zhang and M. Shi, *Int. J. Heat Fluid Flow*, 2010, **31**, 622–629.
- 27 D. Surblys, Y. Kawagoe, M. Shibahara and T. Ohara, *J. Chem. Phys.*, 2019, **150**, 114705.
- 28 Z. Song, Z. Cui, Q. Cao, Y. Liu and J. Li, *J. Mol. Liq.*, 2021, **337**, 116052.
- 29 Y. Guo, D. Surblys, Y. Kawagoe, H. Matsubara and T. Ohara, *J. Appl. Phys.*, 2019, **126**, 1–12.
- 30 Y. Guo, D. Surblys, H. Matsubara, Y. Kawagoe and T. Ohara, *J. Phys. Chem. C*, 2020, **124**, 27558–27570.
- 31 Y. Guo, D. Surblys, H. Matsubara and T. Ohara, *J. Mol. Liq.*, 2021, **335**, 116243.
- 32 D. Huang, R. Ma, T. Zhang and T. Luo, *ACS Appl. Mater. Interfaces*, 2018, **10**, 28159–28165.
- 33 T. Zhang, A. R. Gans-Forrest, E. Lee, X. Zhang, C. Qu, Y. Pang, F. Sun and T. Luo, *ACS Appl. Mater. Interfaces*, 2016, **8**, 33326–33334.
- 34 X. Wei, T. Zhang and T. Luo, *ACS Appl. Mater. Interfaces*, 2017, **9**, 33740–33748.
- 35 C. U. Gonzalez-Valle, S. Kumar and B. Ramos-Alvarado, *ACS Appl. Mater. Interfaces*, 2018, **10**, 29179–29186.
- 36 H. Han, S. Merabia and F. Müller-Plathe, *Nanoscale*, 2017, **9**, 8314–8320.
- 37 M. Barisik and A. Beskok, *Int. J. Therm. Sci.*, 2014, **77**, 47–54.
- 38 G. Song and C. Min, *Mol. Phys.*, 2013, **111**, 903–908.
- 39 H. Han, S. Mérabia and F. Müller-Plathe, *J. Phys. Chem. Lett.*, 2017, **8**, 1946–1951.
- 40 A. Pham, M. Barisik and B. Kim, *J. Chem. Phys.*, 2013, **139**, 244702.
- 41 X. Wang and D. Jing, *Int. J. Heat Mass Transf.*, 2019, **128**, 199–207.
- 42 Z. Liang and H. L. Tsai, *Phys. Rev. E*, 2011, **83**, 1–7.

- 43 X. Wang, P. Cheng and X. Quan, *Int. Commun. Heat Mass Transf.*, 2016, **77**, 183–189.
- 44 X. Liu, D. Surblys, Y. Kawagoe, A. R. Bin Saleman, H. Matsubara, G. Kikugawa and T. Ohara, *Int. J. Heat Mass Transf.*, 2020, **147**, 118949.
- 45 D. C. Hannah, J. D. Gezelter, R. D. Schaller and G. C. Schatz, *ACS Nano*, 2015, **9**, 6278–6287.
- 46 Y. Ma, Z. Zhang, J. Chen, K. Sääskilähti, S. Volz and J. Chen, *Carbon*, 2018, **135**, 263–269.
- 47 G. Nagayama, T. Tsuruta and P. Cheng, *Int. J. Heat Mass Transf.*, 2006, **49**, 4437–4443.
- 48 T. Tsuruta and G. Nagayama, *Energy*, 2005, **30**, 795–805.
- 49 F. Li, J. Wang, G. Xia and Z. Li, *Nanoscale*, 2019, **11**, 13051–13057.
- 50 C. Herrero, G. Tocci, S. Merabia and L. Joly, *Nanoscale*, 2020, **12**, 20396–20403.
- 51 W. Q. Chen, M. Sedighi and A. P. Jivkov, *Nanoscale*, 2021, **13**, 1696–1716.
- 52 J. W. Arblaster, *Platin. Met. Rev.*, 2013, **57**, 127–136.
- 53 R. J. Sadus, *Molecular simulation of fluids*, Elsevier, Netherlands, 2nd Ed., 2002.
- 54 E. M. Yezdimer, A. A. Chialvo and P. T. Cummings, *J. Phys. Chem. B*, 2001, **105**, 841–847.
- 55 J. Delhommelle and P. Millié, *Mol. Phys.*, 2001, **99**, 619–625.
- 56 A. V. Oppenheim, *Signals, Systems and Interference*, Pearson, Boston, 1st Ed., 2016.
- 57 M. Masduzzaman and B. Kim, *ACS Omega*, 2020, **5**, 26527–26536.
- 58 B. B. Wang, Z. M. Xu, X. D. Wang and W. M. Yan, *Int. J. Heat Mass Transf.*, 2018, **125**, 756–760.
- 59 H. Sun, F. Li, M. Wang, G. Xin and X. Wang, *RSC Adv.*, 2020, **10**, 23097–23107.